Long-term monitoring (1953-2019) of geomorphologically active sections of~~n~~ ~~LIA~~ Little Ice Age lateral moraines ~~under~~ in the context of changing ~~meteorological~~ meteorological conditions

Moritz Altmann[1], Madlene Pfeiffer[2], Florian Haas[1], Jakob Rom[1], Fabian Fleischer[1], Tobias Heckmann[1], Livia Piermattei[1,3], Michael Wimmer[4], Lukas Braun[5], Manuel Stark[1], Sarah Betz-Nutz[1], Michael Becht[1]

[1]Department of Physical Geography, Catholic University of Eichstätt-Ingolstadt, Eichstätt, 85072, Germany
[2]Institute of Geography, University of Bremen, Bremen, 28359, Germany
[3]Swiss Federal Institute for Forest, Snow and Landscape Research (WSL), Birmensdorf, 8903, Switzerland
[4]Department of Geodesy and Geoinformation, TU Wien, Vienna, 1040, Austria
[5]Institute of Mathematics, Albert Ludwig University of Freiburg, Freiburg, 79104, Germany

Correspondence to: Moritz Altmann (MAltmann@ku.de)

Abstract. We show a long-term erosion monitoring of several geomorphologically active gully systems on Little Ice Age lateral moraines in the European ~~c~~Central Eastern Alps covering a total time period from 1953 to 2019 including several survey periods in order to identify corresponding morphodynamic trends. For the implementation, DEM of Differences were calculated based on multitemporal high-resolution digital elevation models from historical aerial images (generated by structure-from-motion photogrammetry with multi-view-stereo) and light detection and ranging from airborne platforms. Two approaches were implemented to achieve the corresponding objectives. First, by calculating linear regression models using the accumulated sediment yield and the corresponding catchment area (on a log-log scale), the range of the variability of the spatial distribution of erosion values within the ~~areas of interest is shown~~sites. Secondly, we use volume calculations to determine the total/mean sediment output (and erosion rates) of the entire ~~areas of interest~~sites. Subsequently, both the sites and the different time periods of both approaches are compared~~ comparison is made between the areas of interest and the epochs of both approaches.~~ Based on the slopes of the calculated regression lines, it can be shown that the highest variability of sediment yield in the sites occurs in the first time period (mainly 1950s to 1970s). This can be attributed to the fact that within some sites the sediment yield per square metre increases clearly more strongly (regression lines with slopes up to 1.5). In contrast, in the later time periods (1970s to mid-2000s and mid-2000s to 2017/2019), there is generally a decrease in 10 out of 12 cases (regression lines with slopes around 1). ~~Based on the slopes of the calculated regression lines, it could be shown that the highest range of the variability of sediment yield within all areas of interest is in the first epoch (mainly 1950s to 1970s), as in some areas of interest sediment yield per square metre increases clearly more (regression lines with slopes up to 1.5), which in the later epochs (1970s to mid-2000s and mid-2000s to 2017/2019) generally decreases in 10 out of 12 cases (regression lines with slopes around 1).~~ However, even in the ~~areas of interest~~sites with an increase in the variability of sediment yield over time,

Formatiert: Absatz-Standardschriftart

Formatiert: Schriftart: 10 Pt., Schriftfarbe: Automatisch

Formatiert: Schriftart: 10 Pt., Schriftfarbe: Automatisch

Formatiert: Schriftart: 10 Pt., Schriftfarbe: Automatisch

Formatiert: Schriftart: 10 Pt., Schriftfarbe: Automatisch

Formatiert: Schriftart: 10 Pt., Schriftfarbe: Automatisch

Formatiert: Schriftart: 10 Pt., Schriftfarbe: Automatisch

the earlier high variabilities are no longer reached. This means that the spatial pattern of erosion in the gully heads changes over time as it becomes more uniform. Furthermore, using sediment volume calculations and corresponding erosion rates, we show a generally decreasing trend in geomorphic activity (amount of sediment yield) between the different time periods ~~epochs~~ in 10 out of 12 ~~areas of interest~~sites, while 2 ~~areas of interest~~sites show an opposite trend where morphodynamics increase and remain at the same level. Finally, we summarise the results of long-term changes in the morphodynamics of geomorphologically active areas on lateral moraines by presenting the "sediment activity concept", which, in contrast to theoretical models, is based on actually calculated erosion. The level of geomorphic activity depends strongly on the characteristics of the ~~areas of interest~~sites, such as size, slope length and slope gradient, some of which are associated with deeply incised gullies. It is noticeable that especially areas with influence of dead ice over decades ~~of dead ice influence~~ in the lower slope area show high geomorphic activity. Furthermore, we show that system-internal factors as well as the general paraglacial adjustment process have a greater influence on long-term morphodynamics than changing external weather and climate conditions, which, however, had a slight impact mainly in the last, i.e. most recent time period ~~epoch~~ (mid-2000s to 2017/2019) and may have led to an increase in erosion at the ~~areas of interest~~sites.

Keywords: Airborne Laser Scanning (ALS), DEM of Difference (DoD), gully erosion, historical aerial images ~~(HAI)~~, ~~gully erosion,~~ Little Ice Age (LIA) lateral moraines, paraglacial process system, proglacial areas, ~~modelling,~~ Structure-from-Motion (SfM) photogrammetry, ~~proglacial areas,~~ Weather Research and Forecasting (WRF) model

1 Introduction

Since the end of the Little Ice Age (LIA) around 1850 (Matthews and Briffa, 2005; Ivy-Ochs et al., 2009) and the strong global warming of the last decades (IPCC, 2021; Pepin et al., 2022), proglacial areas play a special role in the current landscape changes of high alpine geosystems, as such areas are strongly ~~increasing~~ extending due to the ongoing retreat of the glaciers (Deline et al; Heckmann and Morche, 2019; Haeberli and Whiteman, 2021). The melting of glaciers leads to the release of unstable sediment sources, which are subsequently exposed to several geomorphological slope processes, which can lead to high erosion rates.

The relationship between this glacier melt and slope instability has been subject of research for several decades. Church and Ryder (1972) were the first to develop a theoretical model ("paraglacial concept") to describe future landscape change throughout a proglacial area and defined the phase of transition as the paraglacial period, during which paraglacial processes (non-glacial processes) occur. After a period of high geomorphic activity (fluvial erosion and transport) associated with a peak, sediment production decreases over time until a "normal" level of sediment movement is reached. By further developing the model, Ballantyne (2002a) describes this paraglacial landscape adjustment using the "sediment exhaustion model", which is based on a hypothetical paraglacial system. Several variable factors determine the duration of this period, such as sediment release and the rate of sediment reworking. Following the sediment exhaustion model, the rate of sediment reworking of glacigenic sediments in proglacial areas decreases exponentially if the sediment release rate only depends on sediment availability (Ballantyne, 2002a, 2002b).

Ballantyne and Benn (1994) and Curry (1999) describe the paraglacial slope adjustment of lateral moraines by analysing the formation of gully systems on lateral moraines and the corresponding alluvial fans and debris cones (both in western Norway). These systems result from weathering and erosion, such as fluvial erosion, slope wash, debris flows, smaller slope failures, and ground/snow avalanches (Ballantyne, 2002a, 2002b; Curry et al., 2006; Haas et al., 2012; Dusik et al., 2019). Material is deposited in the gullies (e.g. by nival processes, fluvial activity and sidewall collapse) and subsequently ~~is then~~ transported downslope, mainly by debris flows triggered in the gully heads after heavy rainfall or after rapid snowmelt (Ballantyne and Benn, 1994; Ballantyne, 2002b; Curry et al., 2006). Similarly, large deformations such as deep-seated slope failures and landslides with low frequency and high magnitude also occur (Mattson and Gardner, 1991; Blair, 1994; Hugenholtz et al., 2008; Altmann et al., 2020; Cody et al., 2020; Betz-Nutz, 2021; Zhong et al., 2022). These erosion processes are primarily driven by temperature and precipitation events, which have been subject to change in recent years and decades (Serquet et al., 2011; Brugnara et al., 2012; Mankin and Diffenbaugh, 2015; Klein et al., 2016; Beniston et al., 2018; Hock et al., 2019; IPCC, 2021; Pepin et al., 2022). Spring-time snowmelt provide important preparatory steps for sediment transport processes, such as loosening of the upper layers of sediments of the slope or through the delivery of material into the gulllies by nival processes, which is then transported downslope by debris flows in the summer months (Haas et al., 2012; Dusik et al., 2019), which is considered as the most important process occurring (Ballantyne, 2002a; Curry et al., 2006). Dusik (2019) also shows a positive correlation between the number of mass movements and the number of extreme precipitation intensities, the number of certain threshold exceedances for extreme daily precipitation totals as well as annual precipitation totals. These processes ultimately lead to the dissection of the upper parts of the lateral moraines which is, however, limited in time (Curry et al., 2006). Curry et al. (2009) inferred from morphometric measurements along a chronosequence that gullies increase in depth, width, area, and volume over time, with width increasing significantly more than depth, resulting in the older ones not being as densely gullied. Furthermore, it is described that the slope gradient decreases over time, e.g. Ballantyne and Benn (1994) report an average of 5° (in 48 years between 1943 and 1991). Betz-Nutz et al. (2023) document a range of slope gradient changes between -3.2° and +6.6° between the ~1950s and 2018 (~68 years), showing that both increases and decreases can occur. Ballantyne and Benn (1994), Curry (1999) and Curry et al. (2006) give average annual erosion rates of different gully systems over several decades estimated by the volume of the gullies. Curry et al. (2006) showed at different test sites in the Swiss Alps that the maximum extent of gullies is reached after 50 years of ice release and that sediment filling and stabilisation occurs after 80-140 years of deglaciation. While 50% of the available sediment is exhausted after 10-50 years, it can take several centuries until the paraglacial adjustment process is completed (Curry et al., 2006). Schiefer and Gilbert (2007) show, based on quantitative analyses (via stereo-photogrammetry using historical aerial images), a significant decrease in the geomorphic activity of gully systems on lateral moraines over several decades and different time periods ~~epochs~~ in the glacier foreland~~field~~ of the Lillooet Glacier (Canada, British Columbia). Carrivick et al. (2013) generally confirm the concept of paraglacial adjustment by showing decreasing morphodynamics with increasing distance from the glacier as they have been ice-free for a longer time. However, the lower morphodynamics observed in the distal areas of the glacier forelands ~~forefields~~ could also be due to the generally lower slope gradients there (Betz-Nutz et al., 2023). Lane et al. (2017) showed in the glacier foreland ~~forefield~~ of Haut Glacier d'Arolla (Switzerland, Valais) that there are no indications of filling in the developed gully systems, which indicates that they are still in the incision phase. Betz-Nutz et al. (2023) show with the use of historical aerial photographs (processed by SfM-photogrammetry) that the paraglacial adjustment process over decades is very variable. While 13 out of 20 moraine sections showed decreasing erosion rates over decades, divided into several time periods~~epochs~~, six showed almost constant activity and one section even showed a substantial increase in erosion rate.

The period of paraglacial landscape adjustment is also influenced by upcoming vegetation, which can be considered both a consequence and a cause of slope stabilisation (Eichel et al., 2016; Haselberger et al., 2021; Haselberger et al., 2022; Eichel et al., 2023). Nevertheless, bound solifluction processes can occur under a dense vegetation cover and are therefore not an absolute sign of stabilisation (Draebing and Eichel, 2017).

The generation of multitemporal accurate and precise digital elevation models (DEMs) and the resulting DEM of Differences (DoDs) by different remote sensing methods and techniques, which have been established in geomorphological research in recent years, enabled the detection of changes in the Earth's surface in high spatial and temporal resolution (Pulighe and Fava, 2013; Nebiker et al., 2014; Tarolli, 2014; Smith et al., 2016; Eltner et al., 2016; Sevara et al., 2018; Okyay et al., 2019; Noto et al., 2017). By processing overlapping high-resolution digitised historical aerial images ~~(HAI)~~ of high alpine geosystems, using SfM-MVS (Structure-from Motion with Multi-View-Stereo) digital stereo-photogrammetry in combination with current airborne LiDAR (Light Detection And Ranging) data into DEMs and the corresponding DoDs, landscape changes in these areas can be reconstructed over several decades (Midgley and Tonkin, 2017; Mölg and Bolch, 2017; Lane et al., 2017; Betz et al., 2019; Altmann et al., 2020; Fleischer et al., 2021; Betz-Nutz, 2021; Stark et al., 2022; Piermattei et al., 2022). The spatial distribution of positive and negative DoD elevation changes enable various analyses, such as the reconstruction and interpretation of individual geomorphological processes (Dusik, 2019) or the calculation of morphological budgets (Altmann et al., 2020).

Furthermore, by applying flow routing algorithms and the accumulation of DoD values accordingly, sediment yield ~~(SY)~~ from the contributing area of each cell can be determined: Pelletier and Orem (2014) used repeat airborne LiDAR-based DEMs before and after a wildfire and calculated for each pixel the net sediment volume exported by geomorphological processes. Further applications of this methodology have been published by Wester et al. (2014), who calculated the total sediment yield ~~SY~~ by applying a weighted flow accumulation algorithm, and Heckmann and Vericat (2018), who further developed the approach by calculating a spatially distributed measure of functional sediment connectivity on a proglacial slope. Neugirg et al. (2015a; 2015b; 2016) showed a positive correlation between log sediment yield ~~SY~~ (calculated by accumulated DoD values on slopes) and the corresponding log ~~SCA (~~sediment contributing area~~)~~, respectively log ~~CA (~~catchment area (using the sediment-contributing-area approach), ~~),~~ both extracted at randomly selected cells of the channel network (so-called "virtual sediment traps"~~, VST~~). Besides to these studies conducted over several months and years on slopes~~, which were carried out on hillslopes~~ in the Northern Alps (Germany, Lainbach valley and Arzbach valley) and at a former iron ore mine on the island of

Elba in the Tyrrhenian Sea (Italy, next to Rio Marina)), this approach was also applied by Dusik (2019) and Dusik et al. (2019) over several weeks to a proglacial slope in Kaunertal (Austria, Tyrol). One advantage of this approach is that it can be used to determine not only the size of sediment yield ~~SY~~ (which can be compared with previous time periods~~epochs~~, for example), but also the variability of sediment yield ~~SY in~~within the ~~AOI~~ site ~~within~~ in an time period ~~epoch~~ (spatial pattern of sediment yield ~~SY~~ within the ~~AOI~~site), which is not possible, for example, when calculating simple erosion rates, where only the volume of the total change can be computed.

In this study we apply the sediment-contribution-area approach to several LIA lateral moraine sections over several decades and several time periods in the European Central Eastern Alps in order to better understand the paraglacial adjustment process of lateral moraines. Thus, the aim is to find out how the spatial erosion pattern within the areas changes over time. ~~In order to better understand the paraglacial adjustment process of lateral moraines, we continue the application (Sediment contributing area approach) to different LIA lateral moraines in the central Eastern Alps in this study.~~ Secondly, we show volume calculations of the entire ~~AOIs~~ sites to determine the total sediment yield (and erosion rates). Therefore, by ~~C~~combining high-resolution historical and current DEMs and the corresponding DoDs, we show~~, the~~ quantification and analysis of gully system morphodynamics at 12 different sections in the upper reaches of lateral moraines in five different glacier forelands ~~forefields~~ over a total period ~~epoch~~ of several decades (1953-2019) with several survey periods (~1950s to ~1970s, ~1970s to ~2000s and ~2000s to 2017/2019). ~~-~~By using simulated climate data of the glacier forelands ~~forefields~~ we were able to investigate, besides system-internal influences, also external impacts on the morphodynamics, which have not been considered in long-term studies on erosion of LIA lateral moraines so far.

2 Study Area

The sites ~~areas of interest (AOIs)~~ are located in different high alpine geosystems along a north-south axis in the European Central Eastern Alps ~~central Eastern Alps~~ and are situated north (Horlachtal and upper Kaunertal) and south (upper Martelltal) of the ~~m~~Main ~~a~~Alpine ~~d~~Divide. In these valleys, the sites ~~AOIs~~ are located within five glacier forelands ~~forefields~~ on lateral moraines formed by the glaciers during their maximum glacier ~~extent~~ outline during the LIA around 1850 (Figure 1). The Horlachtal is located in the Stubai Alps (Tyrol, Austria), which is a tributary of the Oetztal (Geitner, 1999; Rieger, 1999). The investigated section of the Horlachtal is located in the side valley and sub-catchment Grastal (glacier foreland ~~forefield~~ Grastalferner), which is oriented in a north-south direction. Geologically, the Horlachtal is located in the Oetztal Massif, where gneisses and mica schists dominate (Becht, 1995; Geitner, 1999). The Kaunertal is also located in the Oetztal Alps (Tyrol, Austria) and is oriented in a north-south direction. This valley geologically belongs to the Austroalpine crystalline complex (Tollmann, 1977; Geological Survey of Austria, 1999) where crystalline rocks, mainly ortho- and paragneisses, dominate (Vehling, 2016). The sites ~~AOIs~~ within the Kaunertal are located in the glacier forelands ~~forefields~~ of the Gepatschferner, another glacier outlet of the Gepatschferner, the so-called Münchner Abfahrt (MA), and the Weißseeferner. The Martelltal is a southwest-northeast oriented valley located in the Ortler-Cevedale group (South Tyrol, Italy) and belongs geologically to the Ortler-Campo Crystalline, where quartz phyllite dominates with layers of e.g. shales, gneisses and marbles (Mair and Purtscheller, 1996; Staindl, 2000; Mair et al., 2007). The two sites ~~AOIs~~ are located in the glacier foreland ~~forefield~~ of the Hohenferner. All valleys are characterized by the continental climate and low annual precipitation sums of the inner alpine dry region (Becht, 1995; Hagg and Becht, 2000; Veit, 2002; Hilger, 2017; Betz-Nutz, 2021). The sites ~~AOIs~~ are characterized by very ~~low~~ sparse vegetation cover, intense paraglacial morphodynamics and typical unsorted moraine material. Table 1 and Figure 1 give an overview of the location as well as the characteristics of the sites~~AOIs~~.

Table 1: Characteristics of the ~~AOIs~~sites. Values were derived from 2017 DEM (Kaunertal) and 2019 DEM (Horlachtal and Martelltal).

~~AOI~~Sites	Location (Centre) (ETRS89/ UTM Zone 32N, EPSG Code: 25832)	Elevation (Ellipsoidal heights) (m)	Aspect	Size (m²)	Max. length of delinated ~~AOI~~ site (downslope) (m)	Mean (and max.) slope gradient (°)	At least ice-free since (years)*	Glacial or dead ice influence at the foot of the slope
HG1	E 652032, N 5218283	2659-2696	W	1647	43	37.9 (46.8)	1860 (159)	Not detectable
KG1	E 632991, N 5193590	2183-2262	W	12431	124	41.5 (69.3)	1937 (80)	Not detectable
KG2	E 633140, N 5193339	2244-2321	SW	8814	59	43.8 (61)	1933 (84)	Until 2006
KG3	E 633421, N 5193204	2329-2400	S	3123	29	38.5 (48.3)	1872 (145)	Not detectable
KG4	E 634596, N 5193101	2540-2620	SW	6193	99	41.1 (61.3)	1929 (88)	until today
KG5	E 634789, N 5192997	2580-2645	SW	3531	77	44.3 (57.1)	1913 (104)	until today
KM1	E 632904, N 5192058	2443-2486	E	2025	23	39.8 (46.9)	1903 (114)	Not detectable
KM2	E 632783, N 5191632	2560-2598	E	2534	30	45.7 (56.7)	1901 (116)	Until 2006
KW1	E 631025, N 5192561	2546-2603	SW	2951	38	41.6 (54.4)	1924 (93)	Not detectable
KW2	E 631204, N 5192213	2682-2714	SW	3638	49	39.9 (53.4)	1937 (80)	Until 2006
MH1	E 628937, N 5147454	2704-2729	E	1475	26	35.5 (51.6)	1921 (98)	Not detectable
MH2	E 629426, N 5147413	2755-2796	SW	3983	45	45.3 (72)	1943 (76)	Until 2004/2005

***Determination of complete deglacialisation is based on an interpolation between the two glacier ~~extensions~~ outlines within which the ~~AOIs~~ sites have become ice-free by calculating the euclidean distance as proposed by Betz-Nutz et al. (2023).**

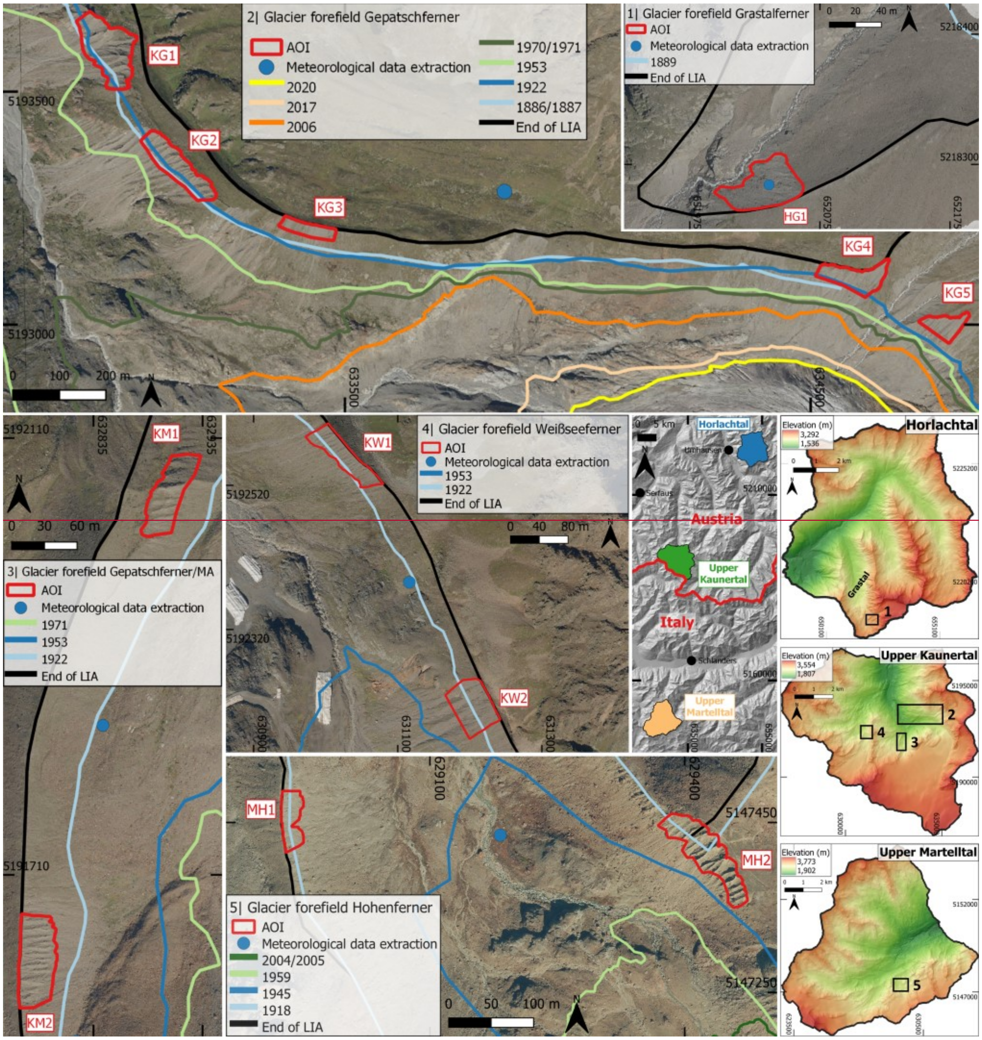
2| Glacier forefield Gepatschferner
AOI
Meteorological data extraction
2020
2017
2006
1970/1971
1953
1922
1886/1887
End of LIA
KG1
KG2
KG3
KG4
KG5
5193500
5193000
633500
634500
0 100 200 m
1| Glacier forefield Grastalferner
AOI
Meteorological data extraction
1889
End of LIA
0 20 40 m
5218400
5218300
651975
652075
652175
HG1
3| Glacier forefield Gepatschferner/MA
AOI
Meteorological data extraction
1971
1953
1922
End of LIA
KM1
KM2
5192110
5191710
632835
632935
0 30 60 m
4| Glacier forefield Weißseeferner
AOI
Meteorological data extraction
1953
1922
End of LIA
KW1
KW2
5192520
5192320
630900
631100
631300
0 40 80 m
5| Glacier forefield Hohenferner
AOI
Meteorological data extraction
2004/2005
1959
1945
1918
End of LIA
MH1
MH2
629100
629400
5147450
5147250
0 50 100 m
0 5 km
Horlachtal
Umhausen
Serfaus
Austria
Upper Kaunertal
Italy
Schlanders
Upper Martelltal
5210000
5160000
Elevation (m)
3,292
1,536
Horlachtal
Grastal
1
0 2 km
5225200
5220200
Elevation (m)
3,554
1,807
Upper Kaunertal
2
3
4
0 1 2 km
5195000
5190000
Elevation (m)
3,773
1,902
Upper Martelltal
5
0 1 2 km
5152000
5147000
N

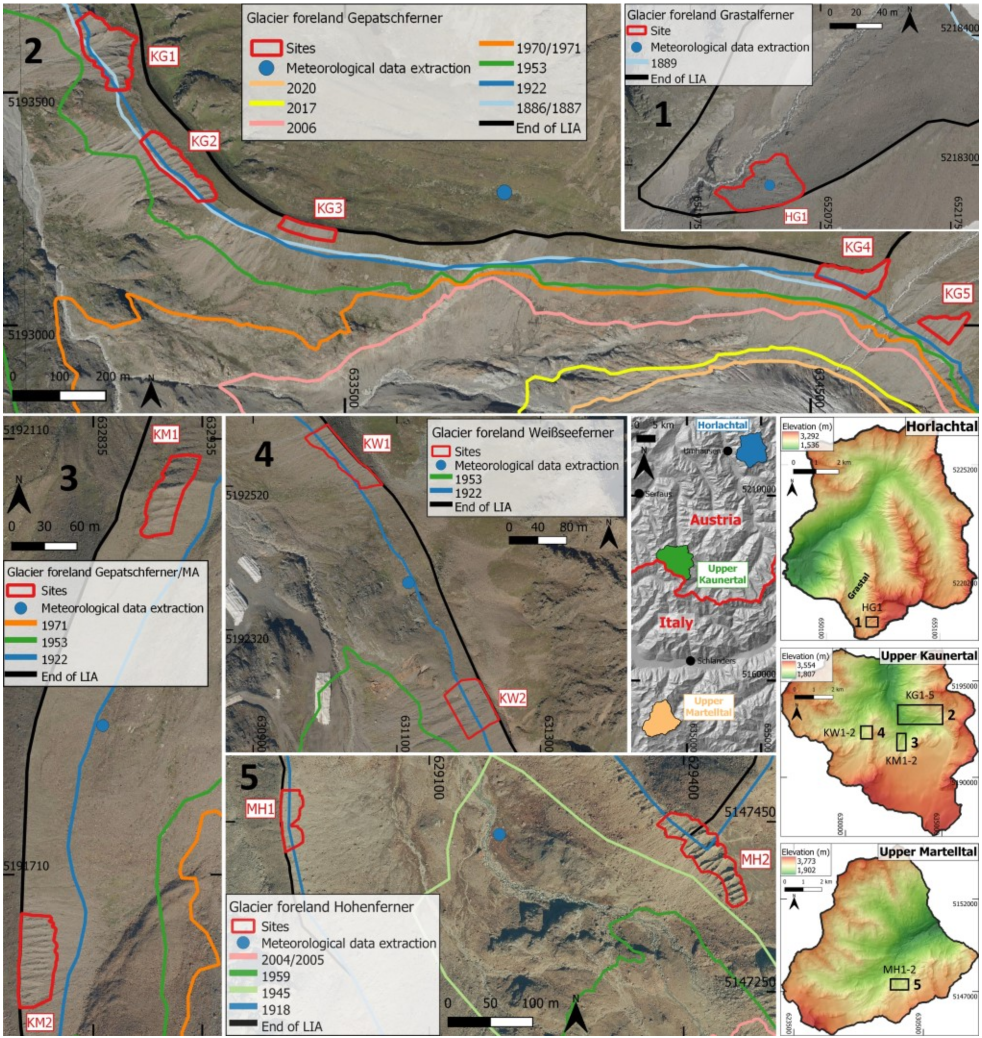

Figure 1: Location of ~~AOIs~~the sites, glacier ~~extents~~ outlines (Sources in Table 2) and location for meteorological data extraction (for corresponding analysis, see sec. 3.3). Large-scale elevation data (DSM, 25 m) (centre right) are based on SRTM and ASTER GDEM (Copernicus, 2016). DEMs (1 m) (right and bottom right) are based on airborne LiDAR (ALS) data from 2017 (Kaunertal) and 2019 (Horlachtal and Martelltal) (see sect. 3.1.1). Orthophotos (from 2020) are provided by the Province of Tyrol (Horlachtal and

Kaunertal) and by the Autonomous Province of Bolzano, South Tyrol (Martelltal). The glacier ~~extent~~ outline of Groß and Patzelt (2015) is based on mapping of the LIA lateral moraines and field surveys based on orthophotos. In the process of this study, these mappings were slightly modified so that they fit to the maximum glacier ~~extent~~ outline (LIA lateral moraines) more accurately. The glacier ~~extents~~ outlines end of LIA, 1918, 1945 and 1959 in the Martelltal have already been described by Betz et al. (2019).

Formatiert: Standard

Table 2: Sources of the glacier ~~extents~~outlines.

Valley	Year	Source
Horlachtal	End of LIA	Groß and Patzelt (2015)
	1889	Gedächtnisspeicher Ötztal (Austria, Längenfeld), K&K Militärgeographisches Institutsarchiv*
Kaunertal	End of LIA	Groß and Patzelt (2015)
	1886/1887	Finsterwalder and Schunck (1888)*
	1922	Finsterwalder (1928)*
	1953	Images of BEV, DoD 1953/2017***
	1970/1971	Images of the Office of the Tyrolean Government, DoD 1970/1971-2017***
	2006	Province of Tyrol, DoD 2006-2017***
	2017	Chair of Physical Geography, Cath. University Eichstätt-Ingolstadt, SEHAG-project (See sect. 3) **
	2020	Province of Tyrol, orthofoto**
Martelltal	End of LIA	Mapped on base of visible moraines and descriptions of Finsterwalder (1890)
	1918	Spezialkarte 1:75.000 of BEV*
	1945	Images of the IGMI, orthofoto*
	1959	Images of IGMI, DoD 1959-2019***
	2004/2005	Autonomous Province of Bolzano, DoD 2004/2005-2019***

***based on historical map, **based on orthophoto and/or hillshade and ***based on DoD (SfM-MVS/photogrammetry and/or ALS).**

3 Material and Methods

3.1 Generation of the topographic data

3.1.1 Processing of airborne LiDAR and photogrammetric/SfM-MVS point clouds

Several data sets were used for the reconstruction of the terrain surface for the entire catchments. These include both current airborne LiDAR data and historical aerial image series (Figure 2). Thus, the time periods ~~epochs~~ are based on the availability and quality of the data.

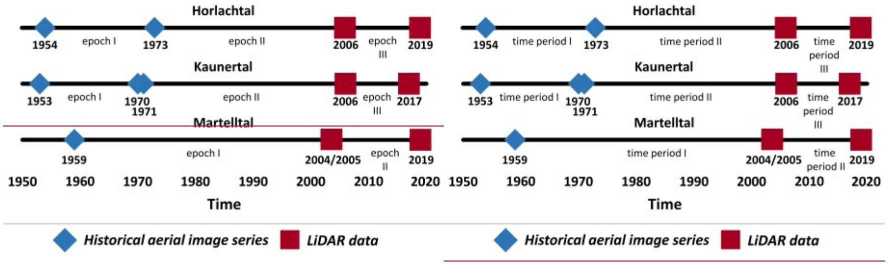

Figure 2: Type of topographic dataset and the resulting time periods.~~Data and epochs.~~

To determine the recent morphodynamics in the respective ~~AOIs~~sites, available airborne LiDAR data from 2004/2005 to 2019 were used. The 2004/2005 and 2006 data of the three valleys were provided by the Autonomous Province of Bolzano and the Province of Tyrol (Table 3). The latest ALS datasets of each valley (2017 and 2019) were collected in own ALS flight campaigns of the Chair of Physical Geography at the Catholic University of Eichstätt-Ingolstadt (Table 3) (Stark et al., 2022). In this case, LiDAR data sets were collected using previously determined flight strips. Direct georeferencing (position and altitude) of the trajectories was determined by Global Navigation Satellite System (GNSS) rover antenna and an Inertial Measurement Unit (IMU) (Applanix AP 20), both located in the laser scanner. In addition, GNSS correction data were acquired on the ground during the flight missions using a dGNSS antenna (Figure 3).

~~Subsequently, the GNSS/IMU trajectory data were processed in three steps. This included, (i) the calculation of precise trajectories using the software PosPac MMS (Applanix), (ii) the attachment of raw scans to the flight lines using the software package Riegl RiProcess, and finally (iii) a strip adjustment in the processing software OPALS (Pfeifer et al., 2014) using the approach of Glira et al. (2015).~~

Table 3: ALS and DEM data and corresponding flight mission attributes.~~Overview of the ALS (and DEM) data.~~

Valley	Date of acqui-sition	Source/Purpose	Laser-scanner	Field of view (°)	Flying altitude (metre above ground)	Air-speed (kn)	Laser pulse Measuring frequency (khz)	Wave-length (nm)	DEM res. or mean point density of the ~~AOIs~~ sites (points/m^2)
Horlachtal	05.09.2006	Province of Tyrol	N/A	N/A	N/A	N/A	N/A	N/A	DEM, 1 m
	08.08.2019	SEHAG project (“SEnsitivity of High Alpine Geosystems to climate change since 1850”)	Mobile laser scanner VP1 (Riegl VuxSys-LR)	180	~150	~45	200	1550	24.1
Kaunertal	05.09.2006	Province of Tyrol	N/A	N/A	N/A	N/A	N/A	999	3.4
	05.07.2017	PROSA project (“High-resolution measurements of	Mobile laser scanner	180	~150	~45	200	1550	35.7

		morphodynamics in rapidly changing PROglacial Systems of the Alps")	VP1 (Riegl VuxSys-LR)						
Martelltal	2004/2005	Autonomous province of Bolzano	N/A	N/A	N/A	N/A	N/A	N/A	1.4
	09.08.2019	SEHAG project ("SEnsitivity of High Alpine Geosystems to climate change since 1850")	Mobile laser scanner VP1 (Riegl VuxSys-LR)	180	~150	~45	200	1550	13.3

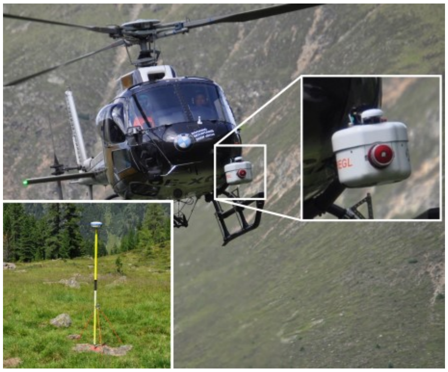

Figure 3: ALS data collection on 08.08.2019 in Horlachtal. Helicopter with nose-mounted VP1 laser scanner as well as the ground station which recorded the dGNSS raw data during the flight time (Stonex S9III).

In order to extend the temporal scope of this study by several decades (until 1953), previously digitised (high-resolution) overlapping historical aerial images ~~HAI~~ were processed into historical DEMs. Except for the 1959 Martelltal-survey, camera distortion parameters and focal lengths were provided for all data with the respective camera calibration certificates (Table 4). The digitised image series were processed with the Agisoft Metashape Professional software package (Version 1.6.6; Agisoft LLC) using Structure from Motion (SfM) photogrammetry with multi-view-stereo (MVS) algorithms to generate high-resolution point clouds. The generation of point clouds from digitised historical (aerial)image series requires different preparation and processing steps. First, all images of each series were resized to a common image size (uniform number of pixels along the x- and y-axis) without changing the image content. This step was necessary so that the software can assign all images to the same camera (source) and was carried out using Adobe Photoshop (CS6). This is of enormous importance in order to be able to use the appropriate distortion parameters for the respective camera models for the calculation. After, the image sets were imported into single folders and a common global coordinate system (ETRS89/UTM zone 32N; EPSG code: 25832) was defined. Next, all images were masked to exclude the black borders/frame (instrument stripes with the camera metadata) in order to avoid interference with the orientation of the cameras (Gomez et al., 2015). Before the initial processing of images we defined the fiducial mark information and lens distortion parameters in order to set the metric dimension of images and lenses. This informations were included and used for the alignment of single images (SfM).

Since a global exterior orientation requires a large number of precisely surveyed ground control points (GCPs) distributed throughout the area, we used highly-precise ALS datasets with millimetre accuracy (2019 Horlachtal; 2017 Kaunteral) to extract these GCPs and to define the exterior orientation of all data. The selection and extraction of GCPs was based on clearly identifiable objects (e.g. rock formations) that were also considered as stable (geomorphologically unchanged) over the entire observation period. If a calibration certificate was available, the film camera option was used, fiducial marks defined, the focal length set and fixed. All other lens distortion parameters (C_x,C_y, k_1,k_1, $k_{1,}$ p_1 & p_2) were estimated and adjusted fully automatic using the auto-calibration function. In case of missing camera calibration certificate, an auto-calibration (no film camera) was performed. Both options were proposed by Stark et al. (2022).

According to these pre-processing steps, the point clouds were generated by (i) initial joint orientation of the images, (ii) selection of ground control points (GCPs), (iii) final camera orientation (bundle block adjustment) including scale definition, and (iv) calculation of dense point clouds.

The processing of the 1959 point cloud, which was used in this study, is already described in Betz et al. (2019).

Table 4: Overview of acquired historical image series for point cloud generation and corresponding DEMs by photogrammetry/SfM.

	1953 (Kaunertal)	1954 (Horlachtal)	1959 (Martelltal)	1970 (Kaunertal)	1971 (Kaunertal)	1973 (Horlachtal)
Source/ Purpose	BEV/Forest condition estimation; Flight C	BEV/Forest condition estimation; Flight D	IGMI	Office of the Tyrolean Government/ Tyrolean state Surveying flight	Office of the Tyrolean Government/ Tyrolean state Surveying flight	Office of the Tyrolean Government/ Tyrolean state Surveying flight
Date of acquisition	31.08.1953/ 01.09.1953/ 08.09.1953	31.08.1954/ 04.09.1954	09.09.1959/ 20.09.1959	29.09.1970	18.08.1971	06.08.1973
Flying altitude (m a.s.l)	ca. 5955/ unknown ca. 5850	ca. 6110/ ca. 5920	ca. 5100/ ca. 5000	ca. 8665	ca. 5025	ca. 4900
Camera	Wild RC/5	Wild RC/5	Santoni	Wild RC5/RC8	Wild RC5/RC8	Wild RC5/RC8
Number of images	36/51/63	32/4	2/6	26	31	88
Focal length (mm)	210.11	210.23	153.41	210.43	209.48	210.43
Scanning Resolution (µm)	15	15	N/A	12	12	12
Format	TIFF	TIFF	TIFF	TIFF	TIFF	TIFF
Calibration protocol available	yes	yes	no	yes	yes	yes
Number of GCPs	100	74	23	88	29	67

Mean point density (points/m²)*	8.5	3.7	4.9	13.3	15.7	20.5
Ground resolution (cm/pix) **	22.5	34.8	19.6	19	17	13.8
RMS reprojection error (pix) **	0.48	0.51	1.55	0.86	0.44	0.45

***refers to the exact ~~AOIs~~sites, **refers to the entire data set**

3.1.2 Digital elevation model (DEM) and DEM of Difference (DoD) processing

Although all point clouds were finally available in the same coordinate system (ETRS89/UTM Zone 32N, EPSG Code: 25832), a local adjustment of each ~~AOI~~ site was carried out to obtain the highest possible accuracy of the subsequent DoDs to be calculated. For this purpose, stable areas, i.e. geomorphologically unchanged areas such as rock outcrops or stable areas on the lateral moraines, were mapped next to each ~~AOI~~ site based on orthophotos. To match the point clouds as well as possible, the Iterative Closest Point algorithm (ICP) (Besl and McKay, 1992; Bakker and Lane, 2017) implemented in SAGA-LIS (Conrad et al., 2015) was used for fine registration. Previously, the LiDAR based point clouds were further processed in the software SAGA-LIS (LIS Pro 3D) from Laserdata (laserdata.at) in combination with Python and R to prepare point clouds for the generation of high-resolution digital elevation models (DEMs). This included the removal of outliers (Remove Isolated Points), a ground classification (to remove vegetation), which was carried out with a modified approach according to Hilger (2017) and the achievement of more homogeneous point clouds with the tool 3D Block Thinning (PC) in SAGA-LIS. The point clouds were then converted into DEMs using the Point Cloud to Grid tool in SAGA-LIS (elevations of points averaged for each raster cell; cell sizes for Horlachtal and Kaunertal 1m, for Martelltal 2m). Finally, the DoDs were generated by subtracting the individual DEMs from each other to determine the positive and negative elevation changes of the earth's surface.

3.1.3 ~~Uncertainty assessment~~Data statistics

The presence of various uncertainties in differently generated DEMs (Hodgson and Bresnahan, 2004; Bakker and Lane, 2017) also leads to uncertainties in the resulting DoDs (Lane et al., 2003; Rolstad et al., 2009; Cavalli et al., 2017; Anderson, 2019). Therefore, an uncertainty assessment was carried out using the DoD values from stable areas near each ~~AOI~~site. The size of the stable areas varied between 25% and 75% of the size of the corresponding ~~AOI~~site. In addition to the estimation of the precision (Std Dev) and accuracy (RMSE), the arithmetic mean, minimum and maximum values were also determined (Figure 4).

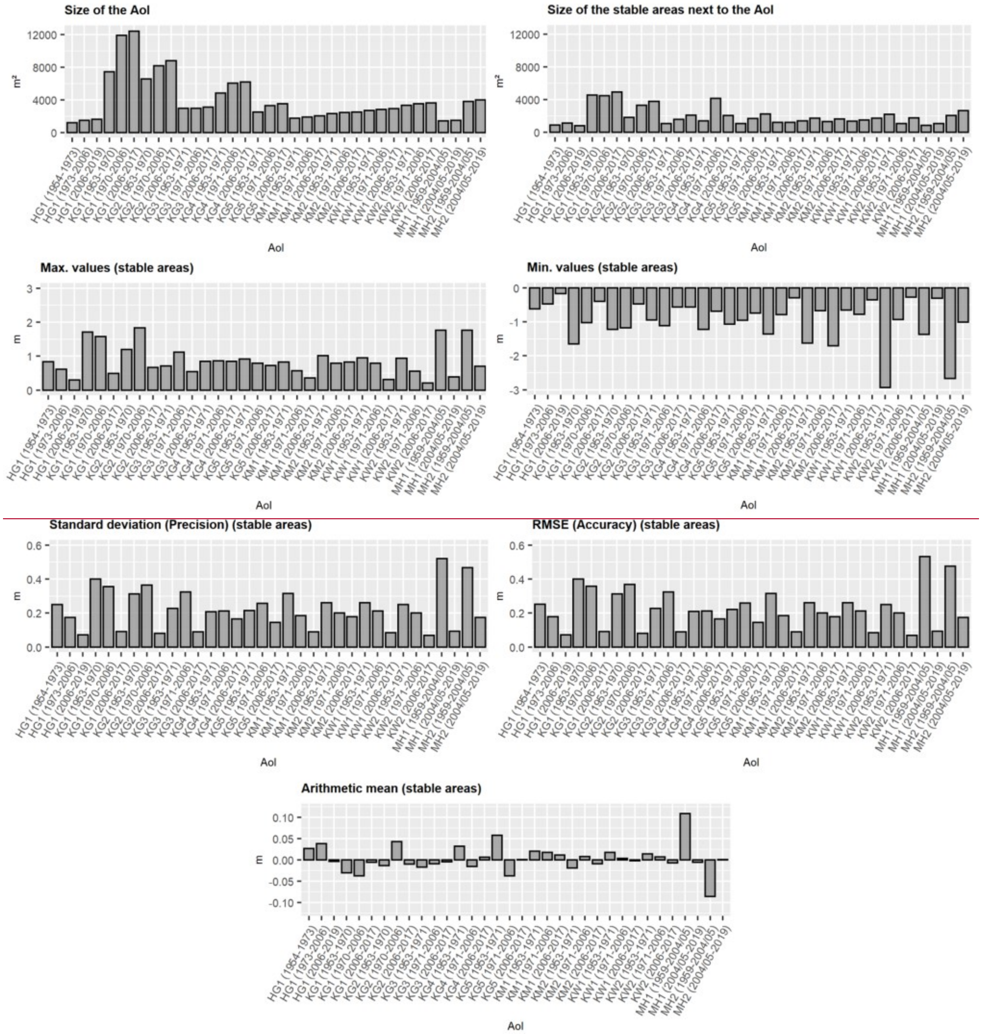
Size of the AoI
m²
12000
8000
4000
0
Size of the stable areas next to the AoI
Max. values (stable areas)
m
3
2
1
0
Min. values (stable areas)
0
-1
-2
-3
Standard deviation (Precision) (stable areas)
0.6
0.4
0.2
0.0
RMSE (Accuracy) (stable areas)
Arithmetic mean (stable areas)
0.10
0.05
0.00
-0.05
-0.10
AoI
HG1 (1954-1973)
HG1 (1973-2006)
HG1 (2006-2019)
KG1 (1953-1970)
KG1 (1970-2006)
KG1 (2006-2017)
KG2 (1953-1970)
KG2 (1970-2006)
KG2 (2006-2017)
KG3 (1953-1971)
KG3 (1971-2006)
KG3 (2006-2017)
KG4 (1953-1971)
KG4 (1971-2006)
KG4 (2006-2017)
KG5 (1953-1971)
KG5 (1971-2006)
KG5 (2006-2017)
KM1 (1953-1971)
KM1 (1971-2006)
KM1 (2006-2017)
KM2 (1953-1971)
KM2 (1971-2006)
KM2 (2006-2017)
KW1 (1953-1971)
KW1 (1971-2006)
KW1 (2006-2017)
KW2 (1953-1971)
KW2 (1971-2006)
KW2 (2006-2017)
MH1 (1959-2004/05)
MH1 (2004/05-2019)
MH2 (1959-2004/05)
MH2 (2004/05-2019)

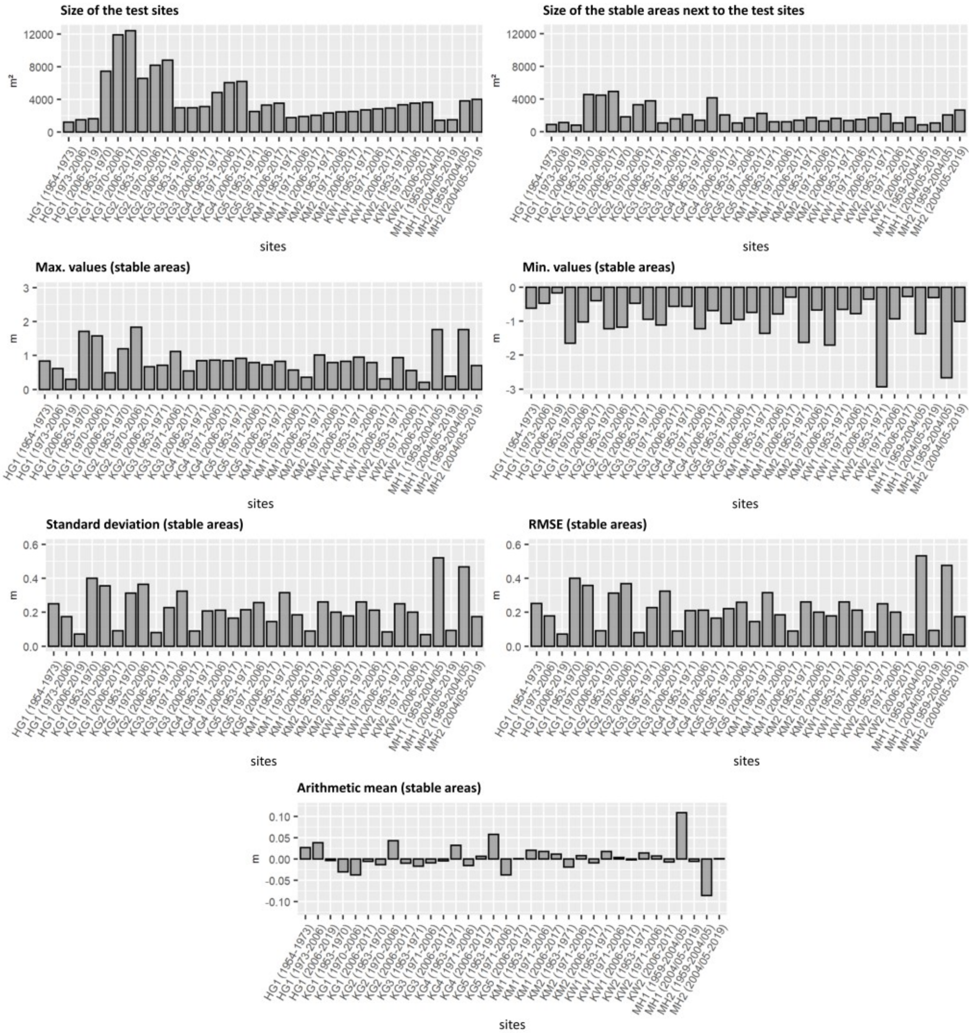

Figure 4:~~-~~ Statistical analysis of the uncertainty assessment: (a) Size of the test sites, (b) size of the stabe areas next to the test sites, (c) max. values (stable areas), (d) min. values (stable areas), (e) standard deviation (stable areas), (f) RMSE (stable areas) and (g) arithmetic mean.~~Uncertainty assessment.~~

Formatiert: Schriftart: 9 Pt., Schriftfarbe: Automatisch

Formatiert: Schriftart: 9 Pt., Schriftfarbe: Automatisch

Formatiert: Schriftart: 9 Pt., Schriftfarbe: Automatisch

Formatiert: Schriftart: 9 Pt., Schriftfarbe: Automatisch

Formatiert: Schriftart: 9 Pt., Schriftfarbe: Automatisch

Formatiert: Schriftart: 9 Pt., Schriftfarbe: Automatisch

Formatiert: Schriftart: 9 Pt., Schriftfarbe: Automatisch

Formatiert: Schriftart: 9 Pt., Schriftfarbe: Automatisch

To determine the uncertainty of the sediment volume change (total sediment output, Figure 7), the error propagation method for uncorrelated, correlated and systematic error according to Anderson (2019) was applied. ~~-~~No threshold has been set for the level of detection of the DoDs, as Anderson (2019) clearly recommends not using this for volumetric calculations as it leads to bias in the results. ~~We chose not to threshold our DoDs by a Level of Detection following Anderson's (2019) clear recommendation not to apply thresholding to net volumetric change analysis where thresholding can lead to biased results.~~

For the final determination of the total error, the following formula was applied Eq. (1):

$$\sigma_v = \sqrt{\sigma_{v,re}^2 + \sigma_{v,sc}^2 + \sigma_{v,sys}^2}, \qquad (1)$$

where $\sigma_{v,re}$ is the uncorrelated error, $\sigma_{v,sc}$ spatially correlated error and $\sigma_{v,sys}$ systematic error.

3.2 Derivation of the regression lines

In this study, we followed the sediment contributing area ~~SCA~~ approach of Neugirg et al. (2015a; 2015b; 2016) and Dusik et al. (2019), who applied this approach at the slope scale and replaced real sediment traps in the channels, as originally based on the work of Haas (2008) and Haas et al. (2011) using the *sediment contributing area model*, ~~-~~ with so-called virtual sediment traps ~~(VSTs)~~ in modelled channels in a DEM (Fig. 5). ~~The *SCA model* represents a set of simple DEM-based rules according to Heinimann et al. (1998) for delineating those geomorphologically active areas that potentially deliver sediment to the channel network (and hence constitute the sediment contributing area of the latter). This approach is similar to the "effective catchment area" proposed by Fryirs et al. (2007) and Fryirs (2013). By selecting different parameters related to topography and landcover information, namely the minimum channel gradient threshold (for longitudinal (de-)coupling), the minimum slope gradient threshold (for lateral (de-)coupling), the maximum distance from channel (slope length) and a weighting of the vegetation cover (representing the role impedance of vegetation as a disturbing factor into sediment transport), Haas (2008) and Haas et al. (2011) reduced the hydrological catchment accordingly to the sediment supplying and thus the sediment contributing area (SCA). A correlation between the size of the SCA, which thus corresponds to a subset of the hydrological catchment, and the computed sediment yield (determined by sediment traps in the channels) could be shown, but no correlation between the size of the hydrological catchment and the sediment yield. This shows that only a certain part within a hydrological catchment is geomorphologically active, providing sediment to the channels and subsequently transporting it downstream, as covered areas and areas with low gradients (hillslope and channel sections) reduce sediment connectivity within a catchment. Linear regression analysis was used to show this significant correlation, which is formulated as Eq. (2):~~

~~$y = \text{intercept} + \text{slope} * x,$ (2)~~

~~where *y* is (log.) mean annual bedload sediment yield and x (log.) SCA.~~

Formatiert: Schriftart: 10 Pt., Schriftfarbe: Automatisch

Formatiert: Schriftart: 10 Pt., Schriftfarbe: Automatisch

Formatiert: Schriftart: Kursiv

The *sediment contributing area ~~SCA~~ model* uses an empirical relationship between log. sediment contributing area as the independent variable and log. mean annual bedload sediment yield as the dependent variable. Thus, the sediment contributing area ~~SCA~~ can be used as a predictor of sediment delivery in alpine catchments.

Linear regression analysis was used to show this significant correlation, which is formulated as Eq. (2):

$$\mathrm{y} = \mathrm{intercept} + \mathrm{slope} * \mathrm{x}, \qquad (2)$$

where *y* is (log.) mean annual bedload sediment yield and x (log.) sediment contributing area.

This has already been confirmed in several studies in both small and large catchments (ranging from hectare to square kilometres) and in different regions such as the Northern Calcareous Alps (Haas, 2008; Haas et al., 2011; Sass et al., 2012; Huber et al., 2015) and the French Northern Alps/Prealps (Altmann et al., 2021).

Finally it can be stated that a linear dependency of two variables x and y on a log-log-scale has a fundamentally different behavior than a usual linear dependency. In our case, we have ~~—~~ $\mathrm{y} = \log($sediment ~~SY~~yield$)$ and $\mathrm{x} = \log($~~SCA~~sediment contributing area$)$. Back-transformation of Eq. (2) using the *exp* function yields gives the following relation between ~~SCA~~ sediment contributing area and sediment yield~~SY~~, Eq. (3):

sediment yield~~SY~~ $= \exp(\mathrm{intercept}) *$ sediment contributing ~~SC~~area~~A~~$^{\mathrm{slope}}$ (3)

Thus, the relation between ~~SY~~ sediment yield and sediment contributing area ~~SCA~~ is a polynomial of the form $\mathrm{y} = a * \mathrm{x}^{b}$. In particular, the slope in the log-log model represents the exponent of the polynomial in the standard model. The relation between ~~SY~~ sediment yield and sediment contributing area ~~SCA~~ is (nearly) linear if slope is (close to) one. In this case, the exponential of the intercept in the log-log model represents the slope of the linear relation in the standard model, meaning that independent of the actual size of the sediment contributing area~~SCA~~, one square meter provides the same amount of ~~SY~~sediment yield, given by $exp(intercept)$. On the other hand, if the slope in the log-log model is considerably greater than one, the standard model shows a polynomial behaviour, meaning that in the same ~~AOI~~site, increasing the sediment contributing area ~~SCA~~ provides more sediment yield ~~SY~~ per square meter.

The steps of the sediment contributing area ~~SCA~~ approach of this study are composed as follows and were implemented in SAGA LIS and R. The elevation changes in DoDs (using no threshold) generated from multitemporal data were routed downslope and accumulated using the D8 algorithm (O'Callaghan and Mark, 1984). The resulting accumulated DoD values (accDoD) in every raster cell corresponds to the net volume of the sediment balance within its contributing area. On steep slopes, accDoD will be negative and represents the sediment yield of this contributing area (Pelletier and Orem, 2014); if it is close to zero, it means that all eroded sediment has been re-deposited within the contributing area. As in the previous sediment contributing area ~~SCA~~ studies by Neugirg et al. (2015a; 2015b; 2016), the application of the parameters used in the original *sediment contributing area ~~SCA~~ model* (Haas, 2008; Haas et al., 2011), which lead to the reduction of the hydrological catchment to the sediment contributing area~~SCA~~, is omitted because the ~~AOIs~~ sites and the modelled channels are consistently

Formatiert: Schriftart: Kursiv

Formatiert: Schriftart: Kursiv

steep, uncovered and have short slope lengths, which makes this reduction obsolete. Therefore, the sediment contributing area ~~SCA~~ is identical to the catchment area ~~(CA)~~ in this study.

In detail, channel initiation points were delineated using a threshold of 20 m² of the flow accumulation that was computed using the D8 algorithm (O'Callaghan and Mark, 1984). Channels that were shorter than 10 m were discarded. To ensure statistical independence through avoiding overlapping contributing areas, a stratified sampling scheme was adopted that included one randomly selected raster cell per channel. Pairs of values (sediment yield ~~SY~~ and the corresponding sediment contributing area ~~SCA~~ size) were randomly extracted from the corresponding channels ~~(representing the VSTs)~~ for each ~~AOI~~ site and a regression line were calculated accordingly. To quantify the uncertainty due to random selection, this sample was repeated 100 times, resulting in 100 regression models of sediment yield ~~SY~~ on sediment contributing area~~SCA~~.

Furthermore, we added two conditions and further developed the sediment contributing area ~~SCA~~ approach accordingly. In order to obtain more stable regression lines, the range of values of the sediment contributing area ~~SCA~~ size was divided into quartiles (with equal number of cells within the quartiles) to ensure a homogeneous distribution of the extracted values. Additionally samples that contained points with a high leverage (greater than 0.5) in the regression model were discarded, and the sampling was repeated until a number of 100 samples was reached.

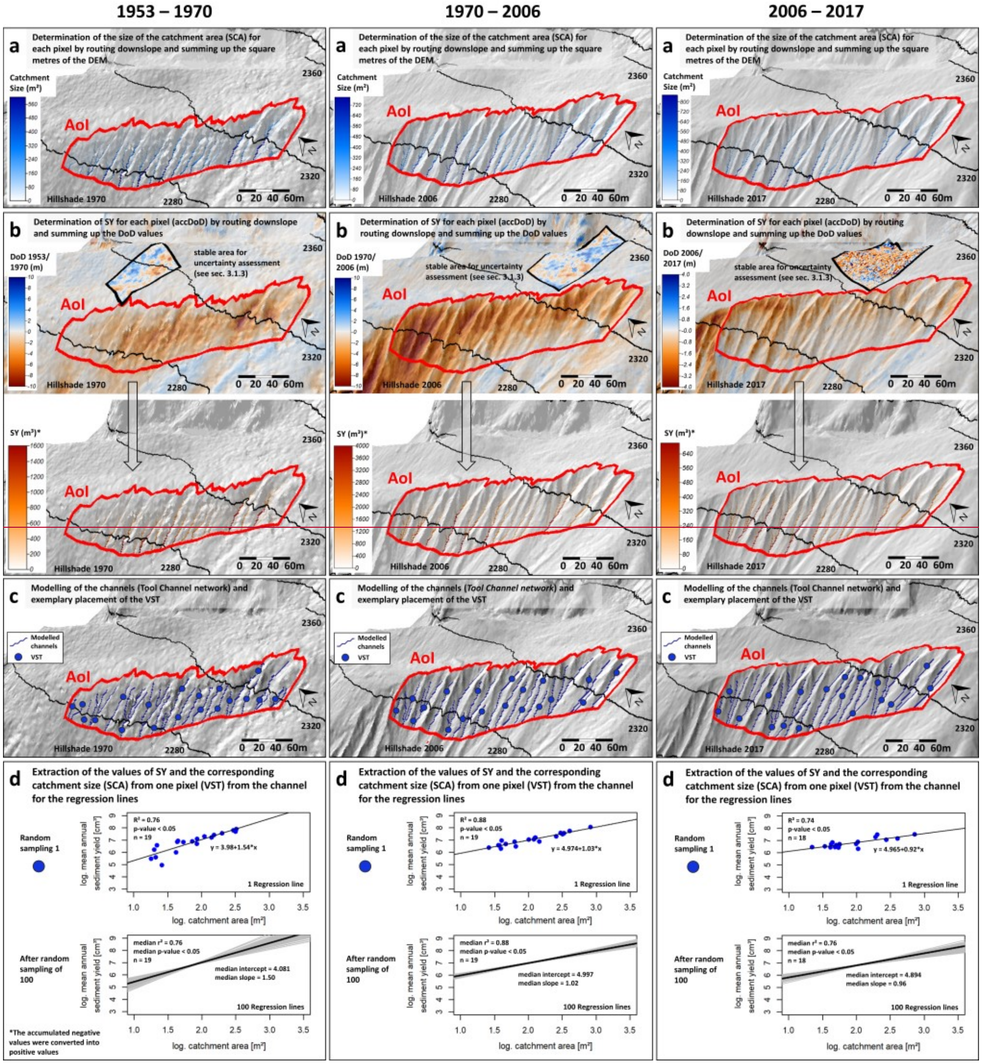
1953 – 1970
1970 – 2006
2006 – 2017
a
Determination of the size of the catchment area (SCA) for each pixel by routing downslope and summing up the square metres of the DEM
Catchment Size (m²)
AoI
Hillshade 1970
Hillshade 2006
Hillshade 2017
2360
2320
2280
0 20 40 60m
b
Determination of SY for each pixel (accDoD) by routing downslope and summing up the DoD values
DoD 1953/ 1970 (m)
DoD 1970/ 2006 (m)
DoD 2006/ 2017 (m)
stable area for uncertainty assessment (see sec. 3.1.3)
SY (m³)*
c
Modelling of the channels (Tool Channel network) and exemplary placement of the VST
Modelled channels
VST
d
Extraction of the values of SY and the corresponding catchment size (SCA) from one pixel (VST) from the channel for the regression lines
Random sampling 1
R² = 0.76
p-value < 0.05
n = 19
y = 3.98+1.54*x
R² = 0.88
p-value < 0.05
n = 19
y = 4.974+1.03*x
R² = 0.74
p-value < 0.05
n = 18
y = 4.965+0.92*x
1 Regression line
log. mean annual sediment yield [cm³]
log. catchment area [m²]
After random sampling of 100
median r² = 0.76
median p-value < 0.05
n = 19
median intercept = 4.081
median slope = 1.50
median r² = 0.88
median p-value < 0.05
n = 19
median intercept = 4.997
median slope = 1.02
median r² = 0.76
median p-value < 0.05
n = 18
median intercept = 4.894
median slope = 0.96
100 Regression lines
*The accumulated negative values were converted into positive values

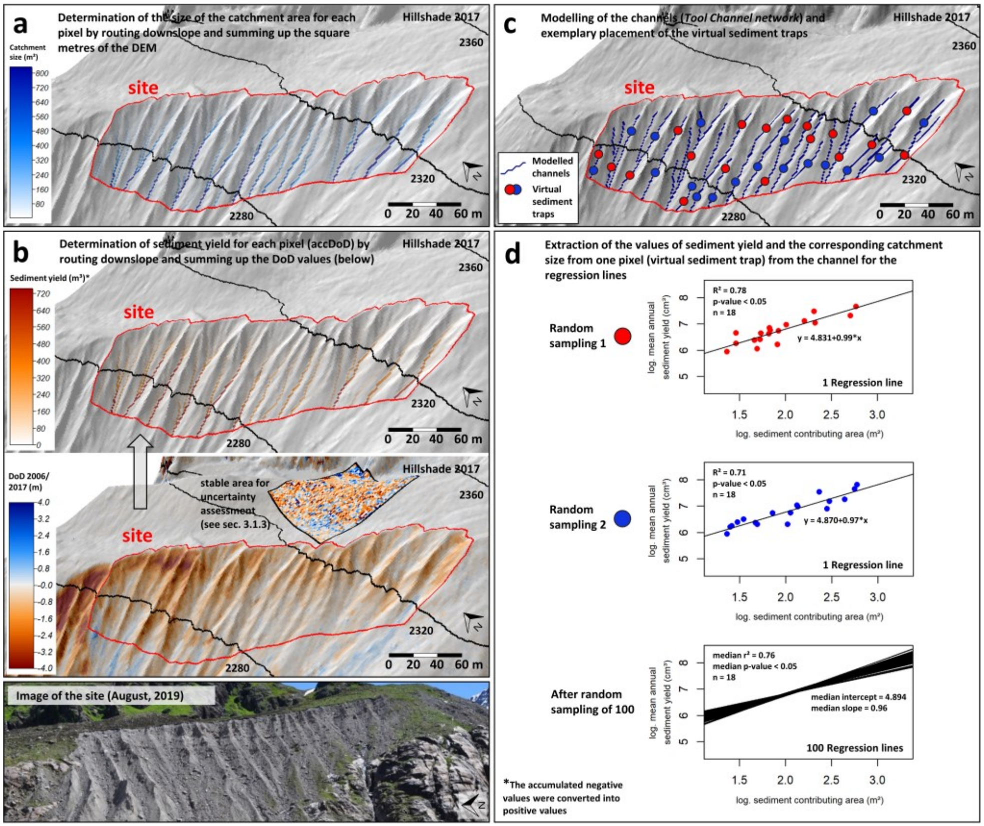

Figure 5: Derivation of the sediment contributing area approach using the example of test site KG2: (a) Determination of the size of the catchment area, (b) determination of sediment yield, (c) modelling of the channels and exemplary placement of the virtual sediment traps and (d) calculation of the regression lines.

~~Example derivation of the statistical relationship at AOI KG2.~~

3.3 Calculation of the sediment output

Additionally, the total sediment output volume, the mean annual sediment output (divided by the corresponding number of years) and the specific mean annual sediment output (additionally divided by the area of the ~~AOI~~site) were calculated for each ~~AOI~~ site and time period~~epoch~~.

The following equation was used for this (4):

$$V = \sum D oD * L^2, \quad (4)$$

where Σ DoD is the sum of the corresponding DoD subset values and L^2 is the cell size.

3.4 Generation of meteorological data

Using data generated with a regional climate model (RCM), the influence of the changes in climate forcing (air temperature and precipitation) on morphodynamics was investigated. For dynamical downscaling of climate data for the beginning of the study period until 2015, we used the Advanced Research Version of the Weather Research and Forecasting (ARW-WRF) model (version 4.3), which is based on fully compressible and non-hydrostatic equations (Skamarock and Klemp, 2008). The 20th Century Reanalysis version 3 (20CRv3) dataset (Compo et al., 2011; Giese et al., 2016; Slivinski et al., 2019), with a spatial and temporal resolution of 1°x1° and three hours, respectively, was used as driving data (initial and boundary conditions). The simulation was performed in three nested domains with grid spacing of 18- (Domain 1), 6- (Domain 2), and 2-km (Domain 3). For our simulations, we mainly used the physics and dynamics options proposed by Collier and Mölg (2020), and are listed in Table 5. However, the Noah land surface model, prescribed eta levels by Collier et al. (2019), and the 24 United States Geological Survey (USGS) land use categories were used. The temporal resolution of simulated data in D3 is 1 hour for temperature and 15 minutes for precipitation.

Table 5: Overview of the WRF configuration.

Domain configuration	
Horizontal grid spacing	18-, 6-, 2-km (D1, D2 and D3)
Grid dimensions	190 x 190, 151 x 142, 121 x 139
Lateral boundary condition	variable (20CRv3 at 1°x1°, 3-hour)
Time step	90, 30, 10 s
Vertical levels	50
Model top pressure	10hPa
Model physics	
Microphysics	Morrison (Morrison et al., 2009)
Cumulus	Kain-Fritsch (none in D3) (Kain, 2004)
Radiation	RRTMG (Iacono et al., 2008)
Planetary boundary layer	Yonsei State University (Hong et al., 2006)
Atmospheric surface layer	Monin Obukhov (Jiménez et al., 2012)
Land surface	Noah (Chen and Dudhia, 2001)
Dynamics	
Top boundary conditions	Rayleigh damping
Diffusion	Calculated in physical space

~~For the period from 2016 to the end of the study period (2017/2019), the ERA5 reanalysis dataset (Hersbach et al., 2018) was used (spatial resolution: 55 km, temporal resolution: 1 hour). The different meteorological datasets were combined and divided into the corresponding study epochs.For this purpose the temporal resolution of the precipitation data simulated with WRF was adjusted to one hour to fit the ERA5 temporal resolution.~~ The simulated temperature and precipitation data were extracted at the location of each of the five glacier ~~forefield~~ foreland (Figure 1). These are the centres of the respective ~~AOIs~~ sites and represent the corresponding glacier foreland~~forefield~~. In addition, a corresponding elevation correction of the climate data was applied for temperature.

For the analysis, we used the mean annual air temperature (2 metres above ground), as well as the corresponding trends and the mean number of ice days (days with maximum temperature <0°C). In addition, the number of warm air inflows from October to May was determined in order to identify corresponding snowmelt processes on the ~~AOIs~~sites. A warm air inflow is defined as a period of at least ~~3~~ 2 days in which more than 70% is above 0°C, following a previously colder period of ~~5~~ 3 days (100% below 0°C). In addition, the precipitation patterns were analysed. For this purpose, the mean annual precipitation totals, the mean annual winter (October to May) and the mean annual summer precipitation totals (June to September) as well as the corresponding trends were determined in order to identify seasonal changes. Furthermore, various continuing classes (4 mm for one-hour resolution and 10 mm classes for daily totals) were used to analyse corresponding changes in individual extreme events and daily precipitation totals. Individual precipitation events were defined as one event, regardless of length, if they were contiguous throughout, and were separated if there was no precipitation for at least one hour. To minimise the noise generated in the data, both datasets were also filtered for extremely small events by changing the values from <0.01 mm to 0 mm. The calculation of the mean annual winter precipitation was always carried out over the entire winter. For example, for the winter of 1953, data from October 1952 to May 1953 was included. The average summer precipitation was calculated accordingly from June 1953 to September 1953. Furthermore, precipitation was differentiated into snow and rain events. The determination of a threshold to distinguish rain from snowfall is very dynamic in mountainous regions and difficult to estimate. However, the difference between rain to snow depends mainly on surface air temperature as well as air humidity, with snow occurring mainly between 0 and 3°C (Froidurot et al., 2014) and the lower the humidity, the higher the probability of snowfall is. In this study, the threshold from rain to snow was defined at ≤0°C, as below this temperature rain is almost excluded (Froidurot et al., 2014; Fehlmann et al., 2018).

4 Results

4.1 Sediment-Contributing-Area ~~(SCA)~~ approach

All determined regression lines show a positive correlation between log mean annual sediment yield ~~(SY)~~ and log sediment contributing area ~~(SCA)~~ (Figure 6, Appendix A), which means that sediment yield ~~SY~~ increases with the corresponding sediment contributing area~~SCA~~. In the following, only the median of the 100 regression lines (median slope) of all ~~AOIs~~ sites and time periods ~~epochs~~ is used to qualitatively describe corresponding differences. Mostly, there is a decrease in sediment yield ~~SY~~ between the different time periods ~~epochs~~ and a decrease of the slopes of the regression lines, which is due to a decrease in sediment yield ~~SY~~ per square metre of the ~~AOIs~~sites. ~~-~~With regard to section 3.3, a decreasing intercept together with an almost constant, although slightly decreasing, slope close to one can be seen over the different time periods in the log-log model, indicating that the relation between sediment contributing area and sediment yield remains almost constant.~~With regard to section 3.3, a decreasing intercept together with an almost constant slope close to one over the different epochs (in the log-log model) (although with a slightly decreasing slope) indicates that the relation between SCA and SY stays nearly constant.~~ The ~~AOI's~~ sites KG3, KG4, KM1, KM2 and KW2 show such a behaviour. On the other hand, the areas KG1, KG2, KG5, KW1 and MH2 show clearly larger differences in the time periods~~epochs~~. In the earliest time period~~epoch~~, the slopes considerably larger than one (in the log-log model) show polynomial behaviour, which means that in the same ~~AOI~~ site an increasing sediment contributing area ~~SCA~~ provides clearly more sediment yield ~~SY~~ per square meter. In the later time periods~~epochs~~, the slopes also tend towards one, so that the models of the different groups become similar. In addition to this general trend (ten ~~AOIs~~sites), an increase in sediment yield ~~SY~~ and an increase in the slope of the regression line for ~~AOI~~ site HG1 were observed, showing an increase in sediment dynamics over the time periods ~~epochs~~ in this case, which is in contrast to the previous observations. ~~AOI~~ Site MH1 shows a similar level of sediment yield ~~SY~~ (between the time periods~~epochs~~) with higher slopes of the regression lines, also indicating an increase in sediment yield~~SY~~. Furthermore, slopes of the regression lines below 1 occur in all time periods~~epochs~~, but especially in the second and third.

Formatiert: Schriftart: 10 Pt., Schriftfarbe: Automatisch

Formatiert: Schriftart: 10 Pt., Schriftfarbe: Automatisch

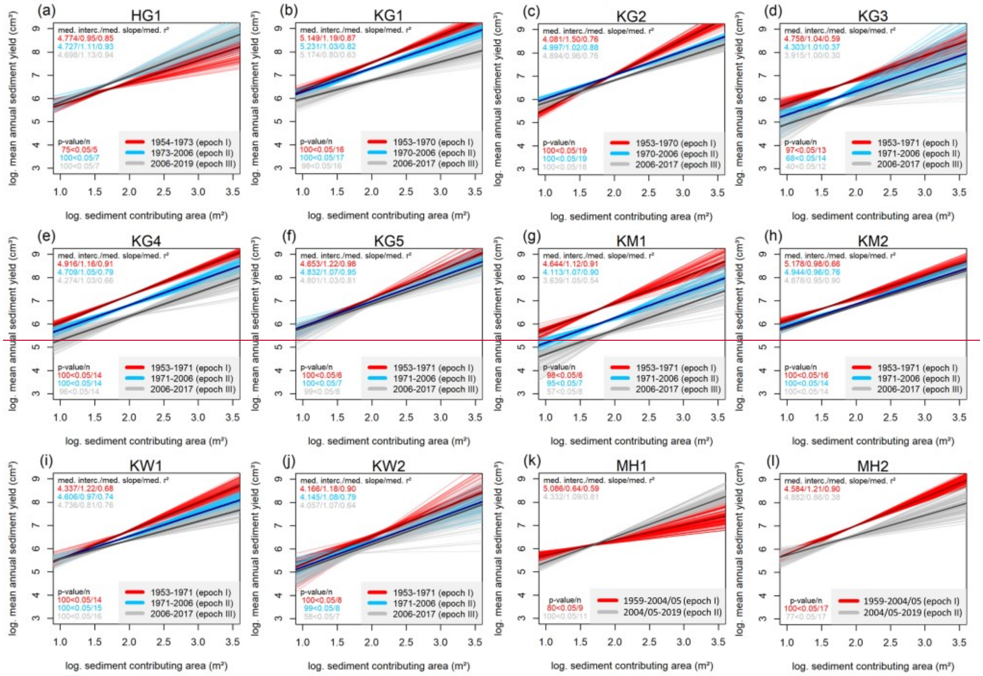
(a)
HG1
med. interc./med. slope/med. r²
4.774/0.95/0.85
4.727/1.11/0.93
4.698/1.13/0.94
p-value/n
75<0.05/5
100<0.05/7
100<0.05/7
1954-1973 (epoch I)
1973-2006 (epoch II)
2006-2019 (epoch III)
(b)
KG1
med. interc./med. slope/med. r²
5.149/1.19/0.87
5.231/1.03/0.82
5.174/0.80/0.63
p-value/n
100<0.05/16
100<0.05/17
98<0.05/16
1953-1970 (epoch I)
1970-2006 (epoch II)
2006-2017 (epoch III)
(c)
KG2
med. interc./med. slope/med. r²
4.081/1.50/0.76
4.997/1.02/0.88
4.894/0.96/0.76
p-value/n
100<0.05/19
100<0.05/19
100<0.05/18
1953-1970 (epoch I)
1970-2006 (epoch II)
2006-2017 (epoch III)
(d)
KG3
med. interc./med. slope/med. r²
4.758/1.04/0.59
4.303/1.01/0.37
3.915/1.00/0.30
p-value/n
97<0.05/13
68<0.05/14
40<0.05/12
1953-1971 (epoch I)
1971-2006 (epoch II)
2006-2017 (epoch III)
(e)
KG4
med. interc./med. slope/med. r²
4.916/1.16/0.91
4.709/1.05/0.79
4.274/1.03/0.66
p-value/n
100<0.05/14
100<0.05/14
96<0.05/14
1953-1971 (epoch I)
1971-2006 (epoch II)
2006-2017 (epoch III)
(f)
KG5
med. interc./med. slope/med. r²
4.653/1.22/0.98
4.832/1.07/0.95
4.801/1.03/0.81
p-value/n
100<0.05/6
100<0.05/7
99<0.05/8
1953-1971 (epoch I)
1971-2006 (epoch II)
2006-2017 (epoch III)
(g)
KM1
med. interc./med. slope/med. r²
4.644/1.12/0.91
4.113/1.07/0.90
3.639/1.05/0.54
p-value/n
98<0.05/6
95<0.05/7
57<0.05/8
1953-1971 (epoch I)
1971-2006 (epoch II)
2006-2017 (epoch III)
(h)
KM2
med. interc./med. slope/med. r²
5.178/0.98/0.66
4.944/0.96/0.76
4.878/0.95/0.90
p-value/n
100<0.05/16
100<0.05/14
100<0.05/14
1953-1971 (epoch I)
1971-2006 (epoch II)
2006-2017 (epoch III)
(i)
KW1
med. interc./med. slope/med. r²
4.337/1.22/0.68
4.606/0.97/0.74
4.736/0.81/0.76
p-value/n
100<0.05/14
100<0.05/15
100<0.05/16
1953-1971 (epoch I)
1971-2006 (epoch II)
2006-2017 (epoch III)
(j)
KW2
med. interc./med. slope/med. r²
4.166/1.18/0.90
4.145/1.08/0.79
4.057/1.07/0.64
p-value/n
100<0.05/8
99<0.05/8
58<0.05/7
1953-1971 (epoch I)
1971-2006 (epoch II)
2006-2017 (epoch III)
(k)
MH1
med. interc./med. slope/med. r²
5.086/0.64/0.59
4.332/1.09/0.81
p-value/n
80<0.05/9
100<0.05/11
1959-2004/05 (epoch I)
2004/05-2019 (epoch II)
(l)
MH2
med. interc./med. slope/med. r²
4.584/1.21/0.90
4.882/0.86/0.38
p-value/n
100<0.05/17
77<0.05/17
1959-2004/05 (epoch I)
2004/05-2019 (epoch II)
log. mean annual sediment yield (cm³)
3
4
5
6
7
8
9
log. sediment contributing area (m²)
1.0
1.5
2.0
2.5
3.0
3.5

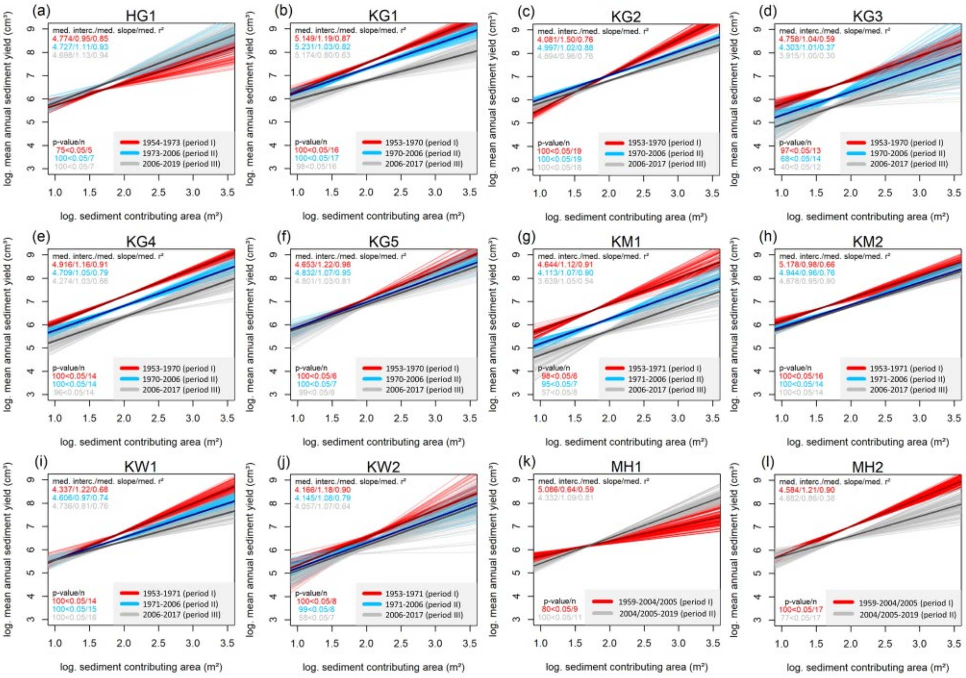

Figure 6: Relationships between log sediment contributing area ~~SCA~~ and log sediment yield ~~SY~~ yield for 100 samples of each ~~AOI~~ site and the corresponding ~~epochs~~time periods. In addition, the median regression line (median slope) is represented by a slightly thicker and darker line.

4.2 Volume calculations of the sediment output

The analyses of the sediment output of the ~~AOIs~~ sites confirm the results of the sediment contributing area ~~SCA~~ approach (Figure 7). In general, there is a clear and continuous decrease in mean annual sediment yield ~~SY~~ of ten ~~AOIs~~ sites over the different time periods~~epochs~~. In contrast to this trend, ~~AOI~~ site HG1 shows a clear increase in mean annual sediment yield~~SY~~. Site ~~AOI~~ MH1 also shows an increase, but at a very low level, which can also be described as a geomorphic activity of a similar level. In total, the mean annual sediment output decreases across the different time periods~~epochs~~. Nevertheless, there is also very high temporal and spatial variability of this change on the ~~AOIs~~ sites HG1 and MH1, which also shows a clear increase in geomorphic activity as well as a slight increase (respectively activity at the same level).

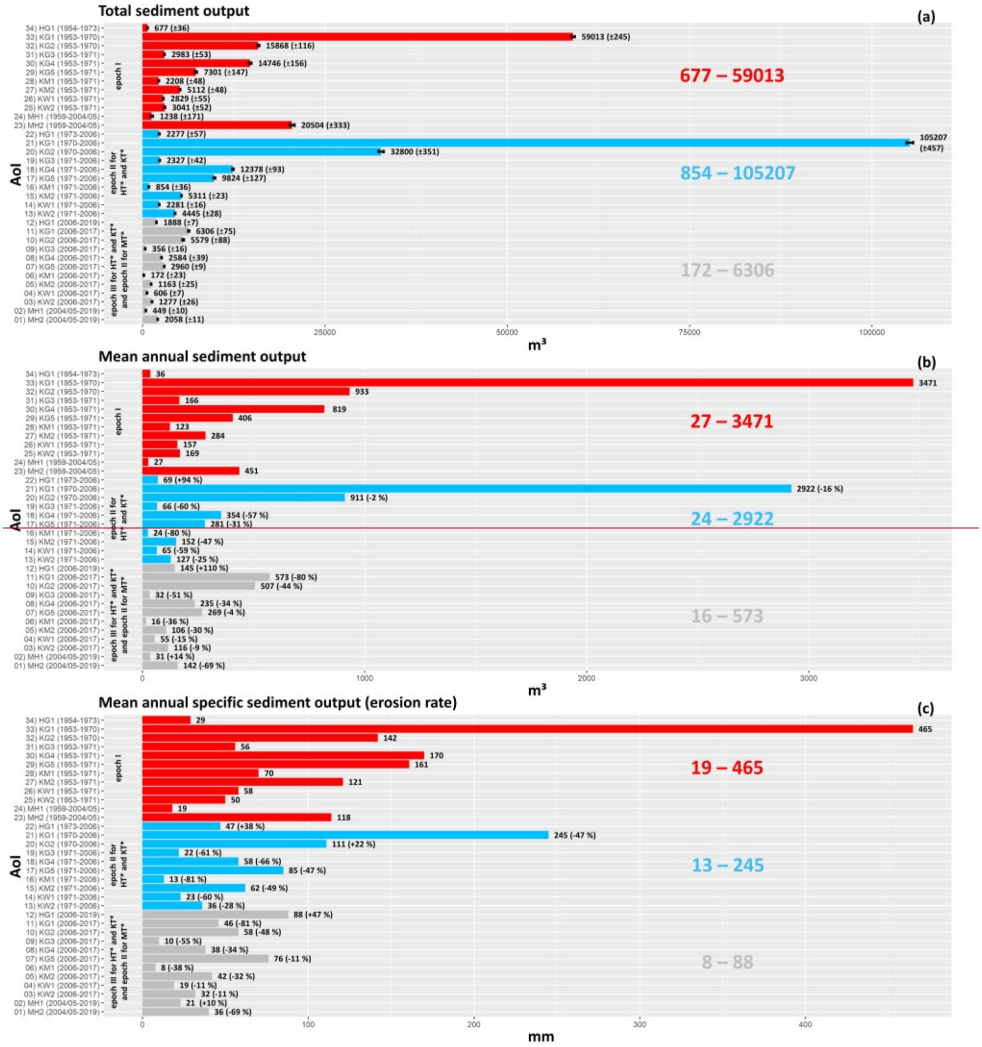
Total sediment output
(a)
34) HG1 (1954-1973)
33) KG1 (1953-1970)
32) KG2 (1953-1970)
31) KG3 (1953-1971)
30) KG4 (1953-1971)
29) KG5 (1953-1971)
28) KM1 (1953-1971)
27) KM2 (1953-1971)
26) KW1 (1953-1971)
25) KW2 (1953-1971)
24) MH1 (1959-2004/05)
23) MH2 (1959-2004/05)
22) HG1 (1973-2006)
21) KG1 (1970-2006)
20) KG2 (1970-2006)
19) KG3 (1971-2006)
18) KG4 (1971-2006)
17) KG5 (1971-2006)
16) KM1 (1971-2006)
15) KM2 (1971-2006)
14) KW1 (1971-2006)
13) KW2 (1971-2006)
12) HG1 (2006-2019)
11) KG1 (2006-2017)
10) KG2 (2006-2017)
09) KG3 (2006-2017)
08) KG4 (2006-2017)
07) KG5 (2006-2017)
06) KM1 (2006-2017)
05) KM2 (2006-2017)
04) KW1 (2006-2017)
03) KW2 (2006-2017)
02) MH1 (2004/05-2019)
01) MH2 (2004/05-2019)
epoch I
epoch II for HT* and KT*
epoch III for HT* and KT* and epoch II for MT*
AoI
677 (±36)
59013 (±245)
15868 (±116)
2983 (±53)
14746 (±156)
7301 (±147)
2208 (±48)
5112 (±48)
2829 (±55)
3041 (±52)
1238 (±171)
20504 (±333)
2277 (±57)
105207 (±457)
32800 (±351)
2327 (±42)
12378 (±93)
9824 (±127)
854 (±36)
5311 (±23)
2281 (±16)
4445 (±28)
1888 (±7)
6306 (±75)
5579 (±88)
356 (±16)
2584 (±39)
2960 (±9)
172 (±23)
1163 (±25)
606 (±7)
1277 (±26)
449 (±10)
2058 (±11)
677 – 59013
854 – 105207
172 – 6306
0
25000
50000
75000
100000
m³
Mean annual sediment output
(b)
AoI
epoch I
epoch II for HT* and KT*
epoch III for HT* and KT* and epoch II for MT*
36
3471
933
166
819
406
123
284
157
169
27
451
69 (+94 %)
2922 (-16 %)
911 (-2 %)
66 (-60 %)
354 (-57 %)
281 (-31 %)
24 (-80 %)
152 (-47 %)
65 (-59 %)
127 (-25 %)
145 (+110 %)
573 (-80 %)
507 (-44 %)
32 (-51 %)
235 (-34 %)
269 (-4 %)
16 (-36 %)
106 (-30 %)
55 (-15 %)
116 (-9 %)
31 (+14 %)
142 (-69 %)
27 – 3471
24 – 2922
16 – 573
0
1000
2000
3000
m³
Mean annual specific sediment output (erosion rate)
(c)
AoI
epoch I
epoch II for HT* and KT*
epoch III for HT* and KT* and epoch II for MT*
29
465
142
56
170
161
70
121
58
50
19
118
47 (+38 %)
245 (-47 %)
111 (+22 %)
22 (-61 %)
58 (-66 %)
85 (-47 %)
13 (-81 %)
62 (-49 %)
23 (-60 %)
36 (-28 %)
88 (+47 %)
46 (-81 %)
58 (-48 %)
10 (-55 %)
38 (-34 %)
76 (-11 %)
8 (-38 %)
42 (-32 %)
19 (-11 %)
32 (-11 %)
21 (+10 %)
36 (-69 %)
19 – 465
13 – 245
8 – 88
0
100
200
300
400
mm

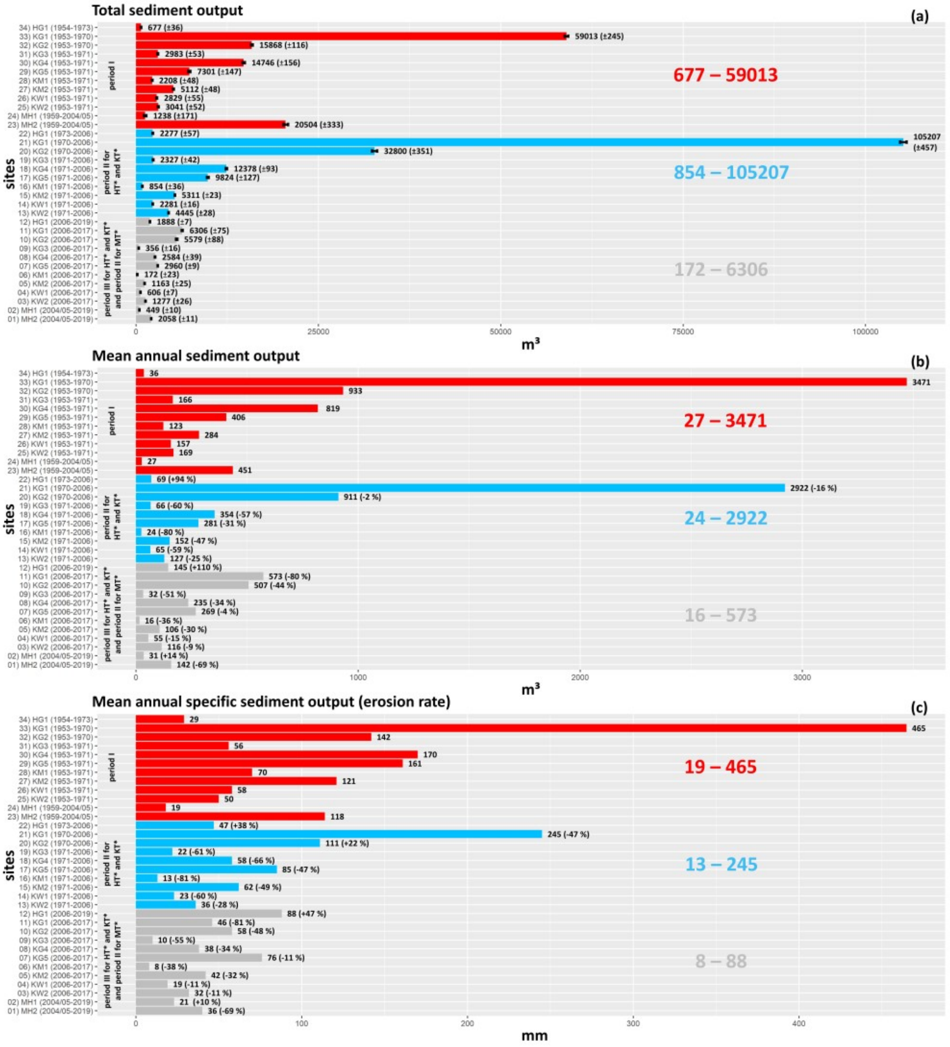

Figure 7. Bar plots of total sediment output (with error range according to Anderson (2019), see sect. 3.1.3 and 3.4), mean annual sediment output and mean annual specific sediment output (erosion rate) of each ~~AOI~~ site and time period~~epoch~~.

4.2 Meteorological regime

4.2.1 Air temperature

The mean annual air temperature (2 m above ground) of all selected positions of the glacier forelands ~~forefields~~ shows a statistically significant warming trend over the entire study period of ~~60~~56, 6~~4~~1 and 6~~5~~2 years (Figure 8). Overall, there is a positive total change of +1.66~~75~~°C (annual trend +0.03; p-value <0.05; R² 0.35~~9~~) for the Horlachtal/Grastalferner glacier forelands~~forefield~~, +1.~~68~~36°C (annual trend +0.0~~3~~2; p-value <0.05; R² 0.~~–~~32~~8~~) for the Kaunertal/Gepatschferner glacier foreland~~forefield~~, +1.74~~0~~°C (annual trend +0.02~~3~~; p-value <0.05; R² 0. 3~~8~~2) for the Kaunertal/Gepatschferner Münchner Abfahrt glacier foreland~~forefield~~, for the Kaunertal Weißseeferner glacier foreland ~~forefield~~ of +1.~~64~~55°C (annual trend +0.02~~3~~; p-value <0.05; R² 0.33~~6~~) and for the Martelltal Hohenferner glacier foreland ~~forefield~~ of +1.41~~2.23~~°C (annual trend 0.0~~4~~2; p-value <0.05; R² 0.~~45~~34).

Formatiert: Schriftfarbe: Automatisch

Formatiert: Schriftfarbe: Automatisch

Formatiert: Schriftfarbe: Automatisch

Formatiert: Schriftfarbe: Automatisch

Formatiert: Schriftfarbe: Automatisch

Formatiert: Schriftfarbe: Automatisch

Formatiert: Schriftfarbe: Automatisch

Formatiert: Schriftfarbe: Automatisch

Formatiert: Schriftfarbe: Automatisch

Formatiert: Schriftfarbe: Automatisch

Formatiert: Schriftfarbe: Automatisch

Formatiert: Schriftfarbe: Automatisch

Formatiert: Schriftfarbe: Automatisch

Formatiert: Schriftfarbe: Automatisch

Formatiert: Schriftfarbe: Automatisch

Formatiert: Schriftfarbe: Automatisch

Formatiert: Schriftfarbe: Automatisch

Formatiert: Schriftfarbe: Automatisch

Formatiert: Schriftfarbe: Automatisch

Formatiert: Schriftfarbe: Automatisch

Formatiert: Schriftfarbe: Automatisch

445

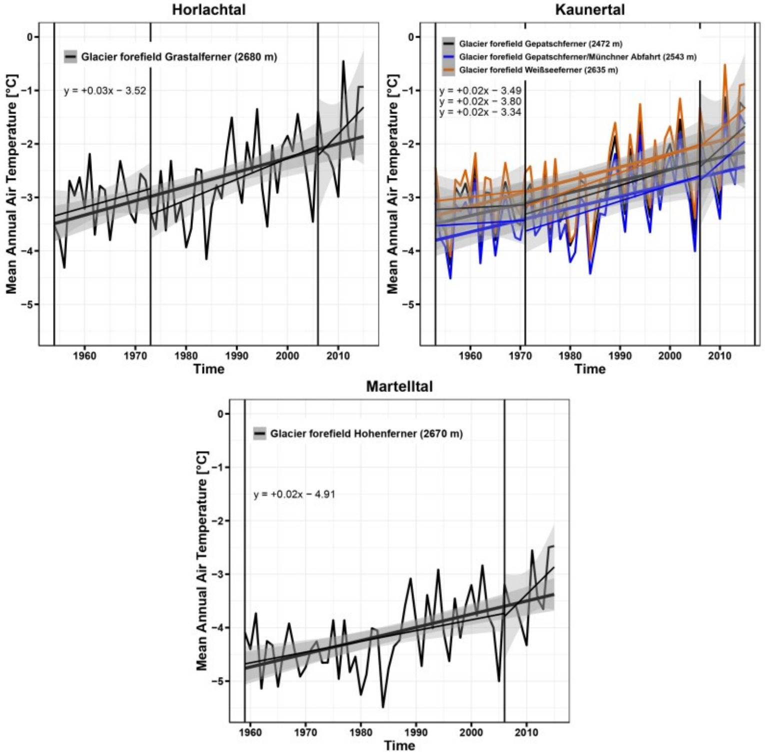
Horlachtal
Glacier forefield Grastalferner (2680 m)
y = +0.03x − 3.52
Kaunertal
Glacier forefield Gepatschferner (2472 m)
Glacier forefield Gepatschferner/Münchner Abfahrt (2543 m)
Glacier forefield Weißseeferner (2635 m)
y = +0.02x − 3.49
y = +0.02x − 3.80
y = +0.02x − 3.34
Martelltal
Glacier forefield Hohenferner (2670 m)
y = +0.02x − 4.91
Mean Annual Air Temperature [°C]
0
−1
−2
−3
−4
−5
Time
1960
1970
1980
1990
2000
2010

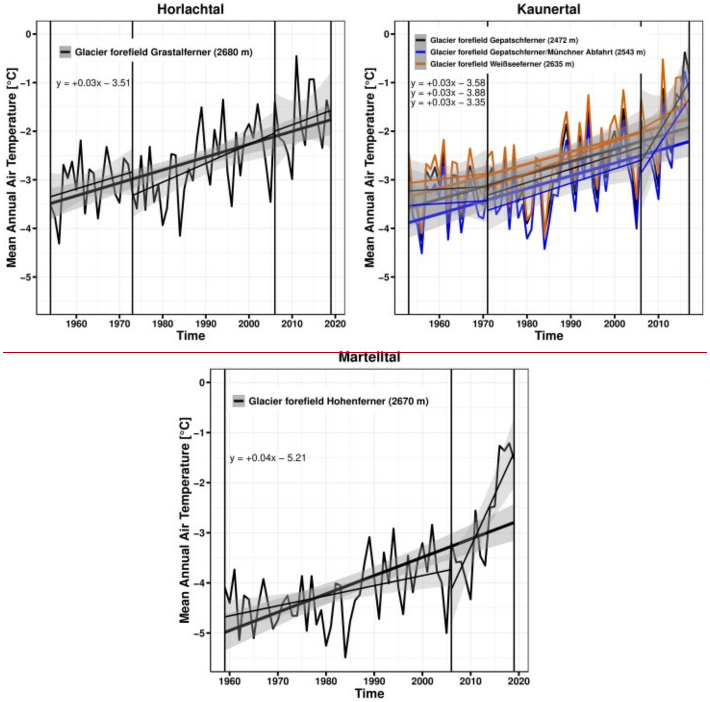

Figure 8: Mean annual 2 meter air temperature of the glacier forelands~~fields~~ within the study ~~epochs~~ periods (95% confidence interval is included).

The analysis of the mean annual ice days shows a decrease between the time periods~~epochs~~, especially from the second to the third time period ~~epoch~~ (in the Martelltal from the first to the second), with a decrease in ice days between ~~18~~12.4~~.4~~ and ~~20.7~~60.1 days, which corresponds to almost ~~three~~eight weeks (Figure 9).

The analysis of the mean annual warm air inflows shows a general increase of these, especially from the second to the third period (Grastalferner, Gepatschferner, Hohenferner (first to second period)). In the glacier foreland of the Gepatschferner/MA the analysis shows a decrease from the first to the second time period, but a more pronounced increase from the second to the third time period. In the glacier foreland of the Weißseeferner, there is first a slight increase, followed by a slight decrease.

~~The analysis of the mean annual warm air inflows shows a decrease from the first to the second epoch in the glacier forefields of Grastalferner, Gepatschferner and Gepatschferner/MA, and a more pronounced increase from the second to the third epoch. In the glacier forefield of Weißseeferner ,there is a consistent increase, the latter being equally more pronounced, whereas in~~

Formatiert: Schriftfarbe: Automatisch

Formatiert: Schriftfarbe: Automatisch

Formatiert: Schriftfarbe: Automatisch

Formatiert: Schriftfarbe: Automatisch

Formatiert: Schriftfarbe: Automatisch

Formatiert: Schriftfarbe: Rot

~~Martelltal there is only a slight increase. Thus, the number of warm air inflows has generally increased.~~

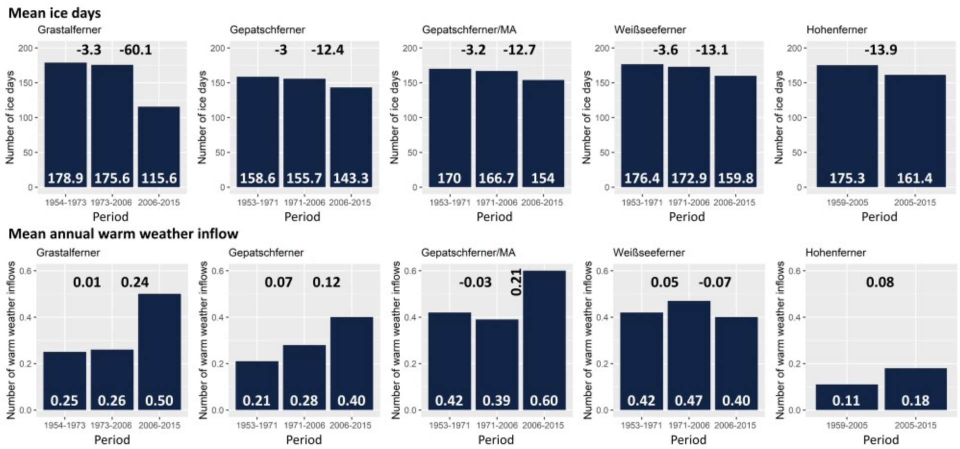

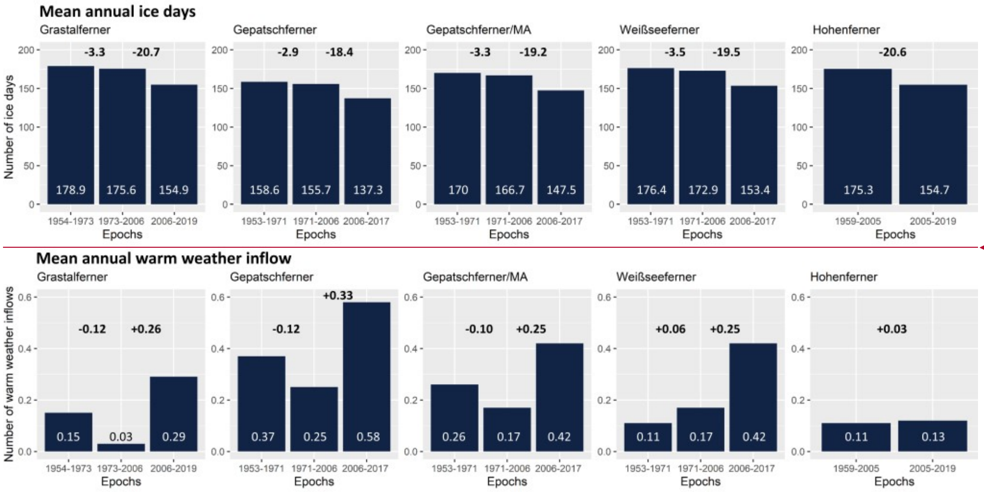

Figure 9: Mean annual ice days and mean annual warm weather inflows with the corresponding changes between ~~epochs~~time periods.

Formatiert: Schriftfarbe: Rot

Formatiert: Block

4.2.2 Precipitation

Over the entire time periods ~~epochs~~ (~~60~~56, ~~64~~61 and 6~~5~~2 years), all study areas show a decreasing trend in mean annual, mean summer and mean winter precipitation (with the exception of winter precipitation in the Kaunertal and summer precipitation in the Martelltal, which shows a positive trend) (Figure 10). ~~However, only the changes in winter precipitation (entire study period), summer precipitation (second epoch: 2004/2005-2019) in the Martelltal (Hohenferner glacier forefield) and annual precipitation (third epoch: 2006-2019) in the Horlachtal (Grastalferner glacier forefield) are statistically significant, although the latter both cover only 13 and 14 years.~~ In the Horlachtal, the first two time periods ~~epochs~~ show a decreasing trend in precipitation, while the third time period ~~epoch~~ shows an increase in precipitation (mean annual, winter and summer precipitation)~~, which is significantly more pronounced in summer than in winter.~~

In the Kaunertal, winter precipitation shows a slight increase in the first time period ~~epoch~~ and a stronger decrease in summer precipitation. The second time period ~~epoch~~ shows a slight increase in summer and a slight decrease in winter. The third time period ~~epoch~~ also shows a strong decrease in summer and an increase in winter precipitation. In the Martelltal, on the other hand, winter precipitation decreases ~~significantly~~ and summer precipitation increases~~ significantly, especially in the second epoch, although epochs of different lengths are analysed~~.

Formatiert: Schriftfarbe: Automatisch

Formatiert: Schriftfarbe: Automatisch

Formatiert: Schriftfarbe: Automatisch

Formatiert: Schriftfarbe: Automatisch

Formatiert: Schriftfarbe: Automatisch

Formatiert: Schriftfarbe: Automatisch

Formatiert: Schriftfarbe: Automatisch

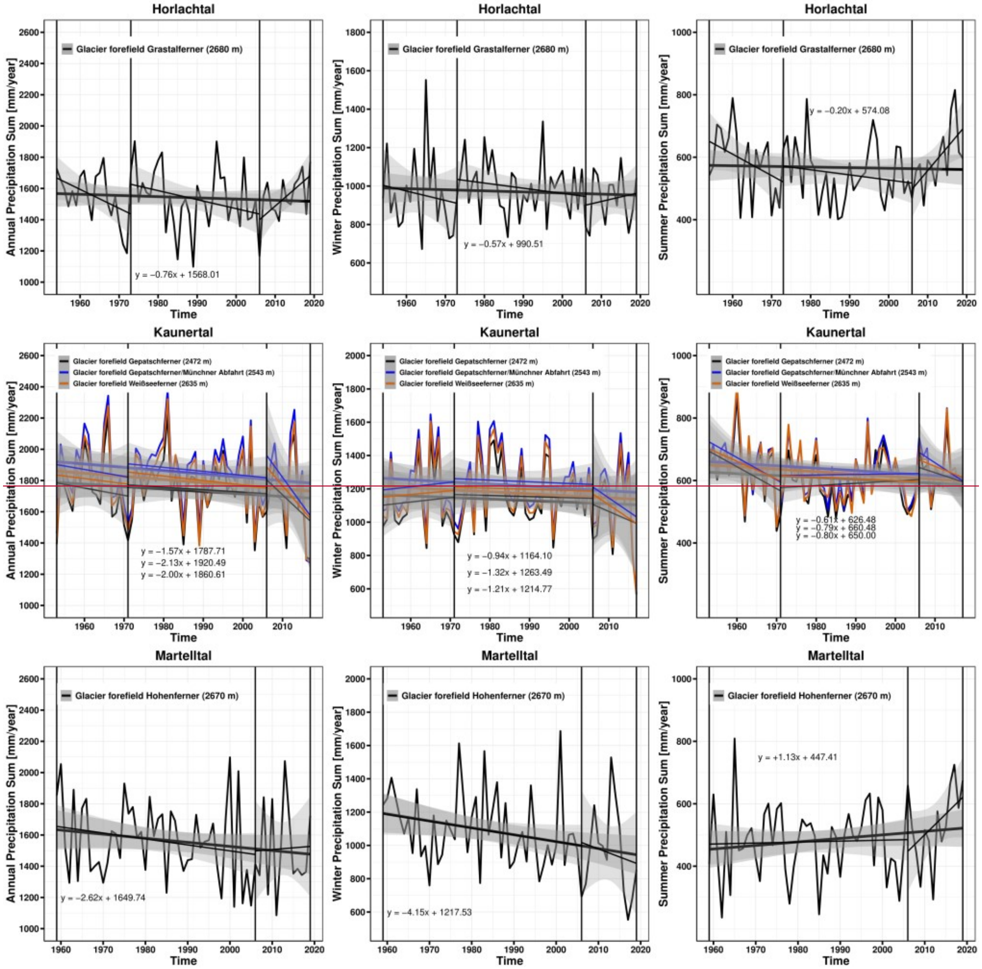
Horlachtal
Glacier forefield Grastalferner (2680 m)
Annual Precipitation Sum [mm/year]
Winter Precipitation Sum [mm/year]
Summer Precipitation Sum [mm/year]
y = −0.76x + 1568.01
y = −0.57x + 990.51
y = −0.20x + 574.08
Kaunertal
Glacier forefield Gepatschferner (2472 m)
Glacier forefield Gepatschferner/Münchner Abfahrt (2543 m)
Glacier forefield Weißseeferner (2635 m)
y = −1.57x + 1787.71
y = −2.13x + 1920.49
y = −2.00x + 1860.61
y = −0.94x + 1164.10
y = −1.32x + 1263.49
y = −1.21x + 1214.77
y = −0.61x + 626.48
y = −0.79x + 660.48
y = −0.80x + 650.00
Martelltal
Glacier forefield Hohenferner (2670 m)
y = −2.62x + 1649.74
y = −4.15x + 1217.53
y = +1.13x + 447.41
Time
1960
1970
1980
1990
2000
2010
2020
1000
1200
1400
1600
1800
2000
2200
2400
2600
600
800
400

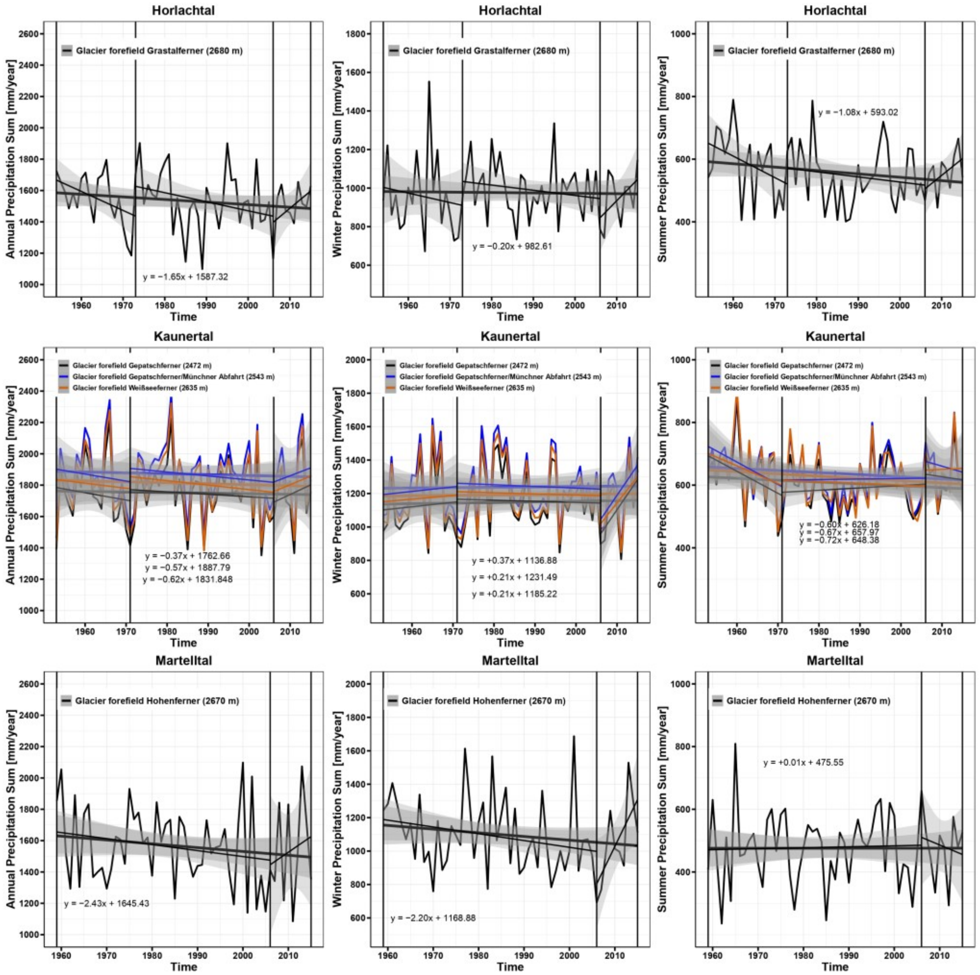

Figure 10: Mean annual, mean summer and mean winter precipitation of the respective glacier foreland~~field~~s.

In the following, the changes of different precipitation classes (as well as with a different temporal resolution) between the individual time periods ~~epochs~~ are analysed. The calculated changes are based on Appendix B and C. In these tables, the number of all precipitation events of the corresponding time periods ~~epochs~~ is shown and divided into corresponding precipitation classes. Using the number of years per time period~~epoch~~, this results in an mean annual number of events per class. The calculated changes result from the comparison of the mean occurrence of the precipitation classes of the previous time period~~epoch~~. Both precipitation events with a resolution of one hour (Figure 11/Appendix B) and daily precipitation totals (Figure 12/Appendix C) were analysed. The highest temporal resolution (1 hour) shows that the classes >0 to 4 and 4 to 8 are subject to the highest variations (Figure 11)~~; for example, precipitation events of the class >0 to 4 occur 7.63 times less in the glacier forefield of the Grastalferner in the second epoch compared to the first~~. In general, it can be seen that the higher precipitation classes tend to decrease, albeit very slightly, but there are still changes with both an increase and a decrease in the different precipitation classes. The daily precipitation totals also show a high variation, with both a decrease and an increase over the different time periods ~~epochs~~ (Figure 12). In general, there are also very slight changes. Nevertheless, the decrease in the higher three classes predominates when comparing the third with the second time period~~epoch~~.

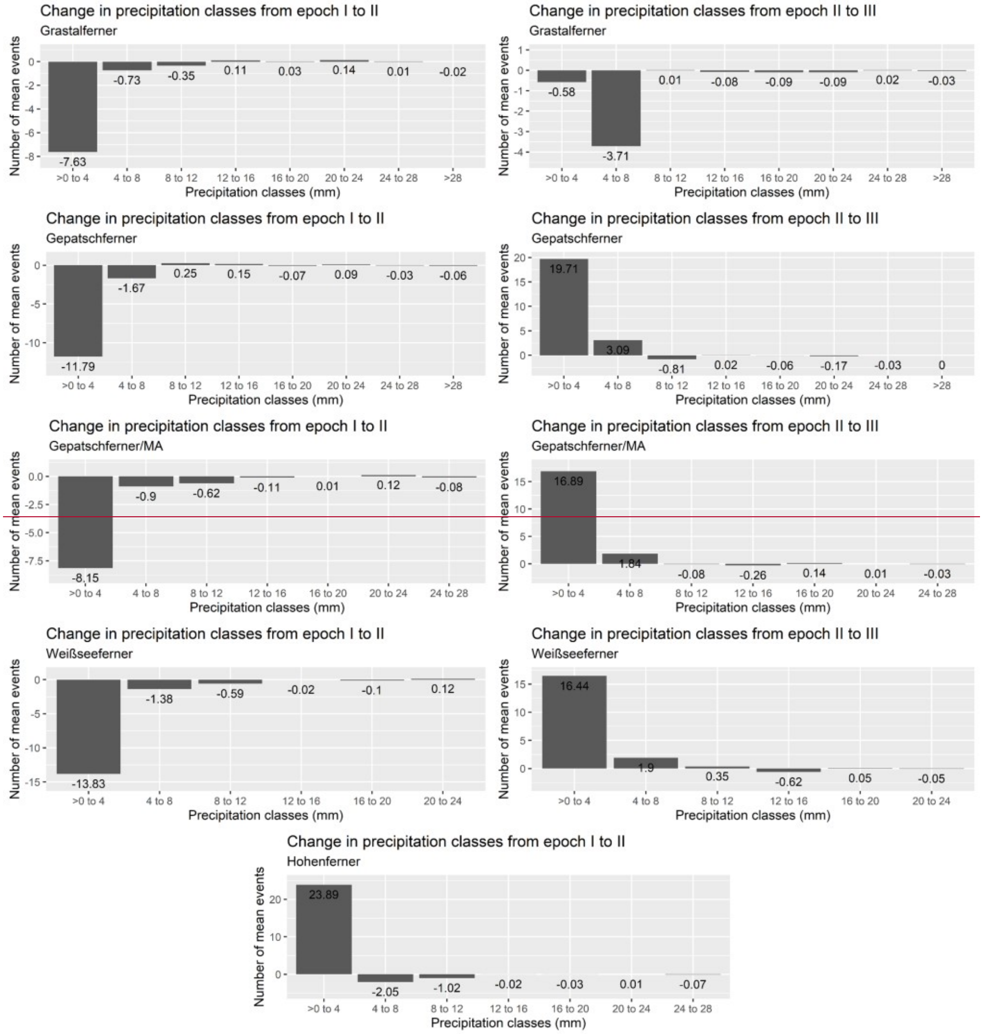

Change in precipitation classes from epoch I to II
Grastalferner
Number of mean events
0
-2
-4
-6
-8
-7.63
-0.73
-0.35
0.11
0.03
0.14
0.01
-0.02
>0 to 4
4 to 8
8 to 12
12 to 16
16 to 20
20 to 24
24 to 28
>28
Precipitation classes (mm)
Change in precipitation classes from epoch II to III
Grastalferner
Number of mean events
1
0
-1
-2
-3
-4
-0.58
-3.71
0.01
-0.08
-0.09
-0.09
0.02
-0.03
>0 to 4
4 to 8
8 to 12
12 to 16
16 to 20
20 to 24
24 to 28
>28
Precipitation classes (mm)
Change in precipitation classes from epoch I to II
Gepatschferner
Number of mean events
0
-5
-10
-11.79
-1.67
0.25
0.15
-0.07
0.09
-0.03
-0.06
>0 to 4
4 to 8
8 to 12
12 to 16
16 to 20
20 to 24
24 to 28
>28
Precipitation classes (mm)
Change in precipitation classes from epoch II to III
Gepatschferner
Number of mean events
20
15
10
5
0
19.71
3.09
-0.81
0.02
-0.06
-0.17
-0.03
0
>0 to 4
4 to 8
8 to 12
12 to 16
16 to 20
20 to 24
24 to 28
>28
Precipitation classes (mm)
Change in precipitation classes from epoch I to II
Gepatschferner/MA
Number of mean events
0.0
-2.5
-5.0
-7.5
-8.15
-0.9
-0.62
-0.11
0.01
0.12
-0.08
>0 to 4
4 to 8
8 to 12
12 to 16
16 to 20
20 to 24
24 to 28
Precipitation classes (mm)
Change in precipitation classes from epoch II to III
Gepatschferner/MA
Number of mean events
15
10
5
0
16.89
1.84
-0.08
-0.26
0.14
0.01
-0.03
>0 to 4
4 to 8
8 to 12
12 to 16
16 to 20
20 to 24
24 to 28
Precipitation classes (mm)
Change in precipitation classes from epoch I to II
Weißseeferner
Number of mean events
0
-5
-10
-15
-13.83
-1.38
-0.59
-0.02
-0.1
0.12
>0 to 4
4 to 8
8 to 12
12 to 16
16 to 20
20 to 24
Precipitation classes (mm)
Change in precipitation classes from epoch II to III
Weißseeferner
Number of mean events
15
10
5
0
16.44
1.9
0.35
-0.62
0.05
-0.05
>0 to 4
4 to 8
8 to 12
12 to 16
16 to 20
20 to 24
Precipitation classes (mm)
Change in precipitation classes from epoch I to II
Hohenferner
Number of mean events
20
10
0
23.89
-2.05
-1.02
-0.02
-0.03
0.01
-0.07
>0 to 4
4 to 8
8 to 12
12 to 16
16 to 20
20 to 24
24 to 28
Precipitation classes (mm)

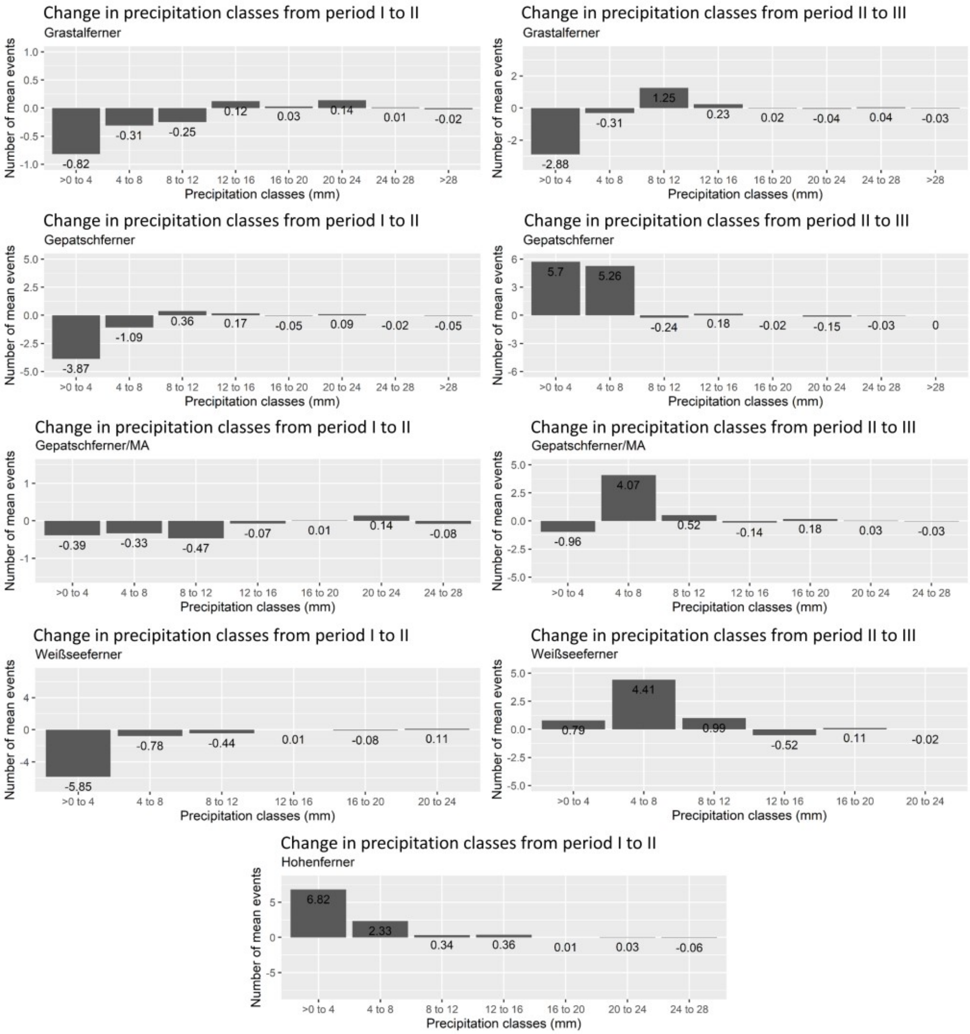

Figure 11: Change in precipitation classes between the different time periods ~~epochs~~ with a one-hour resolution (extreme precipitation events).

Formatiert: Schriftart: 9 Pt., Fett

504

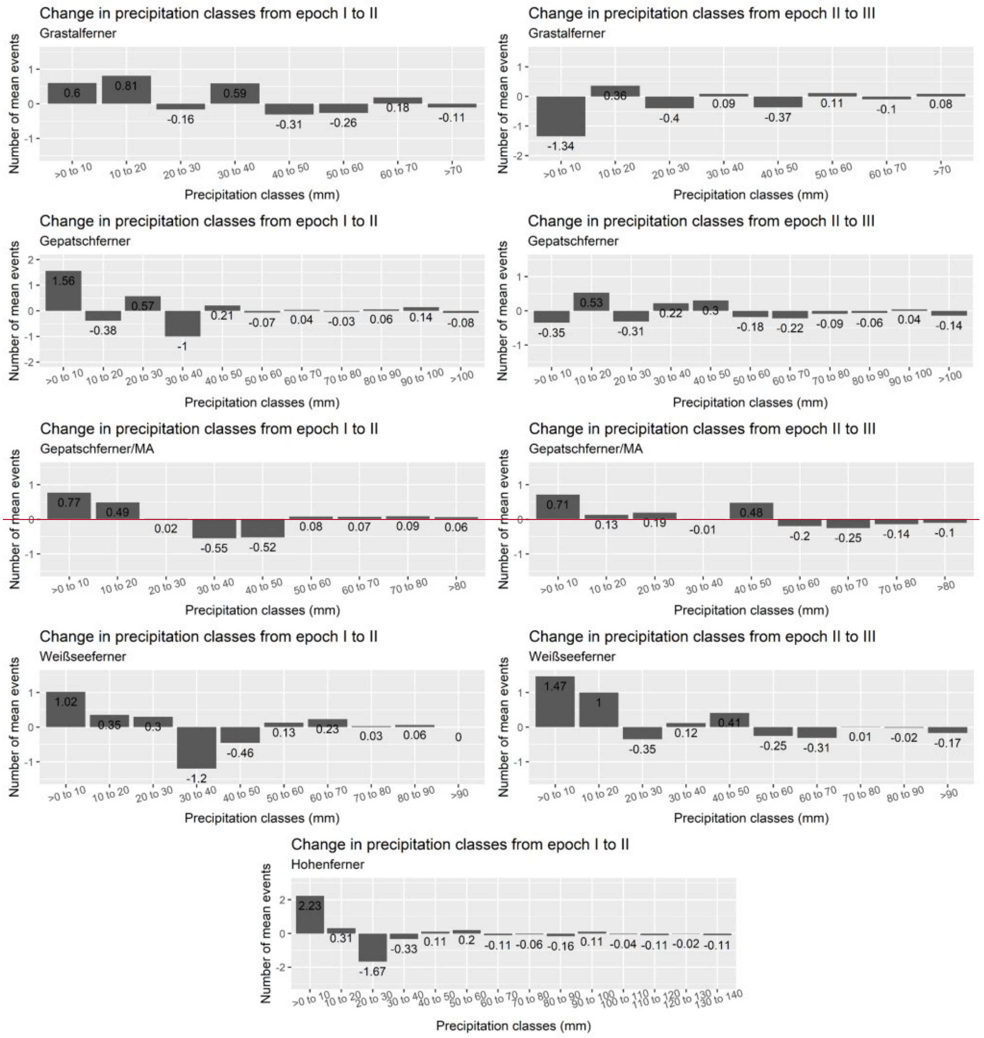
Change in precipitation classes from epoch I to II
Grastalferner
0.6
0.81
-0.16
0.59
-0.31
-0.26
0.18
-0.11
>0 to 10
10 to 20
20 to 30
30 to 40
40 to 50
50 to 60
60 to 70
>70
Change in precipitation classes from epoch II to III
Grastalferner
-1.34
0.36
-0.4
0.09
-0.37
0.11
-0.1
0.08
>0 to 10
10 to 20
20 to 30
30 to 40
40 to 50
50 to 60
60 to 70
>70
Change in precipitation classes from epoch I to II
Gepatschferner
1.56
-0.38
0.57
-1
0.21
-0.07
0.04
-0.03
0.06
0.14
-0.08
>0 to 10
10 to 20
20 to 30
30 to 40
40 to 50
50 to 60
60 to 70
70 to 80
80 to 90
90 to 100
>100
Change in precipitation classes from epoch II to III
Gepatschferner
-0.35
0.53
-0.31
0.22
0.3
-0.18
-0.22
-0.09
-0.06
0.04
-0.14
>0 to 10
10 to 20
20 to 30
30 to 40
40 to 50
50 to 60
60 to 70
70 to 80
80 to 90
90 to 100
>100
Change in precipitation classes from epoch I to II
Gepatschferner/MA
0.77
0.49
0.02
-0.55
-0.52
0.08
0.07
0.09
0.06
>0 to 10
10 to 20
20 to 30
30 to 40
40 to 50
50 to 60
60 to 70
70 to 80
>80
Change in precipitation classes from epoch II to III
Gepatschferner/MA
0.71
0.13
0.19
-0.01
0.48
-0.2
-0.25
-0.14
-0.1
>0 to 10
10 to 20
20 to 30
30 to 40
40 to 50
50 to 60
60 to 70
70 to 80
>80
Change in precipitation classes from epoch I to II
Weißseeferner
1.02
0.35
0.3
-1.2
-0.46
0.13
0.23
0.03
0.06
0
>0 to 10
10 to 20
20 to 30
30 to 40
40 to 50
50 to 60
60 to 70
70 to 80
80 to 90
>90
Change in precipitation classes from epoch II to III
Weißseeferner
1.47
1
-0.35
0.12
0.41
-0.25
-0.31
0.01
-0.02
-0.17
>0 to 10
10 to 20
20 to 30
30 to 40
40 to 50
50 to 60
60 to 70
70 to 80
80 to 90
>90
Change in precipitation classes from epoch I to II
Hohenferner
2.23
0.31
-1.67
-0.33
0.11
0.2
-0.11
-0.06
-0.16
0.11
-0.04
-0.11
-0.02
-0.11
>0 to 10
10 to 20
20 to 30
30 to 40
40 to 50
50 to 60
60 to 70
70 to 80
80 to 90
90 to 100
100 to 110
110 to 120
120 to 130
130 to 140
Number of mean events
Precipitation classes (mm)

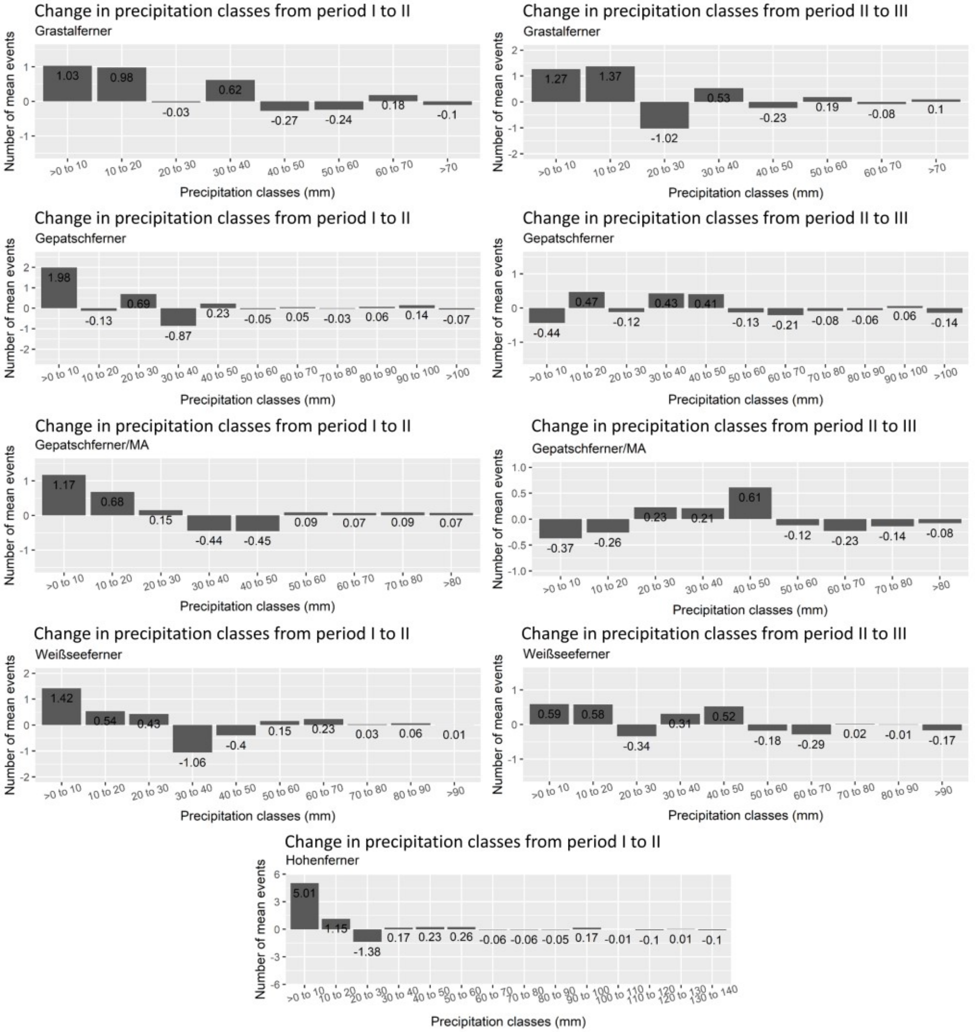

Figure 12: Change in precipitation classes between the different ~~epochs~~ time periods with a 24-hour resolution (daily precipitation totals).

The analysis of the mean annual rainfall and snowfall events shows that there is a consistent increase in rainfall and at the same time a consistent decrease in snowfall~~ (except for the Weißseeferner glacier forefield)~~ (Figure 13).

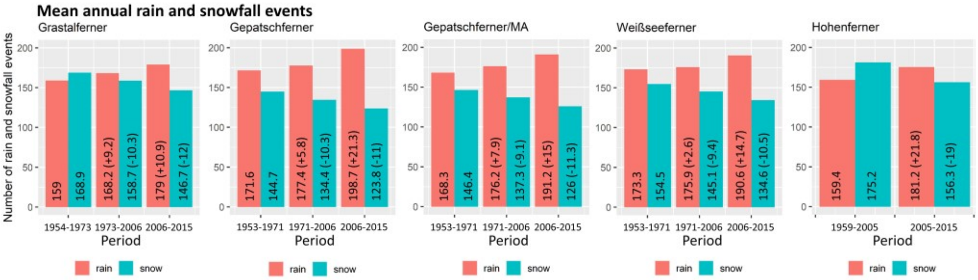

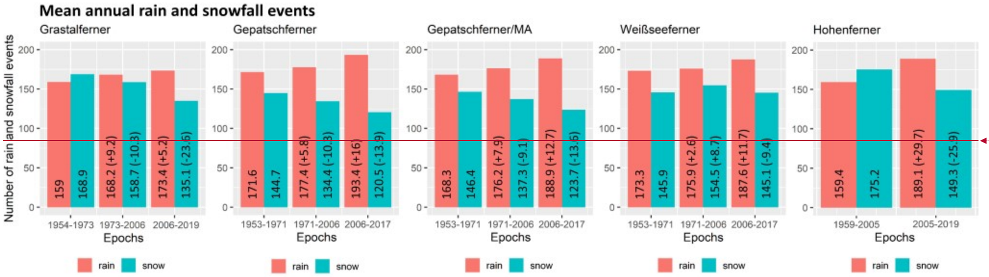

Figure 13: Mean annual rain and snowfall events with the corresponding changes between ~~epochs~~time periods.

5 Discussion

5.1 Assessment of the sediment contributing area ~~SCA~~ approach

Using the relationship between accumulated sediment yield ~~SY~~ from DoDs and sediment contributing area~~SCA~~/~~CA~~catchment area (log-log model) of different ~~AOIs~~ sites and different time periods~~epochs~~, we show a long-term monitoring of several geomorphologically active sections of LIA lateral moraines. This is a clear difference to previous studies that used the space-for-time-substitution (SFTS) approach in proglacial areas, in which studies used recent morphometrical or morphodynamical differences between sites located along a gradient of deglaciation age to infer long-term changes in morphodynamics (Ballantyne and Benn, 1994; Curry, 1999; Curry et al., 2006). Means that long-term studies with quantitative data are rare (Schiefer and Gilbert, 2007; Betz et al., 2019; Altmann et al., 2020; Betz-Nutz, 2021; Betz-Nutz et al., 2023). The approach shown here provides reliable results and requires only a few input data (Neugirg et al., 2015a; 2015b; 2016; Dusik, 2019; Dusik et al., 2019). The results mainly show a decrease in sediment yield ~~SY~~ as well as a decrease in the slope of the regression

Formatiert: Schriftfarbe: Automatisch

Formatiert: Schriftfarbe: Automatisch

Formatiert: Schriftfarbe: Rot

Formatiert: Vom nächsten Absatz trennen lines (suggesting less sediment yield ~~SY~~ per square metre) over the different time periods~~epochs~~, indicating a decrease in geomorphic activity on these ~~AOIs~~sites. In some ~~AOIs~~sites, we observe contrasting changes: There is an increase in sediment yield ~~SY~~ and an increase in the slope of the regression line at HG1 and almost no change in sediment yield ~~SY~~ on the Y-axis but an increase in the slope of the regression line at MH1, which can be described as an increase (HG1) and a constant geomorphic activity (MH1). Moreover, in the earlier time periods~~epochs~~, a clearly higher variability of sediment yield ~~SY~~ (Slope of the regression line clearly higher 1) was observed on the respective ~~AOIs~~sites, which is no longer reached in the later ones. Thus, it is possible to describe two different types of change in sediment yield ~~SY~~ (size of sediment yield ~~SY~~ between time periods ~~epochs~~ and variability of sediment yield ~~SY~~ within an time period~~epoch~~, which can also be compared with the other time periods~~epochs~~). Slopes of the regression line below 1 could occur when spots appear within the area that are no longer active, which could be an indication of stabilisation, which occurs mainly in the second and third time period~~epoch~~.

The p-values of the coefficients are mostly below the alpha level of 0.05, so it is assumed that the relationships between sediment contributing area ~~SCA~~ and sediment yield ~~SY~~ are statistically significant in almost all cases (~92%) (Figure 6). To determine the proportion of the variance of the dependent variable that can be explained by the independent variable, the R-squares (R^2 or the coefficient of determination) of all regression lines were analysed (Figure 6, Appendix A). The relationship between sediment contributing area ~~SCA~~ and sediment yield ~~SY~~ shows varying correlations within the ~~AOI~~ site and the time periods~~epochs~~. The median R^2 values range from 0.59 to 0.91 in the first time period~~epoch~~, from 0.37 to 0.93 in the second time period ~~epoch~~ and from 0.3 to 0.94 in the third time period ~~epoch~~ (Figure 6, Appendix A). The number of channels modelled differed between the time periods ~~epochs~~ on the same ~~AOIs~~ sites due to the different quality of the DEMs and the slightly different size of these. As in Heckmann and Vericat (2018), the accumulation of DoD values resulted in very small positive values at some ~~AOIs~~sites. Such errors are due to the quality of the DoD, different bulk densities of eroded vs. deposited materials, and the inability of the flow routing algorithm to fully reproduce sediment transfer in reality especially when flow directions changed within one time period~~epoch~~. Where positive accDoD values occurred, they were small and manually corrected to the zero.

Nevertheless, the D8 algorithm simplifies complex sediment transport processes such as fluvial activity, landslides and debris flows, which have different frequencies, magnitudes and forms of erosion and accumulation. As the individual time periods ~~epochs~~ cover several years, no reference can be made in this study to individual processes that can be attributed to extreme precipitation events or to seasonal differences. Therefore, we compare different time periods ~~epochs~~ based on mean annual sediment yield ~~SY~~, which includes all geomorphological processes. Accordingly, the aim was not to model individual erosion processes but to compute sediment yield ~~SY~~ of each cell. The individual ~~AOIs~~ sites have a slightly different area within the different time periods~~epochs~~, which is mainly due to headcut retreat (Heckmann and Vericat, 2018; Betz-Nutz et al., 2023). The lateral boundaries also changed slightly due to the quality of the DEMs and geomorphological slope processes, while the lower boundary did not change.

By processing historical aerial photographs into DEMs (by SfM-MVS), the temporal aspect of sediment contributing area ~~SCA~~ studies could be quickly and cost-effectively extended to several decades (up to the 1950s), which previously spanned only a few months or several years (Neugirg et al., 2015a; 2015b; 2016; Dusik, 2019; Dusik et al., 2019). However, as Schiefer and Gilbert (2007) have already shown, the shorter the time intervals and the lower the quality of the aerial images, the more difficult it becomes to detect surface changes, so in the process of this study several series of aerial images had to be sorted out that were actually available due to a poor data quality. Furthermore, it should be noted that the accuracy and precision of the historical DEMs strongly depends on the respective generation, e.g. whether they were generated with or without a calibration certificate (as was the case, for example, with the 1959 aerial photo series in the Horlachtal/glacier foreland ~~forefield~~ Hohenferner), which ultimately influences the sediment contributing area ~~SCA~~ results and the calculated erosion rates (Stark et al., 2022).

5.2 Geomorphic activity

The geomorphic activity is directly related to the characteristics of the ~~AOIs~~sites. The ~~AOIs~~ sites with the highest mean annual sediment output (>100m^3/a) (such as KG1, KG2, KG4, KG5, MH2, KM2, KW2) show strong gully formation and are overall characterised by larger areas, longer max. slope lengths and higher mean and max. slope gradients (Table 1). In contrast, the ~~AOIs~~ sites with lower mean annual sediment output (<100m^3/a) (such as KW1, KG3, HG1, KM1, MH1) show less gully incision. These ~~AOIs~~ sites tend to be characterised by smaller areas, smaller max. slope lengths and smaller mean slope and max. slope gradients (Table 1). The strong influence of slope length and slope gradient on morphodynamics is also shown by previous studies (Ballantyne and Benn, 1994; Curry, 1999; Curry et al., 2006; Betz-Nutz et al., 2023). KG3 also appears to be somehow stabilized by bedrock in the lower part of the slope, which could mitigate the erosion of this ~~AOI~~site, as also shown by Jäger and Winkler (2012). ~~.~~Elevation and aspect, however, do not seem to have an influence on geomorphic activity, which is also shown in the study by Curry et al. (2006). Since only bare and sparsely vegetated areas were investigated, no findings on the influence of vegetation on morphodynamics can be made in this study. Solifluction processes could also not be observed, probably due to the composition of the moraine material. Presumably, the morphodynamics are still so high that the vegetation does not yet have the opportunity to develop accordingly. In general, we assume that debris flows are the most common process, as described for example by Ballantyne (2002a) and Curry et al. (2006). Thus, material stored in the gullies is transported downslope by debris flows mainly rain or snow events in the spring or heavy rainfall events during rainstorms in the summer months (Ballantyne and Benn, 1994; Ballantyne, 2002b; Curry et al., 2006; Dusik et al., 2019).

However, the high mean annual sediment yield and corresponding erosion rate in the first (3471 m^3/a, 465 mm/a) and second (2922 m^3/a, 245 mm/a) time periods ~~epochs~~ of ~~AOI~~ site KG1 (Figure 7) can probably also be attributed to individual landslides and deep-seated slope failures in some cases linked with melting dead ice bodies, as these processes are more likely to occur after deglaciation, and are characterised by high magnitude and low frequency, which has also been shown by Blair (1994), Hugenholtz et al. (2008) and Cody et al. (2020). On the less incised slopes (e.g. MH1), small-scale processes such as fluvial erosion or snow drifts probably occur (Betz-Nutz, 2021), which ultimately show no clear trend in the increase or decrease of morphodynamics, but can be described as a constant geomorphic activity. In Betz-Nutz et al. (2023) and in this study, six similar lateral moraine sections (although other exactly defined ~~AOIs~~sites) were investigated. The test sites KG1, KG2, KW1, KW2 and MH1 (in Betz-Nutz et al. (2023): GPF1, GPF2, WSF1, WSF2 and HF1) showed similar erosion rates and the same log-term trends. In the case of ~~AOI~~ site MH2, different trends were determined (stagnation in Betz-Nutz et al. (2023) and a decrease in this study), which can be attributed to the differently defined ~~AOI~~ site and the slightly different study period.

In the sense of a process-response system, it is noticeable that the first-mentioned group of ~~AOIs~~ sites with the higher erosion rates (except KG1) had considerable influence from melting dead ice in the lower slope area at least until 2006 (KG2, KM2, KW2, MH2) or the glacier was still present at the bottom of the slope (KG4, KG5), which could be identified by the interpretation of the DoDs. Melting of the dead ice can lead to destabilisation of the slope, which can enhance erosion processes of the upper slope areas, as the support is no longer present, the sediment becomes saturated and there can be an increase in the slope gradient due to the subsidence of the lower part of the slope (Altmann et al., 2020; Betz-Nutz et al., 2023). However, the highest slope gradients are also present here, which also plays a major role. In addition, ~~AOI~~ site HG1, where erosion is increasing, shows an undercutting of the slope by the adjacent stream, which leads to a destabilization or lowering of the erosion base and a typical formation of a debris cone and alluvial fan with a successive reduction of the slope gradient is missing (Figure 14). It can be assumed that individual strong rainfall events in the second and third time periods ~~epochs~~ in combination with changing flow pathes due to the retreat of the Grastalferner acted here as an impulse and affected both the ~~AOI~~ site itself and the adjacent stream.

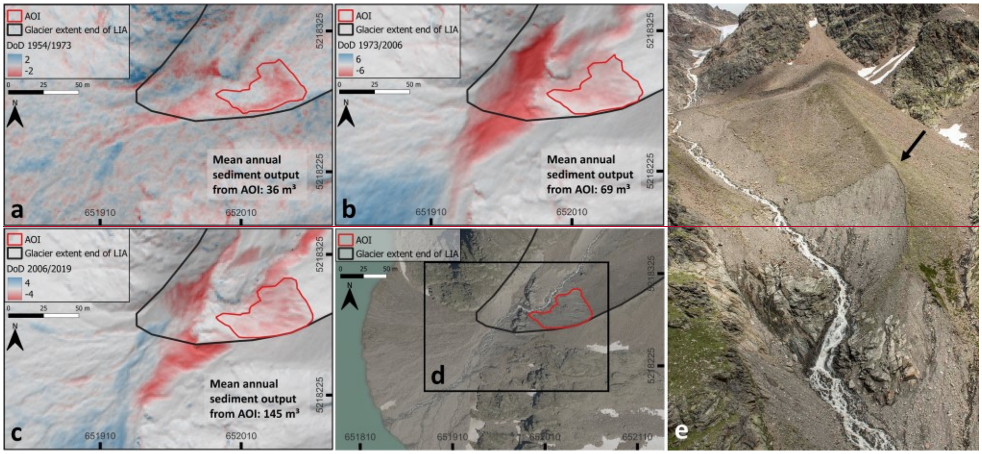

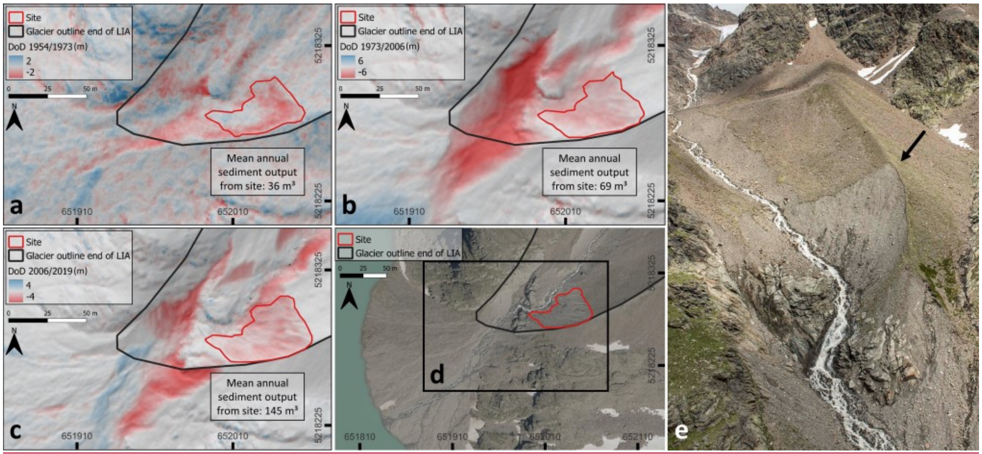

Figure 14: Overview of the DoDs of the corresponding ~~epochs~~ time periods of ~~AOI~~ site HG1: (a) DoD 1954-1973, (b) DoD 1973-2006, (c) DoD 2006-2019, (d) Orthofoto 2020 (provided by the Province of Tyrol) and (e) photo of the ~~AOI~~ site from 2019 by Anton Brandl.

5.3 Paraglacial landscape adjustment

5.3.1 The "Sediment activity concept"

The finding of mainly decreasing geomorphic activity of LIA lateral moraines in this study is largely consistent with previous model-based studies describing the paraglacial landscape adjustment with a decrease in geomorphic activity in proglacial areas over time, such as the theoretical model "paraglacial concept" of Church and Ryder (1972) or the "sediment exhaustion model" of Ballantyne (2002a, 2002b). The geomorphic activity of gully systems is given as a few decades to centuries (Ballantyne, 2002a; 2002b). Furthermore, it is stated that there is a high temporal and spatial variability in this development. The model provides an appropriate approximation (Ballantyne, 2002a; 2002b). Within the paraglacial adjustment process, different geomorphological processes result in different durations of occurrence. Furthermore, different land systems react at different rates and on different spatial scales. Thus, external perturbations can occur, leading to secondary peaks and time delays (Ballantyne, 2002a; 2002b). While ten out of twelve ~~AOIs~~ sites fit the model descriptions, two test plots show opposite morphodynamics, which can be described as a delay of the paraglacial adjustment process or that response systems can run counter to such an adaption.

To estimate the changing morphodynamics, we therefore propose the following simplified description of the landscape evolution using the "Sediment activity concept" based on the results of this study. Due to the study design, this concept is only valid on geomorphologically active areas (in this case the upper lateral moraine section) on LIA lateral moraines and until about 170 years after the end of LIA (Table 6, Figure 15). The concept distinguishes between an earlier and a later phase. The earlier phase (mainly 1950s to 1970s) is characterised by a wide range between areas with high and low variability of sediment yield ~~SY~~ within the area as well as high and low mean annual sediment yield (erosion rate/volume). In contrast, the later stadium (mainly 1970s to 2000s and 2000s to the end of the survey 2017/2019) shows a decrease in this range. Although the decrease of morphodynamics predominates, there are also increases in morphodynamics. The time of ice release was not integrated here, so that the time periods refer to the actual time. In addition, we give two examples in Figure 15. While example A shows high variability (polynomial behaviour) within the area and high sediment yield ~~SY~~ (erosion rates/sediment output), example B shows low variability (constant/linear behaviour) and low sediment yield ~~SY~~ (erosion rates/sediment output). Ultimately, the relationship between sediment yield ~~SY~~ and the size of the catchment has changed so that erosion within the area is more constant today.

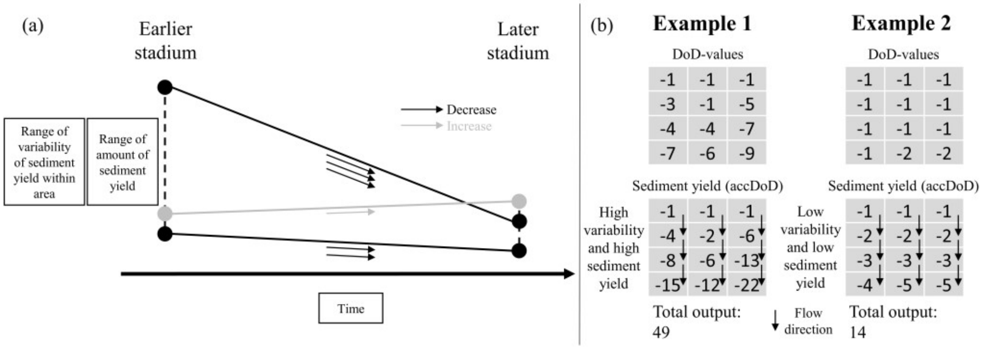

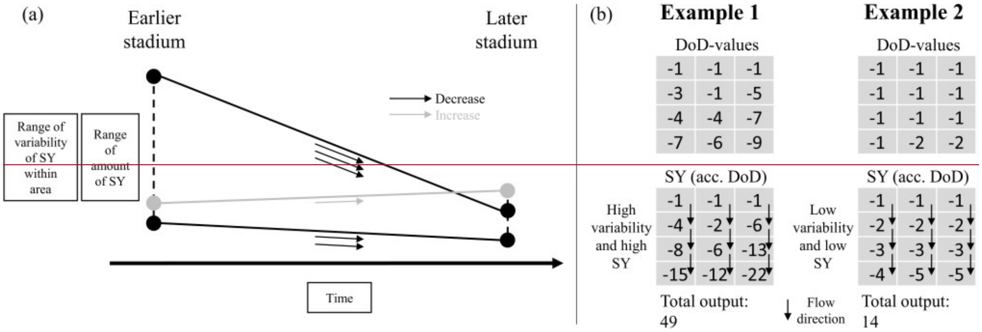

Figure 15: The "Sediment activity concept". Description and illustration of the change in sediment activity over time (a) and 2 corresponding examples (b).

Table 6: Tabular summary of the simplified conceptual model.

	Earlier stadium	Later stadium
Sediment yield ~~SY~~ within area	~~highly~~ Highly variable up to constant	~~in~~ In the range of constant
Amount of sediment yield~~SY~~	~~wide~~ Wide range	L~~l~~ower range
Over time	M~~m~~ostly decreasing	

Introducing the "Sediment activity concept" of this study, we present a different description of the paraglacial adjustment process which is based on the actual ~~SY~~sediment yield. However, the concept is only valid until about 170 years after the end of LIA and on the ~~AOIs~~ sites of this study. The "Sediment activity concept" presented here is also compatible with the results of other studies, as for example Betz-Nutz et al. (2023) mostly show a decrease in erosion rates over a similar time period, but also a remaining at similar levels and an increase. In addition, the studies by Church and Ryder (1972), Ballantyne and Benn (1996), Curry (1999), Ballantyne (2002a), Curry et al. (2006) and Schiefer and Gilbert (2007) show a decrease in geomorphic activity over time, which is also consistent with the model presented here. ~~Nevertheless~~Also, we assume that the concept can also prove its validity in further proglacial active areas and partly over an even longer period of time.

5.3.2 Erosion rates

~~The comparison of long-term erosion rates of gully systems in proglacial areas of different studies shows the high variability of this adjustment; as these studies were carried out with different methods, on different time scales and in different glacier forefields, comparing their results is difficult (Table 7).~~ The methodologies for determining long-term average erosion rates in proglacial areas~~-~~ are based on gully volume estimates (Ballantyne and Benn, 1994; Curry, 1999; Curry et al., 2006) and

Formatierte Tabelle

Formatiert: Schriftart: 9 Pt.

Formatiert: Schriftart: 9 Pt.

sediment volume calculations due to surface changes using DoDs, as shown by Betz-Nutz et al. (2023) and this study (Table 7). In glacier forelands ~~forefields~~ in western Norway, this amounts e.g. to minimum estimates of 50-100 mm/year (max. estimates of min. 200 mm/year) (Ballantyne and Benn, 1994) and a minimum of 5.5-169 mm/year (in different glacier forelands~~forefields~~) (Curry, 1999). A further study in the Swiss Alps shows erosion rates of min. 49-151 (in different glacier forelands~~forefields~~) (Curry et al., 2006). The work of Betz-Nutz et al. (2023) and this study show erosion rates over several decades and distinguish between different time periods~~epochs~~, which makes it possible to show differences between them. Both studies show that the mean erosion rates in the individual time periods ~~epochs~~ decrease (Table 7), although in individual cases there is also a constant and an increase in erosion rates over time. Although there has been a clear decrease in geomorphic activity, stabilisation of the ~~AOIs~~ sites is not yet apparent, which means that the paraglacial adjustment is still ongoing. Within this study, we observed that the ~~AOIs~~ sites still show a high geomorphic activity even after they have been deglaciated for 76-159 years. A stabilisation of the gully systems as shown by Curry (2006) cannot be observed. Other studies such as Lane et al. (2017), Dusik (2019), Altmann et al. (2020), Betz-Nutz et al. (2023) also show the still ongoing paraglacial adjustment processes. Comparing the long-term erosion rates of gully systems from the different studies ultimately shows high variability in the adjustment; as these studies were also conducted using different methods, on different time scales, and in different regions. Differences are probably mainly due to the different local conditions, such as the geomorphological settings, e.g. the different characteristics of the lateral moraine sections, such as slope gradient, slope length, time of ice exposure, dead ice influence and the development of vegetation. Furthermore, the lateral moraines have different sedimentological characteristics related to their genetic origin. In addition, different meteorological conditions prevail in the different regions.

Table 7: Studies on long-term erosion rates (several decades) of gully systems on LIA lateral moraines in different glacier foreland~~field~~s.

Study	Erosion rate (mm/year)	Timescale (year)	Time since ice exposure (year)	Location of the study area
Ballantyne and Benn (1994)	Min. of 50-100, max. min. of 200	48	48	Norway, Fåbergstølsbreen
Curry (1999)	Min. of 5.5-8.8, 38-169 and 19-169	76, 53, 43	76, 53, 43	Norway, Fåbergstølsbreen, Lodalsbreen and Heillstugubreen
Curry et al. (2006)	Min. of 86-151 and 49-103	55, 79	55, 79	Switzerland, Glacier du Mont Miné and Feegletscher

Betz-Nutz (2021; 2023)	~~Epoch~~ Period I: 2-429, period~~epoch~~ II: 1-186, period~~epoch~~ III: 3-110	~~Epoch~~ Period I: Mainly ~1950s to ~1970s, ~~Epoch~~ period II: ~1970s to ~2000s and ~~Epoch~~ period III: ~2000s to 2018/2019	59-154	Austria (Tyrol), Germany (Bavaria) and Italy (South Tyrol), ten different glacier foreland~~field~~s
This study	~~Epoch~~ Period I: 19-465, period~~epoch~~ II (HT and KT): 13-245, ~~epoch~~period II (MT) and ~~epoch~~period III (HT and KT): 8-88	~~Epoch~~ Period I: 17-19 (in HT and KT) and 45/46 (in MT), period~~epoch~~ II: 33-36 (in HT and KT) and 14/15 (in MT) and ~~epoch~~ period III: 11-13 (in HT and KT)	76-159	Austria (Tyrol) and Italy (South Tyrol), five different glacier foreland~~field~~s

***HT = Horlachtal, KT = Kaunertal and MT = Martelltal.**

5.4 Meteorological drivers

The decrease of the mean annual number of ice days and the increase in the number of warm spells over the different time periods ~~epochs~~ and the associated potential increase in snowmelt on the slopes could also lead to an increase in morphodynamics, as these processes represent important preparatory steps for erosion processes in spring (Haas, 2008), such as increased saturation of the slope du to snow melt, loosening of the upper sediment layers or the delivery of material by snow slides or small wet avalanches that is then available for debris flows in the summer months (Dusik et al., 2019). Klein et al. (2016), for example, also show an increase in the frequency and intensity of snowmelt in the Swiss Alps. Mean annual precipitation decreases slightly across time periods~~epochs~~, but is not statistically significant (except for winter precipitation for the entire study period (1959 to 2019) and summer precipitation in the second time period ~~epoch~~ from 2005 to 2019 in the Martelltal). Other studies also show that the decrease in precipitation in the European Alps is low (Brugnara et al., 2012) and that there is no clear trend in precipitation (Hock et al., 2019) or that it is mainly subject to regional influences and decadal variations (Mankin and Diffenbaugh, 2015). Extreme precipitation events (1h resolution) and daily precipitation totals also show only minor changes. Differentiation of precipitation, on the other hand, shows a clear increase in rainfall and a decrease in snowfall, which is also shown by Serquet et al. (2011), Beniston et al. (2018) and Hock et al. (2019) who found that the rainfall on snow events in spring as preparatory factor for the erosion processes in the summer months increase. The simulated meteorological data generally show lower temperatures and larger precipitation amounts, when compared to three automatic weather stations operated by TIWAG (Tyrolean Hydropower AG, Innsbruck, Austria). These stations are located in the vicinity of our ~~AOIs~~sites. The simulated mean annual temperatures extracted at the location of the weather stations Horlachalm (1987-2015) (approx. 6.5 km linear distance to the ~~AOI~~ site in the Grastalferner glacier forfield) and Weißseeferner (2007-2015) (approx. 500 m linear distance to the ~~AOIs~~ sites in the Weißseeferner glacier forfield), covering the same time period indicate

Feldfunktion geändert

Feldfunktion geändert

Feldfunktion geändert

Feldfunktion geändert

Feldfunktion geändert

Feldfunktion geändert

Feldfunktion geändert

Feldfunktion geändert

Feldfunktion geändert

Feldfunktion geändert

Feldfunktion geändert

Feldfunktion geändert

Feldfunktion geändert

Feldfunktion geändert

Feldfunktion geändert

a difference of -1.05°C and of -0.87°C, respectively, after accounting for differences in elevation. However, at Gepatschalm (2010-2015) weather station (approx. 2.5 km linear distance to the ~~AOIs~~ sites in the Gepatschferner glacier forfield), the difference between the simulated and observed mean annual temperatures is 0.13°C, indicating that the magnitude of the discrepancies depends on the station data used for the comparison. The simulated precipitation, however, is generally larger with mean annual precipitation sums of 1531, 1655, and 1820 mm at the location of Horlachalm (1990-2015), Gepatchalm (2010-2015), and Weißseeferner (2007-2015), respectively, while the weather stations recorded values of 803, 1086, and 924 mm, indicating large discrepancies especially when compared to Horlachalm and Weißseeferner weather stations. The datasets from which the temperature and precipitation were extracted are both based on coarsely resolved data, which makes a comparison with measurement data in the field difficult, although the corresponding trends are well usable for this study. The large difference between simulated and recorded precipitation is mainly due to winter precipitation (Figure 11) when the weather stations are not always able to record total snowfall accurately; additionally, fog precipitation or precipitation in combination with stronger winds are not recorded correctly.

The weather and climate study periods are based on the predefined study time periods ~~epochs~~ given by the availability and quality of orthophotos, and not on the usual climate periods. This results in large differences in the length of the different time periods~~epochs~~, which must be taken into account.

There are several sources of uncertainty in the simulated data, amongst them the dynamic initial and boundary conditions, as the forcing data have their own sources of uncertainties. Furthermore, the choice of the reanalysis data used for forcing the model has an influence on the final results. Additionally, for such long simulations, an updated sea surface temperature (SST) is recommended. Since there are no SSTs available for the 20CRv3, we have generated SST fields from the skin temperature. Other sources of uncertainty are the static boundary conditions like the fixed land use categories and topography, as well as model simplifications and choices in the parameterization of the physics and dynamics. In our simulations, we have used spectral nudging in order to keep the model from large deviations from the forcing data. Short test runs indicate that the use of spectral nudging improves the simulated data, especially with respect to precipitation. However, the strength of nudging also has an influence on the final resuls. Since the purpose of this study is not to test how strongly to nudge, we have used the default values in WRF.

6 Conclusion

Using DoDs based on SfM photogrammetric and LiDAR data DEMs, we show with two different approaches, the long-term (1953-2019) change in the morphodynamics of several active gully systems on LIA lateral moraines in the Tyrolean and South Tyrolean Alps, Austria and Italy. First, the change in the range of variability of sediment yield ~~SY~~ within the area (using regression lines with accumulated sediment yield~~SY a~~ and sediment contributing area~~SCA~~/catchment area~~CA~~) and second, the change in the amount of sediment yield ~~SY~~ (calculation of erosion rates/volume of sediment output) between the different time periods ~~epochs~~ could be shown.

Finally, the first time period ~~epoch~~ shows a clearly higher range of variability of sediment yield ~~SY~~ within the ~~AOI~~ site than the later time periods~~epochs~~. This means that the spatial pattern of erosion has become more uniform within the areas. In addition, the total sediment yield, the mean annual sediment yield and the mean annual specific sediment yield (erosion rate) were calculated for each ~~AOI~~ site and time period ~~epoch~~ was calculated. Over the time periods~~epochs~~, there is a decreasing trend of geomorphological activity in 10 out of 12 sites ~~AOIs~~, while 2 sites ~~AOIs~~ show an opposite trend, where morphodynamics increase or remain at the same level. Overall, we confirm the general trend of decreasing morphodynamics over time (10 sites~~AOIs~~) of several previous studies, although we could also show that the geomorphic activity of one site ~~AOI~~ is on the same level and one is increasing. Finally, the results led to the proposal of a simplified conceptual model "The sediment activity concept", describing the paraglacial adjustment process by summarising the findings on the long-term morphodynamics of the upper parts (gully heads) of lateral moraines from this study.

Despite the general decline in morphodynamics, the sites ~~AOIs~~ show no stabilisation, leading us to the conclusion that the paraglacial landscape adjustment is still in progress (even on areas that have been ice-free for at least 159 years). It seems that the vegetation has not yet had the opportunity to develop due to the high morphodynamics. In general, debris flows are probably the most common processes, although it is difficult to separate the different processes, but very high sediment yield ~~SY~~ (mainly in the first time period~~epoch~~) also indicate landslides and slope failures. ~~AOI~~ Site morphodynamic is also related to the characteristics, i.e. sites ~~AOIs~~ that are larger, have longer max. lengths and higher mean slope gradients (as well as max. slope gradients) have clearly higher geomorphic activity and form more deeply incised gullies. In the sense of a process-response system, it can be stated that the melting of dead ice in the lower slope area, which in some cases lasts for decades, leads to high morphodynamics of the upper slope area. Furthermore, it is assumed that the lowering of the erosion base by adjacent streams leads to a delay of the paraglacial landscape adjustment, as the formation of an accumulation area is disrupted.

In addition to the system-internal influences on morphodynamics, we assume an additional influence of changing weather and climate factors on the corresponding erosion processes with an increase (mainly in the last, i.e. most recent time period ~~epoch~~ from the mid-2000s to 2017/2019), since the statistically significant warming of the last decades has led to a reduction of the mean annual ice days, to an increase in warm air inflows and, when distinguishing between rainfall and snowfall, to an increase in rainfall. We do not see any clear influence in the changing precipitation, although it can be assumed that the same precipitation intensities led to higher erosion in the first time period ~~epoch~~ than in the second or third. Nevertheless, the system-internal dynamics and the general paraglacial adaptation process seem to have the greatest impact on the changing morphodynamics. Future work should apply the approach used here to more areas and, if possible, with a higher temporal resolution to improve the process understanding of erosion on lateral moraines.

Appendix A

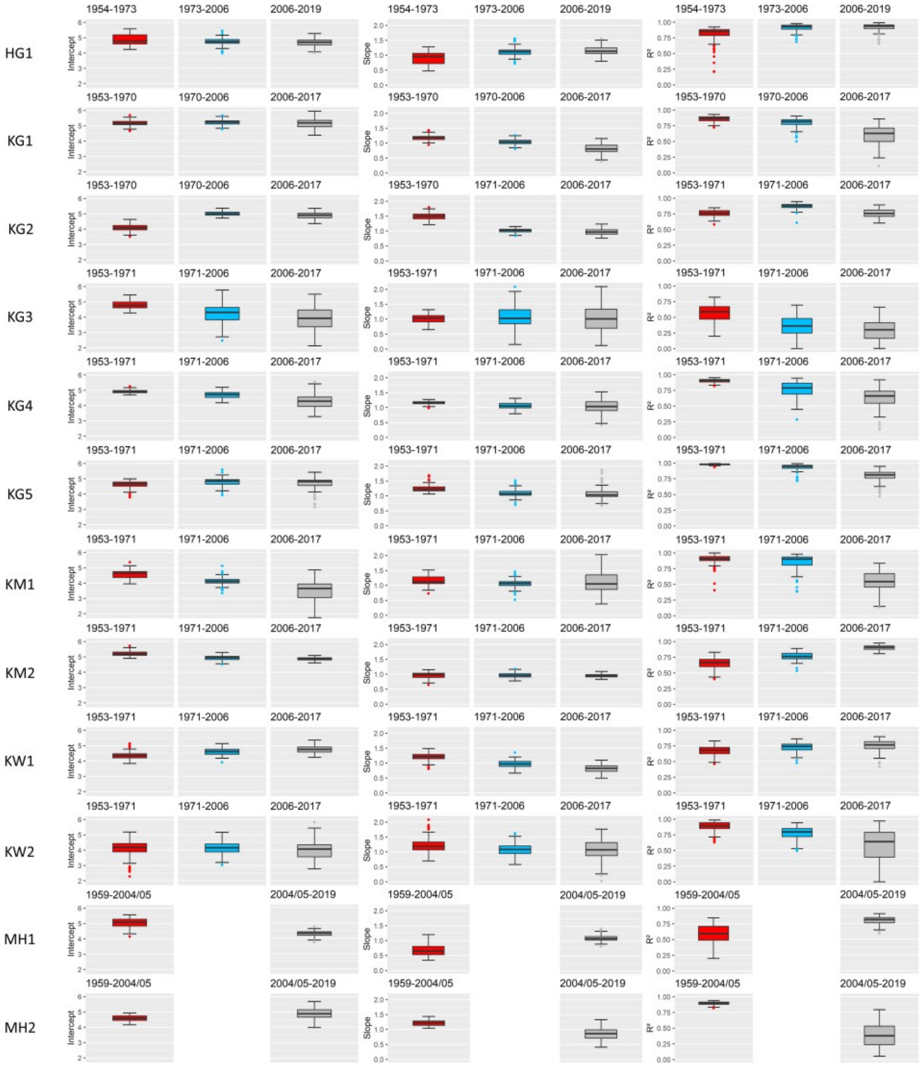

Boxplots of the model parameters Intercept, Slope and R² of all regression lines (see Figure 6).

Appendix B

Calculation of the individual extreme events by continuous ongoing 4 mm classes (with one-hour resolution).

	Precipitation interval (mm)	No. events/ total	No. events/year	No. events/total	No. events/year	No. events/total	No. events/year	Change from previous ~~epoch~~time period	
Grastalferner		1954-1973 (~~epoch~~ period I)		1973-2006 (period ~~epoch~~ II)		2006-~~2019~~ 2015 (period ~~epoch~~ III)		I to II	II to III
(Horlachtal)	>0 to 4	6084	3~~20~~04.2~~1~~0	10315	303.38~~312.58~~	3005~~4056~~	300.50~~312.00~~	-0.82~~-7.63~~	-2.88~~-0.58~~
	4 to 8	368	18.40~~19.37~~	615	18.09~~18.64~~	~~1~~184~~94~~	18.40~~14.92~~	-0.31~~-0.73~~	-0.31~~-3.71~~
	8 to 12	78	3.90~~4.11~~	124	3.65~~3.76~~	49	4.90~~3.77~~	-0.25~~-0.35~~	1.25~~0.01~~
	12 to 16	17	0.85~~0.89~~	33	0.97~~1.00~~	12	1.20~~0.92~~	0.12~~0.11~~	0.23~~-0.08~~
	16 to 20	7	0.35~~0.37~~	13	0.38~~0.39~~	4	0.40~~0.31~~	0.03	0.02~~-0.09~~
	20 to 24	2	0.10~~0.11~~	8	0.24	2	0.20~~0.15~~	0.14	-0.04~~-0.09~~
	24 to 28	1	0.05	2	0.06	1	0.10~~0.08~~	0.01	0.04~~2~~
	>28	1	0.05	1	0.03	0	0.00	-0.02	-0.03
Gepatschferner		1953-1971 (period ~~epoch~~ I)		1971-2006 (period ~~epoch~~ II)		2006-~~2017~~ 2015 (period ~~epoch~~ III)		I to II	II to III
(Kaunertal)	>0 to 4	5498	289.37~~305.44~~	10278	285.50~~293.66~~	2912~~3447~~	291.20~~313.36~~	-3.87~~-11.79~~	5.70~~19.71~~
	4 to 8	390	20.53~~21.67~~	700	19.44~~20.00~~	247~~254~~	24.70~~23.09~~	-1.09~~-1.67~~	5.26~~3.09~~
	8 to 12	87	4.58~~4.83~~	178	4.94~~5.09~~	47	4.70~~4.27~~	0.36~~0.25~~	-0.24~~-0.81~~
	12 to 16	20	1.05~~1.11~~	44	1.22~~1.26~~	14	1.40~~1.27~~	0.17~~0.15~~	0.18~~0.02~~
	16 to 20	9	0.47~~0.50~~	15	0.42~~0.43~~	4	0.40~~0.36~~	-0.05~~-0.07~~	-0.02~~-0.06~~
	20 to 24	3	0.16~~0.17~~	9	0.25~~0.26~~	1	0.10~~0.09~~	0.09	-0.15~~-0.17~~
	24 to 28	1	0.05~~0.06~~	1	0.03	0	0.00	-0.02~~-0.03~~	-0.03
	>28	1	0.05~~0.06~~	0	0.00	0	0.00	-0.05~~-0.06~~	0.00
Gepatschferner/		1953-1971 (period ~~epoch~~ I)		1971-2006 (period ~~epoch~~ II)		2006-~~2017~~ 2015 (period ~~epoch~~ III)		I to II	II to III
Müchner/	>0 to 4	5452	286.95~~302.89~~	10316	286.56~~294.74~~	2856~~3428~~	285.60~~311.64~~	-0.39~~-8.15~~	-0.96~~16.89~~
Abfahrt	4 to 8	402	21.16~~22.33~~	750	20.83~~21.43~~	249~~256~~	24.90~~23.27~~	-0.33~~-0.90~~	4.07~~1.84~~
(Kaunertal)	8 to 12	96	5.05~~5.33~~	165	4.58~~4.71~~	51	5.10~~4.64~~	-0.47~~-0.62~~	0.52~~-0.08~~
	12 to 16	23	1.21~~1.28~~	41	1.14~~1.17~~	10	1.00~~0.91~~	-0.07~~-0.11~~	-0.14~~-0.26~~
	16 to 20	4	0.21~~0.22~~	8	0.22~~0.23~~	4	0.40~~0.36~~	0.01	0.18~~0.14~~
	20 to 24	1	0.03~~0.06~~	6	0.17	2	0.20~~0.18~~	0.14~~0.12~~	0.03~~0.01~~
	24 to 28	2	0.11	1	0.03	0	0.00	-0.08	-0.03
Weißseeferner		1953-1971 (period ~~epoch~~ I)		1971-2006 (period ~~epoch~~ II)		2006-~~2017~~ 2015 (period ~~epoch~~ III)		I to II	II to III
(Kaunertal)	>0 to 4	5690	299.74~~316.11~~	10580	293.89~~302.29~~	2931~~3506~~	293.10~~318.73~~	-5.85~~-13.83~~	0.79~~16.44~~
	4 to 8	408	21.47~~22.67~~	745	20.69~~21.29~~	251~~255~~	25.10~~23.18~~	-0.78~~-1.38~~	4.41~~1.90~~
	8 to 12	96	5.05~~5.33~~	166	4.61~~4.74~~	56	5.60~~5.09~~	-0.44~~-0.59~~	0.99~~0.35~~

Formatierte Tabelle
Formatiert
Formatiert
Formatiert
Formatiert
Formatiert
Formatiert
Formatiert
Formatiert
Formatiert
Formatiert
Formatiert
Formatiert
Formatiert
Formatiert
Formatiert
Formatiert
Formatiert
Formatiert
Formatiert
Formatiert
Formatiert
Formatiert
Formatiert
Formatiert
Formatiert
Formatiert
Formatiert
Formatiert
Formatiert
Formatiert
Formatiert
Formatiert
Formatiert
Formatiert
Formatiert
Formatiert
Formatiert
Formatiert
Formatiert
Formatiert
Formatiert
Formatiert
Formatiert
Formatiert
Formatiert

	12 to 16	23	1.21~~1.28~~	44	1.22~~1.26~~	7	0.70~~0.64~~	0.01~~-0.02~~	-0.52~~-0.62~~
	16 to 20	9	0.47~~0.50~~	14	0.39~~0.40~~	5	0.50~~0.45~~	-0.08~~-0.10~~	0.11~~0.05~~
	20 to 24	2	0.11	8	0.22~~0.23~~	2	0.20~~0.18~~	0.11~~0.12~~	-0.02~~-0.05~~
Hohenferner		1959-2005 (period ~~epoch~~ I)				2005-~~2019~~ 2015 (period ~~epoch~~ II)		I to II	
(Martelltal)	>0 to 4	14531	302.73~~315.89~~			3405~~4757~~	309.55~~339.79~~	6.82~~23.89~~	
	4 to 8	883	18.40~~19.20~~			228~~240~~	20.73~~17.14~~	2.33~~-2.05~~	
	8 to 12	241	5.02~~5.24~~			59	5.36~~4.21~~	0.34~~-1.02~~	
	12 to 16	57	1.19~~1.24~~			17	1.55~~1.21~~	0.36~~-0.02~~	
	16 to 20	8	0.17			2	0.18~~0.14~~	0.01~~-0.03~~	
	20 to 24	3	0.06~~0.07~~			1	0.09~~0.07~~	0.03~~0.01~~	
	24 to 28	3	0.06~~0.07~~			0	0.00	-0.06~~-0.07~~	

Appendix C

Calculation of the daily precipitation totals by continuous ongoing 4 mm classes of the different ~~epochs~~ time periods (24-hour resolution).

Glacier foreland~~field~~	Precipitation interval (mm)	No. events/ total	No. events/ year	No. events/ total	No. events/ year	No. events/ total	No. events/year	Change from previous ~~epoch~~period	
Grastalferner		1954-1973 (epoch I)~~1954-1973 (epoch I)~~		1973-2006 (epoch II)~~1973-2006 (epoch II)~~		2006-2015 (epoch III)~~2006-2019 (epoch III)~~		I to II~~I to II~~	II to III~~II to III~~
(Horlachtal)	0 to 10~~0 to 10~~	410~~410~~	20.50~~21.58~~	732~~732~~	21.53~~22.18~~	228~~271~~	22.80~~20.85~~	1.03~~0.60~~	1.27~~-1.34~~
	10 to 20~~10 to 20~~	181~~181~~	9.05~~9.53~~	341~~341~~	10.03~~10.33~~	114~~139~~	11.40~~10.69~~	0.98~~0.81~~	1.37~~0.36~~
	20 to 30~~20 to 30~~	113~~113~~	5.65~~5.95~~	191~~191~~	5.62~~5.79~~	46~~70~~	4.60~~5.38~~	-0.03~~-0.16~~	-1.02~~-0.40~~
	30 to 40~~30 to 40~~	47~~47~~	2.35~~2.47~~	101~~101~~	2.97~~3.06~~	35~~41~~	3.50~~3.15~~	0.62~~0.59~~	0.53~~0.09~~
	40 to 50~~40 to 50~~	26~~26~~	1.30~~1.37~~	35~~35~~	1.03~~1.06~~	8~~9~~	0.80~~0.69~~	-0.27~~-0.31~~	-0.23~~-0.37~~
	50 to 60~~50 to 60~~	13~~13~~	0.65~~0.68~~	14~~14~~	0.41~~0.42~~	6~~7~~	0.60~~0.54~~	-0.24~~-0.26~~	0.19~~0.11~~
	60 to 70~~60 to 70~~	0~~0~~	0.00~~0.00~~	6~~6~~	0.18~~0.18~~	1~~1~~	0.10~~0.08~~	0.18~~0.18~~	-0.08~~-0.10~~
	>70~~>70~~	2~~2~~	0.10~~0.11~~	0~~0~~	0.00~~0.00~~	1~~1~~	0.10~~0.08~~	-0.10~~-0.11~~	0.10~~0.08~~
Gepatschferner		1953-1971 (period ~~epoch~~ I)		1971-2006 (period ~~epoch~~ II)		2006-2017 (period ~~epoch~~ III)		I to II	II to III

Formatiert ...
Formatiert ...
Formatiert ...
Formatiert ...
Formatiert ...
Formatiert ...
Formatiert ...
Formatiert ...
Formatiert ...
Formatiert ...
Formatiert ...
Formatiert ...
Formatiert ...
Formatiert ...
Formatiert ...
Formatiert ...
Formatiert ...
Formatiert ...
Formatiert ...
Formatiert ...
Formatiert ...
Formatiert ...
Formatiert ...
Formatiert ...
Formatiert ...
Formatiert ...
Formatiert ...
Formatiert ...
Formatiert ...
Formatiert ...
Formatiert ...
Formatiert ...
Formatiert ...
Formatiert ...
Formatiert ...
Formatiert ...
Formatiert ...
Formatiert ...
Formatiert ...
Formatiert ...
Formatiert ...
Formatiert ...
Formatiert ...
Formatiert ...
Formatierte Tabelle ...

(Kaunertal)	0 to 10~~0 to 10~~	335~~335~~	17.63~~18.61~~	706~~706~~	19.61~~20.17~~	192~~218~~	19.20~~19.82~~	1.98~~1.56~~	-0.44~~-0.35~~
	10 to 20~~10 to 20~~	174~~174~~	9.16~~9.67~~	325~~325~~	9.03~~9.29~~	95~~108~~	9.50~~9.82~~	-0.13~~-0.38~~	0.47~~0.53~~
	20 to 30~~20 to 30~~	105~~105~~	5.53~~5.83~~	224~~224~~	6.22~~6.40~~	61~~67~~	6.10~~6.09~~	0.69~~0.57~~	-0.12~~-0.31~~
	30 to 40~~30 to 40~~	73~~73~~	3.84~~4.06~~	107~~107~~	2.97~~3.06~~	34~~36~~	3.40~~3.27~~	-0.87~~-1.00~~	0.43~~0.22~~
	40 to 50~~40 to 50~~	22~~22~~	1.16~~1.22~~	50~~50~~	1.39~~1.43~~	18~~19~~	1.80~~1.73~~	0.23~~0.21~~	0.41~~0.30~~
	50 to 60~~50 to 60~~	11~~11~~	0.58~~0.61~~	19~~19~~	0.53~~0.54~~	4~~4~~	0.40~~0.36~~	-0.05~~-0.07~~	-0.13~~-0.18~~
	60 to 70~~60 to 70~~	5~~5~~	0.26~~0.28~~	11~~11~~	0.31~~0.31~~	1~~1~~	0.10~~0.09~~	0.05~~0.04~~	-0.21~~-0.22~~
	70 to 80~~70 to 80~~	2~~2~~	0.11~~0.11~~	3~~3~~	0.08~~0.09~~	0~~0~~	0.00~~0.00~~	-0.03~~-0.03~~	-0.08~~-0.09~~
	80 to 90~~80 to 90~~	0~~0~~	0.00~~0.00~~	2~~2~~	0.06~~0.06~~	0~~0~~	0.00~~0.00~~	0.06~~0.06~~	-0.06~~-0.06~~
	90 to 100~~90 to 100~~	0~~0~~	0.00~~0.00~~	5~~5~~	0.14~~0.14~~	2~~2~~	0.20~~0.18~~	0.14~~0.14~~	0.06~~0.04~~
	>100~~>100~~	4~~4~~	0.21~~0.22~~	5~~5~~	0.14~~0.14~~	0~~0~~	0.00~~0.00~~	-0.07~~-0.08~~	-0.14~~-0.14~~
Gepatschferner/		1953-1971 (period ~~epoch~~ I)		1971-2006 (period ~~epoch~~ II)		2006-2017 (period ~~epoch~~ III)		I to II	II to III
Müchner	0 to 10~~0 to 10~~	304~~304~~	16.00~~16.89~~	618~~618~~	17.17~~17.66~~	168~~202~~	16.80~~18.36~~	1.17~~0.77~~	-0.37~~0.71~~
Abfahrt	10 to 20~~10 to 20~~	146~~146~~	7.68~~8.11~~	301~~301~~	8.36~~8.60~~	81~~96~~	8.10~~8.73~~	0.68~~0.49~~	-0.26~~0.13~~
(Kaunertal)	20 to 30~~20 to 30~~	101~~101~~	5.32~~5.61~~	197~~197~~	5.47~~5.63~~	57~~64~~	5.70~~5.82~~	0.15~~0.02~~	0.23~~0.19~~
	30 to 40~~30 to 40~~	69~~69~~	3.63~~3.83~~	115~~115~~	3.19~~3.29~~	34~~36~~	3.40~~3.27~~	-0.44~~-0.55~~	0.21~~-0.01~~
	40 to 50~~40 to 50~~	35~~35~~	1.84~~1.94~~	50~~50~~	1.39~~1.43~~	20~~21~~	2.00~~1.91~~	-0.45~~-0.52~~	0.61~~0.48~~
	50 to 60~~50 to 60~~	12~~12~~	0.63~~0.67~~	26~~26~~	0.72~~0.74~~	6~~6~~	0.60~~0.55~~	0.09~~0.08~~	-0.12~~-0.20~~
	60 to 70~~60 to 70~~	5~~5~~	0.26~~0.28~~	12~~12~~	0.33~~0.34~~	1~~1~~	0.10~~0.09~~	0.07~~0.07~~	-0.23~~-0.25~~
	70 to 80~~70 to 80~~	1~~1~~	0.05~~0.06~~	5~~5~~	0.14~~0.14~~	0~~0~~	0.00~~0.00~~	0.09~~0.09~~	-0.14~~-0.14~~

	>80~~>80~~	4~~4~~	0.21~~0.22~~	10~~10~~	0.28~~0.29~~	2~~2~~	0.20~~0.18~~	0.07~~0.06~~	-0.08~~-0.10~~
Weißseeferner		1953-1971 (period ~~epoch~~ I)		1971-2006 (period ~~epoch~~ II)		2006-2017 (period ~~epoch~~ III)		I to II	II to III
(Kaunertal)	0 to 10~~0 to 10~~	302~~302~~	15.89~~16.78~~	623~~623~~	17.31~~17.80~~	179~~212~~	17.90~~19.27~~	1.42~~1.02~~	0.59~~1.47~~
	10 to 20~~10 to 20~~	146~~146~~	7.68~~8.11~~	296~~296~~	8.22~~8.46~~	88~~104~~	8.80~~9.45~~	0.54~~0.35~~	0.58~~1.00~~
	20 to 30~~20 to 30~~	99~~99~~	5.21~~5.50~~	203~~203~~	5.64~~5.80~~	53~~60~~	5.30~~5.45~~	0.43~~0.30~~	-0.34~~-0.35~~
	30 to 40~~30 to 40~~	75~~75~~	3.95~~4.17~~	104~~104~~	2.89~~2.97~~	32~~34~~	3.20~~3.09~~	-1.06~~-1.20~~	0.31~~0.12~~
	40 to 50~~40 to 50~~	32~~32~~	1.68~~1.78~~	46~~46~~	1.28~~1.31~~	18~~19~~	1.80~~1.73~~	-0.40~~-0.46~~	0.52~~0.41~~
	50 to 60~~50 to 60~~	12~~12~~	0.63~~0.67~~	28~~28~~	0.78~~0.80~~	6~~6~~	0.60~~0.55~~	0.15~~0.13~~	-0.18~~-0.25~~
	60 to 70~~60 to 70~~	3~~3~~	0.16~~0.17~~	14~~14~~	0.39~~0.40~~	1~~1~~	0.10~~0.09~~	0.23~~0.23~~	-0.29~~-0.31~~
	70 to 80~~70 to 80~~	1~~1~~	0.05~~0.06~~	3~~3~~	0.08~~0.09~~	1~~1~~	0.10~~0.09~~	0.03~~0.03~~	0.02~~0.01~~
	80 to 90~~80 to 90~~	1~~1~~	0.05~~0.06~~	4~~4~~	0.11~~0.11~~	1~~1~~	0.10~~0.09~~	0.06~~0.06~~	-0.01~~-0.02~~
	>90~~>90~~	3~~3~~	0.16~~0.17~~	6~~6~~	0.17~~0.17~~	0~~0~~	0.00~~0.00~~	0.01~~0.00~~	-0.17~~-0.17~~
Hohenferner		1959-2005 (period ~~epoch~~ I)				2005-2019 (period ~~epoch~~ II)		I to II	
(Martelltal)	0 to 10~~0 to 10~~	1169~~1169~~	24.35~~25.41~~			323~~387~~	29.36~~27.64~~	5.01~~2.23~~	
	10 to 20~~10 to 20~~	403~~403~~	8.40~~8.76~~			105~~127~~	9.55~~9.07~~	1.15~~0.31~~	
	20 to 30~~20 to 30~~	241~~241~~	5.02~~5.24~~			40~~50~~	3.64~~3.57~~	-1.38~~-1.67~~	
	30 to 40~~30 to 40~~	127~~127~~	2.65~~2.76~~			31~~34~~	2.82~~2.43~~	0.17~~-0.33~~	
	40 to 50~~40 to 50~~	54~~54~~	1.13~~1.17~~			15~~18~~	1.36~~1.29~~	0.23~~0.11~~	
	50 to 60~~50 to 60~~	27~~27~~	0.56~~0.59~~			9~~11~~	0.82~~0.79~~	0.26~~0.20~~	

60 to 70~~60 to 70~~	38~~38~~	0.79~~0.83~~	8~~10~~	0.73~~0.71~~	-0.06~~-0.11~~
70 to 80~~70 to 80~~	16~~16~~	0.33~~0.35~~	3~~4~~	0.27~~0.29~~	-0.06~~-0.06~~
80 to 90~~80 to 90~~	24~~24~~	0.50~~0.52~~	5~~5~~	0.45~~0.36~~	-0.05~~-0.16~~
90 to 100~~90 to 100~~	5~~5~~	0.10~~0.11~~	3~~3~~	0.27~~0.21~~	0.17~~0.11~~
100 to 110~~100 to 110~~	5~~5~~	0.10~~0.11~~	1~~1~~	0.09~~0.07~~	-0.01~~-0.04~~
110 to 120~~110 to 120~~	5~~5~~	0.10~~0.11~~	0~~0~~	0.00~~0.00~~	-0.10~~-0.11~~
120 to 130~~120 to 130~~	4~~4~~	0.08~~0.09~~	1~~1~~	0.09~~0.07~~	0.01~~-0.02~~
130 to 140~~130 to 140~~	5~~5~~	0.10~~0.11~~	0~~0~~	0.00~~0.00~~	-0.10~~-0.11~~

Code availability

The processing of the historical aerial images into point clouds (and orthophotos) was done with the commercial software Agisoft Metashape Professional (Version 1.6.6). These point clouds as well as the point clouds based on LiDAR data (ALS) were further processed in the commercial geoinformation system SAGA LIS Pro 3D (Version 7.4.0) and converted into DEMs. The preparatory steps for the regression lines (derivation of the corresponding value pairs (sediment yield ~~SY~~ and sediment contributing area~~SCA~~)) were carried out in open-source software SAGA GIS (Version 7.2.0), whereby the subsequent automated repetition of the extraction of the value pairs by using a for-loop and the calculation of the corresponding regression lines were carried out in the open-source software R (RStudio, version 1.4.1103). Maps were created in both the open-source software SAGA GIS and QGIS (Version 3.22.4). Atmospheric simulation was performed using the Advanced Research version of the Weather Research and Forecasting (ARW-WRF) model (version 4.3). The meteorological analyses were carried out in R.

Data availability

The historical aerial images~~ (HAI)~~ and the corresponding calibration certificates (if available) were provided by the Federal Office of Metrology and Surveying (BEV, Vienna, Austria) (aerial image series 1953 and 1954), by the Italian Military Geographic Institute (IGMI, Florence, Italy) (aerial image series 1945 and 1959) and by the Province of Tyrol (aerial image series 1970, 1971 and 1973). The DEM 2006 (Horlachtal) and the point clouds of 2006 and 2004/2005 (Kaunertal and

Martelltal) were provided by the Province of Tyrol and the Autonomous Province of Bolzano. The historical maps of 1886/1887 (Kaunertal), 1889 (Horlachtal), 1918 (Martelltal) and 1922 (Kaunertal) were provided by the Archive of the German Alpine Club (DAV), the Ötztal Gedächtnisspeicher (Längenfeld, Austria), the BEV and the Bavarian Academy of Sciences and Humanities. The orthophotos of 2020 (all valleys) were made available for download by the Province of Tyrol and the Autonomous Province of Bolzano on their respective websites. The large-scale elevation data (DSM and Hillshade) (Overview European Alps, Figure 1) was provided by Copernicus (Copernicus Land Monitoring Service). These data were produced with the financial support of the European Union. The 20th century NOAA/CIRES/DOE reanalysis data (V3) were provided by NOAA PSL, Boulder, Colorado, USA, from their website https://psl.noaa.gov. Support for the Twentieth Century Reanalysis Project version 3 dataset is provided by the U.S. Department of Energy, Office of Science Biological and Environmental Research (BER), by the National Oceanic and Atmospheric Administration Climate Program Office, and by the NOAA Earth System Research Laboratory Physical Sciences Laboratory.⦣8364.~~;~~ ~~The ERA5 dataset we used is a Copernicus product. It contains processed information from the Copernicus Climate Change Service [2021] and the Copernicus Atmosphere Monitoring Service [2021]. Please note that neither the European Commission nor the European Centre for Medium-Range Weather Forecasts is responsible for any use that may be made of the Copernicus information or data contained therein.~~

Author contribution

The study was conceptualised by MA, FH, TH and MB. Data preparation was carried out by MA, JR, FF, FH, LP, MP, MW, LB, MS and SB-N. The methodological approach was developed by MA, JR, FH and TH for the sediment contributing area ~~SCA~~ modelling and MA, FH and MP for the meteorological analysis. The formal analysis was carried out by MA and MP. Supervision was carried out by FH, TH and MB. The original draft was prepared by MA. JR, FF, FH, TH, LP, MP, MW, LB, MS, SB-N and MB were involved in the revision of the manuscript. MB, FH and TH were responsible for fundraising and project management.

Competing interests

The authors declare that they have no conflict of interest.

Acknowledgement

We would like to thank the German Research Foundation (DFG), the Austrian Science Fund (FWF) and the Swiss National Science Foundation (SNF) for financial support of the research project SEHAG (SEnsitivity of High Alpine Geosystems to climate change since 1850), within the framework of which this study was generated. Furthermore, we would like to thank for providing the aerial images and the calibration certificates. In this context, we would like to thank the BEV, IGMI, the Province of Tyrol, the Province of Bolzano and the Hydrographic Office of the Autonomous Province of Bolzano (Civil Protection Agency). In addition, we would also like to thank the Province of Tyrol for providing the DEM 2006 (Horlachtal) as well as the point cloud 2006 (Kaunertal) and the Autonomous Province of Bolzano for the point cloud 2006 (Martelltal). We would also like to thank the Archive of the German Alpine Club (DAV), the Ötztaler Gedächtnisspeicher, the BEV and the Bavarian Academy of Sciences and Humanities for providing the historical maps 1886/1887 (Kaunertal), 1889 (Horlachtal), 1918 (Martelltal) and 1922 (Kaunertal). We would also like to thank the Province of Tyrol and the Autonomous Province of Bolzano for the orthophotos of 2020, which can be downloaded on their websites quickly and easily. We would also like to thank Copernicus (Copernicus Land Monitoring Service) for the available download of the coarse resolution hillshade (Overview European Alps, Figure 1). Additionally, we would like to thank Wucher Helikopter GmbH (Ludesch, Austria) for carrying out the flights in which the LiDAR data (ALS) 2017 (Kaunertal) and 2019 (Horlachtal and Martelltal) were acquired. Many thanks for the safe flights even in difficult high alpine terrain. In addition, many thanks to NOAA PSL, Boulder, Colorado, USA for the 20CRv3 ~~and Copernicus for the ERA5~~ dataset.

Funding

The study was financially supported by the German Research Foundation (DFG) and the Austrian Science Fund (FWF) (grant numbers: BE 1118/38-1, BE 1118/39-1, BE 1118/40-1, HA 5740/10-1, HE 5747/6-1, MA 6966/4-1, LA 4426/1-1 and 4062-N29). The open access publication of this article was supported by the Open Access Fund of the Catholic University of Eichstätt-Ingolstadt.

References

Altmann, M., Piermattei, L., Haas, F., Heckmann, T., Fleischer, F., Rom, J., Betz-Nutz, S., Knoflach, B., Müller, S., Ramskogler, K., Pfeiffer, M., Hofmeister, F., Ressl, C., and Becht, M.: Long-Term Changes of Morphodynamics on Little Ice Age Lateral Moraines and the Resulting Sediment Transfer into Mountain Streams in the Upper Kauner Valley, Austria, Water, 12, 3375, https://doi.org/10.3390/w12123375, 2020.

Altmann, M., Haas, F., Heckmann, T., Liébault, F., and Becht, M.: Modelling of sediment supply from torrent catchments in the Western Alps using the sediment contributing area (SCA) approach, Earth Surf. Process. Landforms, 46, 889–906, https://doi.org/10.1002/esp.5046, 2021.

Anderson, S. W.: Uncertainty in quantitative analyses of topographic change: error propagation and the role of thresholding, Earth Surf. Process. Landforms, 44, 1015–1033, https://doi.org/10.1002/esp.4551, 2019.

Bakker, M. and Lane, S.: Archival photogrammetric analysis of river-floodplain systems using Structure from Motion (SfM) methods, Earth Surf. Process. Landforms, 42, 1274–1286, https://doi.org/10.1002/esp.4085, 2017.

Ballantyne, C. K.: A general model of paraglacial landscape response, The Holocene, 12, 371–376, https://doi.org/10.1191/0959683602hl553fa, 2002a.

Ballantyne, C. K.: Paraglacial geomorphology, Quaternary Science Reviews, 21, 1935–2017, https://doi.org/10.1016/S0277-3791(02)00005-7, 2002b.

Ballantyne, C. K. and Benn, D. I.: Paraglacial slope adjustment during recent deglaciation and its implications for slope evolution in formerly glaciated environments, Anderson, M. G., & Brooks, S. M. (eds.), Advances in hillslope processes, 2, 1173–1195, 1996.

Ballantyne, C. K. and Benn, D. I.: Paraglacial Slope Adjustment and Resedlmenfation following Recent Glacier Retreat, Fåbergstølsdalen, Norway, Arctic and Alpine Research, 26, 255–269, 1994.

Becht, M.: Untersuchungen zur aktuellen Reliefentwicklung in alpinen Einzugsgebieten, Univ., Habil.-Schr, Münchener Universitätsschriften/Fakultät für Geowissenschaften, 47, Geobuch-Verl., Germany, München, 187 pp., 1995.

Beniston, M., Farinotti, D., Stoffel, M., Andreassen, L. M., Coppola, E., Eckert, N., Fantini, A., Giacona, F., Hauck, C., Huss, M., Huwald, H., Lehning, M., López-Moreno, J.-I., Magnusson, J., Marty, C., Morán-Tejéda, E., Morin, S., Naaim, M., Provenzale, A., Rabatel, A., Six, D., Stötter, J., Strasser, U., Terzago, S., and Vincent, C.: The European mountain cryosphere: a review of its current state, trends, and future challenges, The Cryosphere, 12, 759–794, https://doi.org/10.5194/tc-12-759-2018, 2018.

Besl, P. J. and McKay, N. D.: Method for registration of 3-D shapes, in: Sensor Fusion IV: Control Paradigms and Data Structures, Boston, MA, Friday 1 November 1991, 586–606, 1992.

Betz, S., Croce, V., and Becht, M.: Investigating morphodynamics on Little Ice Age lateral moraines in the Italian Alps using archival aerial photogrammetry and airborne LiDAR data, Zeitschrift für Geomorphologie, 62, 231–247, https://doi.org/10.1127/zfg/2019/0629, 2019.

Betz-Nutz, S.: Vergleichende photogrammetrische Untersuchungen zu langfristigen Veränderungen der Morphodynamik auf neuzeitlichen Lateralmoränen ausgewählter Alpengletscher, Dissertation, Universitätsbibliothek Eichstätt-Ingolstadt, Eichstätt, 2021.

Betz-Nutz, S., Heckmann, T., Haas, F., and Becht, M.: Development of the morphodynamics on Little Ice Age lateral moraines in 10 glacier forefields of the Eastern Alps since the 1950s, Earth Surf. Dynam., 11, 203–226, https://doi.org/10.5194/esurf-11-203-2023, 2023.

Blair, R. W.: Moraine and Valley Wall Collapse due to Rapid Deglaciation in Mount Cook National Park, New Zealand, Mountain Research and Development, 14, 347, https://doi.org/10.2307/3673731, 1994.

Brugnara, Y., Brunetti, M., Maugeri, M., Nanni, T., and Simolo, C.: High-resolution analysis of daily precipitation trends in the central Alps over the last century, Int. J. Climatol., 32, 1406–1422, https://doi.org/10.1002/joc.2363, 2012.

Carrivick, J. L., Geilhausen, M., Warburton, J., Dickson, N. E., Carver, S. J., Evans, A. J., and Brown, L. E.: Contemporary geomorphological activity throughout the proglacial area of an alpine catchment, Geomorphology, 188, 83–95, https://doi.org/10.1016/j.geomorph.2012.03.029, 2013.

Cavalli, M., Goldin, B., Comiti, F., Brardinoni, F., and Marchi, L.: Assessment of erosion and deposition in steep mountain basins by differencing sequential digital terrain models, Geomorphology, 291, 4–16, https://doi.org/10.1016/j.geomorph.2016.04.009, 2017.

Chen, F. and Dudhia, J.: Coupling an Advanced Land Surface–Hydrology Model with the Penn State–NCAR MM5 Modeling System. Part II: preliminary model validation, Mon. Wea. Rev., 129, 569–585, https://doi.org/10.1175/1520-0493(2001)129<0569:CAALSH>2.0.CO;2, 2001.

Church, M. and Ryder, J. M.: Paraglacial Sedimentation: A Consideration of Fluvial Processes Conditioned by Glaciation, Geol Soc America Bull, 83, 3059, https://doi.org/10.1130/0016-7606(1972)83[3059:PSACOF]2.0.CO;2, 1972.

Cody, E., Anderson, B. M., McColl, S. T., Fuller, I. C., and Purdie, H. L.: Paraglacial adjustment of sediment slopes during and immediately after glacial debuttressing, Geomorphology, 371, 107411, https://doi.org/10.1016/j.geomorph.2020.107411, available at: https://www.sciencedirect.com/science/article/pii/S0169555X20303846, 2020.

Collier, E. and Mölg, T.: BAYWRF: a high-resolution present-day climatological atmospheric dataset for Bavaria, Earth Syst. Sci. Data, 12, 3097–3112, https://doi.org/10.5194/essd-12-3097-2020, 2020.

Collier, E., Sauter, T., Mölg, T., and Hardy, D.: The Influence of Tropical Cyclones on Circulation, Moisture Transport, and Snow Accumulation at Kilimanjaro During the 2006–2007 Season, J. Geophys. Res. Atmos., 124, 6919–6928, https://doi.org/10.1029/2019JD030682, 2019.

Compo, G. P., Whitaker, J. S., Sardeshmukh, P. D., Matsui, N., Allan, R. J., Yin, X., Gleason, B. E., Vose, R. S., Rutledge, G., Bessemoulin P., Brönnimann, S., Brunet, M., Crouthamel, R. I., Grant, A. N., Groisman, P. Y., Jones, P. D., Kruk, M., Kruger, A. C., Marshall, G. J., Maugeri, M., Mok, H. Y., Nordli, Ø., Ross, T. F., Trigo, R. M., Wang, X. L., Woodruff, S. D., and Worley, S. J.: The Twentieth Century Reanalysis Project, Quarterly J. Roy. Meteorol. Soc., 137, 1–28, 2011.

Conrad, O., Bechtel, B., Bock, M., Dietrich, H., Fischer, E., Gerlitz, L., Wehberg, J., Wichmann, V., and Böhner, J.: System for Automated Geoscientific Analyses (SAGA) v. 2.1.4, Geoscientific Model Development, 8, 1991–2007, 2015.

Copernicus: Hillshade derived from EU-DEM version 1.0, https://land.copernicus.eu/imagery-in-situ/eu-dem/eu-dem-v1-0-and-derived-products/hillshade?tab=metadata, last access: 3 June 2021, 2016.

Curry, A. M.: Paraglacial modification of slope form, Earth Surf. Process. Landforms, 24, 1213–1228, https://doi.org/10.1002/(SICI)1096-9837(199912)24:13<1213:AID-ESP32>3.0.CO;2-B, 1999.

Curry, A. M., Cleasby, V., and Zukowskyj, P.: Paraglacial response of steep, sediment-mantled slopes to post-‘Little Ice Age’ glacier recession in the central Swiss Alps, J. Quaternary Sci., 21, 211–225, https://doi.org/10.1002/jqs.954, 2006.

Curry, A. M., Sands, T. B., and Porter, P. R.: Geotechnical controls on a steep lateral moraine undergoing paraglacial slope adjustment, Geological Society, London, Special Publications, 320, 181–197, https://doi.org/10.1144/SP320.12, 2009.

Deline, P., Gruber, S., Delaloye, R., Fischer, L., Geertsema, M., Giardino, M., Hasler, A., Kirkbride, M., Krautblatter, M., Magnin, F., McColl, S., Ravanel, L., and Schoeneich, P.: Chapter 15 - Ice Loss and Slope Stability in High-Mountain

Regions, in: Shroder, J.F; Haeberli, W; Whiteman, C; Hazards and Disasters Series, Snow and Ice-Related Hazards, Risks, and Disasters, Academic press, 521–561, https://doi.org/10.1016/B978-0-12-394849-6.00015-9.

Draebing, D. and Eichel, J.: Spatial Controls of Turf-Banked Solifluction Lobes and Their Role for Paraglacial Adjustment in Glacier Forelands, Permafrost and Periglacial Processes, 28, 446–459, https://doi.org/10.1002/ppp.1930, 2017.

Dusik, J.: Die aktuelle Geomorphodynamik auf proglazialen Moränen im Hinteren Kaunertal: Hochaufgelöste Messung und Modellierung der Prozessdynamik hinsichtlich ihrer lokalen und temporalen Variabilität, Dissertation, Katholische Universität Eichstätt-Ingolstadt, Eichstätt, 2019.

Dusik, J.-M., Neugirg, F., and Haas, F.: Slope Wash, Gully Erosion and Debris Flows on Lateral Moraines in the Upper Kaunertal, Austria, in: Geomorphology of Proglacial Systems, Springer, Cham, 177–196, https://doi.org/10.1007/978-3-319-94184-4_11, 2019.

Eichel, J., Corenblit, D., and Dikau, R.: Conditions for feedbacks between geomorphic and vegetation dynamics on lateral moraine slopes: a biogeomorphic feedback window, Earth Surface Processes and Landforms, 41, 406–419, https://doi.org/10.1002/esp.3859, 2016.

Eichel, J., Draebing, D., Winkler, S., and Meyer, N.: Similar vegetation-geomorphic disturbance feedbacks shape unstable glacier forelands across mountain regions, Ecosphere, 14, https://doi.org/10.1002/ecs2.4404, 2023.

Eltner, A., Kaiser, A., Castillo, C., Rock, G., Neugirg, F., and Abellán, A.: Image-based surface reconstruction in geomorphometry – merits, limits and developments, Earth Surf. Dynam., 4, 359–389, https://doi.org/10.5194/esurf-4-359-2016, 2016.

Fehlmann, M., Gascón, E., Rohrer, M., Schwarb, M., and Stoffel, M.: Estimating the snowfall limit in alpine and pre-alpine valleys: A local evaluation of operational approaches, Atmospheric Research, 204, 136–148, https://doi.org/10.1016/j.atmosres.2018.01.016, 2018.

Finsterwalder, S.: Begleitworte zur Karte des Gepatschferners, Zeitschrift für Gletscherkunde XVI (1/2), 20–41, 1928.

Finsterwalder, S. and Schunck, H.: Die Zunge des Gepatschferners 1886/87, Zeitschrift des Deutschen und Oesterreichischen Alpenvereins, Tafel 4, 1888.

Fleischer, F., Haas, F., Piermattei, L., Pfeiffer, M., Heckmann, T., Altmann, M., Rom, J., Stark, M., Wimmer, H. W., Pfeifer, N., and Becht, M.: Multi-decadal (1953–2017) rock glacier kinematics analysed by high-resolution topographic data in the upper Kaunertal, Austria, The Cryosphere, 15, 5345–5369, https://doi.org/10.5194/tc-15-5345-2021, 2021.

Froidurot, S., Zin, I., Hingray, B., and Gautheron, A.: Sensitivity of Precipitation Phase over the Swiss Alps to Different Meteorological Variables, Journal of Hydrometeorology, 15, 685–696, https://doi.org/10.1175/JHM-D-13-073.1, available at: https://journals.ametsoc.org/view/journals/hydr/15/2/jhm-d-13-073_1.xml, 2014.

Fryirs, K.: (Dis)Connectivity in catchment sediment cascades: a fresh look at the sediment delivery problem, Earth Surf. Process. Landforms, 38, 30–46, https://doi.org/10.1002/esp.3242, 2013.

Fryirs, K. A., Brierley, G. J., Preston, N. J., and Spencer, J.: Catchment-scale (dis)connectivity in sediment flux in the upper Hunter catchment, New South Wales, Australia, Geomorphology, 84, 297–316, https://doi.org/10.1016/j.geomorph.2006.01.044, 2007.

Geitner, C.: Sedimentologische und vegetationsgeschichtliche Untersuchungen an fluvialen Sedimenten in den Hochlagen des Horlachtales (Stubaier Alpen, Tirol): ein Beitrag zur zeitlichen Differenzierung der fluvialen Dynamik im Holozän, vol. 31 of Münchener Geographische Abhandlungen A, Geobuch-Verlag, Diss., München, 1999.

Geological Survey of Austria: Geological map of Austria, 1:2.000.000, Vienna, 1999.

Giese, B. S., Seidel, H. F., Compo, G. P., and Sardeshmukh, P. D.: An ensemble of ocean reanalyses for 1815–2013 with sparse observational input, J. Geophys. Res. Oceans, 121, 6891–6910, https://doi.org/10.1002/2016JC012079, 2016.

Gomez, C., Hayakawa, Y., and Obanawa, H.: A study of Japanese landscapes using structure from motion derived DSMs and DEMs based on historical aerial photographs: New opportunities for vegetation monitoring and diachronic geomorphology, Geomorphology, 242, 11–20, https://doi.org/10.1016/j.geomorph.2015.02.021, 2015.

Groß, G. and Patzelt, G.: The Austrian Glacier Inventory for the Little Ice Age Maximum (GI LIA) in ArcGIS (shapefile) format, 2015.

Haas, F.: Fluviale Hangprozesse in alpinen Einzugsgebieten der nördlichen Kalkalpen: Quantifizierung und Modellierungsansätze, Dissertation, Katholische Universität Eichstätt-Ingolstadt, Eichstätt, 2008.

Haas, F., Heckmann, T., Hilger, L., and Becht, M.: Quantification and Modelling of Debris Flows in the Proglacial Area of the Gepatschferner/Austria using Ground-based LIDAR, Collins, Adrian L. ; Golosov, Valentin ; Horowitz, Arthur J. ; Lu, Xixi ; Stone, Mike ; Walling, Des E. ; Zhang, Xinbao (Eds.): Erosion and Sediment Yields in the Changing Environment: proceedings of an IAHS International Commission on Continental Erosion Symposium, held at the Institute of Mountain Hazards and Environment, CAS-Chengdu, China, 11-15 October 2012, IAHS publication, 356, 293–302, 2012.

Haas, F., Heckmann, T., Wichmann, V., and Becht, M.: Quantification and Modeling of Fluvial Bedload Discharge from Hillslope Channels in two Alpine Catchments (Bavarian Alps, Germany), Zeitschrift für Geomorphologie N.F. Suppl., 55, 147–168, https://doi.org/10.1127/0372-8854/2011/0055S3-0056, 2011.

Haeberli, W. and Whiteman, C.: Snow and Ice-Related Hazards, Risks, and Disasters, Elsevier, 2021.

Hagg, W. and Becht, M.: Einflüsse von Niederschlag und Substrat auf die Auslösung von Hangmuren in Beispielgebieten der Ostalpen, Zeitschrift für Geomorphologie, 79–92, 2000.

Haselberger, S., Zangerl, U., Scheper, S., Otto, J.-C., Ohler, L.-M., Junker, R. R., and Kraushaar, S.: Catchment-Scale Stability and Disturbance in Biogeomorphic Succession in an Alpine Glacier Foreland (Kaunertal Valley, Austria), SSRN Journal, https://doi.org/10.2139/ssrn.4202209, 2022.

Haselberger, S., Ohler, L.-M., Junker, R. R., Otto, J.-C., Glade, T., and Kraushaar, S.: Quantification of biogeomorphic interactions between small-scale sediment transport and primary vegetation succession on proglacial slopes of the Gepatschferner, Austria, Earth Surf. Process. Landforms, 46, 1941–1952, https://doi.org/10.1002/esp.5136, 2021.

Heckmann, T. and Vericat, D.: Computing spatially distributed sediment delivery ratios: inferring functional sediment connectivity from repeat high-resolution digital elevation models, Earth Surf. Process. Landforms, 43, 1547–1554, https://doi.org/10.1002/esp.4334, 2018.

Heckmann, T. and Morche, D. (Eds.): Geomorphology of proglacial systems: Landform and sediment dynamics in recently deglaciated alpine landscapes, Geography of the Physical Environment, Springer International Publishing, Cham, Switzerland, 2019.

Heinimann, H., Hollenstein, K., Kienholz, H., Krummenacher, B., and Mani, P.: Methoden zur Analyse und Bewertung von Naturgefahren, 85, Umwelt-Materialien, BUWAL - Bundesamt für Umwelt, Wald und Landschaft, Bern, 1998.

Hersbach, H., Bell, B., Berrisford, P., Biavati, G., Horányi, A., Muñoz Sabater, J., Nicolas, J., Peubey, C., Radu, R., Rozum, I., Schepers, D., Simmons, A., Soci, C., Dee, D., and Thépaut, J.-N.: ERA5 hourly data on single levels from 1979 to present: Copernicus Climate Change Service (C3S) Climate Data Store (CDS), https://doi.org/10.24381/cds.adbb2d47, last access: 13 October 2021, 2018.

Hilger, L.: Quantification and regionalization of geomorphic processes using spatial models and high-resolution topographic data: A sediment budget of the Upper Kauner Valley, Ötztal Alps., Dissertation, Katholische Universität Eichstätt-Ingolstadt, Eichstätt, 2017.

Hock, R., Rasul, G., Adler, C., Cáceres, B., Gruber, S., Hirabayashi, Y.: Jackson, M., Kääb, A., Kang, S., Kutuzov, S., and Milner, A. L.: High Mountain Areas: In: IPCC Special Report on the Ocean and Cryosphere in a Changing Climate [H.-O. Pörtner, D.C. Roberts, V. Masson-Delmotte, P. Zhai, M. Tignor, E. Poloczanska, K. Mintenbeck, A. Alegría, M. Nicolai, A. Okem, J. Petzold, B. Rama, N.M. Weyer (eds.)]. Cambridge University Press, Cambridge, UK and New York, NY, USA, 131–202, https://doi.org/10.1017/9781009157964.004, 2019.

Hodgson, M. E. and Bresnahan, P.: Accuracy of Airborne Lidar-Derived Elevation, https://doi.org/10.14358/PERS.70.3.331, 2004.

Hong, S. Y., Noh, Y., and Dudhia, J.: A new vertical diffusion package with an explicit treatment of entrainment processes, Mon. Weather Rev., 134, 2318–2341, https://doi.org/10.1175/MWR3199.1, 2006.

Huber, A., Heckmann, T., Haas, F., and Becht, M.: DEM-based scaling of bedload sediment yield in low-order torrents of the Isar catchment, In. Guidelines for Assessing Sediment Dynamics in Alpine Basins and Channel Reaches: Final Report of the SedAlp Project, Work Package 4. SedAlp, Vienna; Annex 39-46, 2015.

Hugenholtz, C. H., Moorman, B. J., Barlow, J., and Wainstein, P. A.: Large-scale moraine deformation at the Athabasca Glacier, Jasper National Park, Alberta, Canada, Landslides, 5, 251–260, https://doi.org/10.1007/s10346-008-0116-5, 2008.

Iacono, M. J., Delamere, J. S., Mlawer, E. J., Shephard, M. W., Clough, S. A., and Collins, W. D.: Radiative forcing by long-lived greenhouse gases: Calculations with the AER radiative transfer models, J. Geophys. Res., 113, https://doi.org/10.1029/2008JD009944, 2008.

IPCC: Climate Change 2021: The Physical Science Basis. Contribution of Working Group I to the Sixth Assessment Report of the Intergovernmental Panel on Climate Change [Masson-Delmotte, V., P. Zhai, A. Pirani, S.L. Connors, C. Péan, S. Berger, N. Caud, Y. Chen, L. Goldfarb, M.I. Gomis, M. Huang, K. Leitzell, E. Lonnoy, J.B.R. Matthews, T.K. Maycock, T. Waterfield, O. Yelekçi, R. Yu, and B. Zhou (eds.)], Cambridge University Press. In Press, 2021.

Ivy-Ochs, S., Kerschner, H., Maisch, M., Christl, M., Kubik, P. W., and Schlüchter, C.: Latest Pleistocene and Holocene glacier variations in the European Alps, Quaternary Science Reviews, 28, 2137–2149, https://doi.org/10.1016/j.quascirev.2009.03.009, 2009.

Jäger, D. and Winkler, S.: Paraglacial processes on the glacier foreland of Vernagtferner (Ötztal Alps, Austria), Zeit fur Geo Supp, 56, 95–113, https://doi.org/10.1127/0372-8854/2012/S-00099, 2012.

Jiménez, P. A., Dudhia, J., González-Rouco, J. F., Navarro, J., Montávez, J. P., and García-Bustamante, E.: A Revised Scheme for the WRF Surface Layer Formulation, Mon. Wea. Rev., 140, 898–918, https://doi.org/10.1175/mwr-d-11-00056.1, 2012.

Kain, J. S.: The Kain–Fritsch Convective Parameterization: An Update, Journal of Applied Meteorology and Climatology, 43, 170–181, https://doi.org/10.1175/1520-0450(2004)043<0170:TKCPAU>2.0.CO;2, available at: https://journals.ametsoc.org/view/journals/apme/43/1/1520-0450_2004_043_0170_tkcpau_2.0.co_2.xml, 2004.

Klein, G., Vitasse, Y., Rixen, C., Marty, C., and Rebetez, M.: Shorter snow cover duration since 1970 in the Swiss Alps due to earlier snowmelt more than to later snow onset, Climatic Change, 139, 637–649, https://doi.org/10.1007/s10584-016-1806-y, 2016.

Lane, S., Bakker, M., Gabbud, C., Micheletti, N., and Saugy, J.-N.: Sediment export, transient landscape response and catchment-scale connectivity following rapid climate warming and Alpine glacier recession, Geomorphology, 277, 210–227, https://doi.org/10.1016/j.geomorph.2016.02.015, available at: http://dx.doi.org/10.1016/j.geomorph.2016.02.015, 2017.

Lane, S. N., Westaway, R. M., and Murray Hicks, D.: Estimation of erosion and deposition volumes in a large, gravel-bed, braided river using synoptic remote sensing, Earth Surf. Process. Landforms, 28, 249–271, https://doi.org/10.1002/esp.483, 2003.

Mair, V. and Purtscheller, F.: Exkursion E: Geologie und Petrologie des Ortlerkristallins, Mitteilungen der Österreichischen Mineralogischen Gesellschaft, 285–303, 1996.

Mair, V., Nocker, C., and Tropper, P.: Das Ortler-Campo Kristallin in Südtirol, Mitteilungen der Österreichischen Mineralogischen Gesellschaft, 219–240, 2007.

Mankin, J. S. and Diffenbaugh, N. S.: Influence of temperature and precipitation variability on near-term snow trends, Clim Dyn, 45, 1099–1116, https://doi.org/10.1007/s00382-014-2357-4, 2015.

Matthews, J. A. and Briffa, K. R.: The ‘little ice age’: re-evaluation of an evolving concept, Geografiska Annaler: Series A, Physical Geography, 87, 17–36, https://doi.org/10.1111/j.0435-3676.2005.00242.x, 2005.

Mattson, L. E. and Gardner, J. S.: Mass Wasting on Valley-Side Ice-Cored Moraines, Boundary Glacier, Alberta, Canada, Geografiska Annaler: Series A, Physical Geography, 73, 123–128, https://doi.org/10.1080/04353676.1991.11880337, 1991.

Midgley, N. G. and Tonkin, T. N.: Reconstruction of former glacier surface topography from archive oblique aerial images, Geomorphology, 282, 18–26, https://doi.org/10.1016/j.geomorph.2017.01.008, 2017.

Mölg, N. and Bolch, T.: Structure-from-Motion Using Historical Aerial Images to Analyse Changes in Glacier Surface Elevation, Remote Sensing, 9, 1021, https://doi.org/10.3390/rs9101021, available at: https://www.mdpi.com/228032, 2017.

Morrison, H., Thompson, G., and Tatarskii, V.: Impact of Cloud Microphysics on the Development of Trailing Stratiform Precipitation in a Simulated Squall Line: Comparison of One- and Two-Moment Schemes, Mon. Wea. Rev., 137, 991–1007, https://doi.org/10.1175/2008MWR2556.1, available at: https://journals.ametsoc.org/view/journals/mwre/137/3/2008mwr2556.1.xml?tab_body=pdf, 2009.

Nebiker, S., Lack, N., and Deuber, M.: Building Change Detection from Historical Aerial Photographs Using Dense Image Matching and Object-Based Image Analysis, Remote Sensing, 6, 8310–8336, https://doi.org/10.3390/rs6098310, 2014.

Neugirg, F., Kaiser, A., Huber, A., Heckmann, T., Schindewolf, M., Schmidt, J., Becht, M., and Haas, F.: Using terrestrial LiDAR data to analyse morphodynamics on steep unvegetated slopes driven by different geomorphic processes, CATENA, 142, 269–280, https://doi.org/10.1016/j.catena.2016.03.021, 2016.

Neugirg, F., Kaiser, A., Schmidt, J., Becht, M., and Haas, F.: Quantification, analysis and modelling of soil erosion on steep slopes using LiDAR and UAV photographs, Proc. IAHS, 367, 51–58, 2015a.

Neugirg, F., Kaiser, A., Schindewolf, M., Becht, M., Schmidt, J., and Haas, F.: Monitoring and modeling slope dynamics in an Alpine watershed - a combined approach of soil science remote sensing and geomorphology, Proc. IAHS, 371, 181–187, 2015b.

Noto, L. V., Bastola, S., Dialynas, Y. G., Arnone, E., and Bras, R. L.: Integration of fuzzy logic and image analysis for the detection of gullies in the Calhoun Critical Zone Observatory using airborne LiDAR data, ISPRS Journal of Photogrammetry and Remote Sensing, 126, 209–224, https://doi.org/10.1016/j.isprsjprs.2017.02.013, 2017.

O'Callaghan, J. F. and Mark, D. M.: The extraction of drainage networks from digital elevation data. Computer vision, graphics, and image processing, Computer vision, graphics, and image processing, 28, 323–344, 1984.

Okyay, U., Telling, J., Glennie, C. L., and Dietrich, W. E.: Airborne lidar change detection: An overview of Earth sciences applications, Earth-Science Reviews, 198, 102929, https://doi.org/10.1016/j.earscirev.2019.102929, 2019.

Pelletier, J. D. and Orem, C. A.: How do sediment yields from post-wildfire debris-laden flows depend on terrain slope, soil burn severity class, and drainage basin area? Insights from airborne-LiDAR change detection, Earth Surf. Process. Landforms, 39, 1822–1832, https://doi.org/10.1002/esp.3570, 2014.

Pepin, N. C., Arnone, E., Gobiet, A., Haslinger, K., Kotlarski, S., Notarnicola, C., Palazzi, E., Seibert, P., Serafin, S., Schöner, W., Terzago, S., Thornton, J. M., Vuille, M., and Adler, C.: Climate Changes and Their Elevational Patterns in the Mountains of the World, Reviews of Geophysics, 60, e2020RG000730, https://doi.org/10.1029/2020RG000730, 2022.

Piermattei, L., Heckmann, T., Betz-Nutz, S., Altmann, M., Rom, J., Fleischer, F., Stark, M., Haas, F., Ressl, C., Wimmer, M., Pfeifer, N., and Becht, M.: Evolution of an Alpine proglacial river during seven decades of deglaciation quantified from photogrammetric and LiDAR digital elevation models, Earth Surf. Dynam. Discuss. [preprint], https://doi.org/10.5194/esurf-2022-63, 2022.

Pulighe, G. and Fava, F.: DEM extraction from archive aerial photos: accuracy assessment in areas of complex topography, European Journal of Remote Sensing, 46, 363–378, https://doi.org/10.5721/EuJRS20134621, 2013.

Rieger, D.: Bewertung der naturräumlichen Rahmenbedingungen für die Entstehung von Hangmuren: Möglichkeiten zur Modellierung des Murpotentials, vol. 51 of Münchener Geographische Abhandlungen A, Geobuch, München, 1999.

Rolstad, C., Haug, T., and Denby, B.: Spatially integrated geodetic glacier mass balance and its uncertainty based on geostatistical analysis: application to the western Svartisen ice cap, Norway, J. Glaciol., 55, 666–680, https://doi.org/10.3189/002214309789470950, 2009.

Sass, O., Haas, F., Schimmer, C., Heel, M., Bremer, M., Stöger, F., and Wetzel, K.: Impact of forest fires on geomorphic processes in the tyrolean limestone alps, Geografiska Annaler: Series A, Physical Geography, 94, 117–133, https://doi.org/10.1111/j.1468-0459.2012.00452.x, 2012.

Schiefer, E. and Gilbert, R.: Reconstructing morphometric change in a proglacial landscape using historical aerial photography and automated DEM generation, Geomorphology, 88, 167–178, https://doi.org/10.1016/j.geomorph.2006.11.003, 2007.

Serquet, G., Marty, C., Dulex, J.-P., and Rebetez, M.: Seasonal trends and temperature dependence of the snowfall/precipitationday ratio in Switzerland, Geophys. Res. Lett., 38, 14–18, https://doi.org/10.1029/2011GL046976, 2011.

Sevara, C., Verhoeven, G., Doneus, M., and Draganits, E.: Surfaces from the Visual Past: Recovering High-Resolution Terrain Data from Historic Aerial Imagery for Multitemporal Landscape Analysis, J Archaeol Method Theory, 25, 611–642, https://doi.org/10.1007/s10816-017-9348-9, available at: https://link.springer.com/article/10.1007/s10816-017-9348-9, 2018.

Skamarock, W. C. and Klemp, J. B.: A time-split nonhydrostatic atmospheric model for weather research and forecasting applications, Journal of Computational Physics, 227, 3465–3485, https://doi.org/10.1016/j.jcp.2007.01.037, 2008.

Slivinski, L. C., Compo, G. P., Whitaker, J. S., Sardeshmukh, P. D., Giese, B. S., McColl, C., Allan, R., Yin, X., Vose, R., Titchner, H., Kennedy, J., Spencer, L. J., Ashcroft, L., Brönnimann, S., Brunet, M., Camuffo, D., Cornes, R., Cram, T. A., Crouthamel, R., Domínguez-Castro, F., Freeman, J. E., Gergis, J., Hawkins, E., Jones, P. D., Jourdain, S., Kaplan, A., Kubota, H., Le Blancq, F., Lee, T.-C., Lorrey, A., Luterbacher, J., Maugeri, M., Mock, C. J., Moore, G. K., Przybylak, R., Pudmenzky, C., Reason, C., Slonosky, V. C., Smith, C. A., Tinz, B., Trewin, B., Valente, M. A., Wang, X. L., Wilkinson, C., Wood, K., and Wyszyński, P.: Towards a more reliable historical reanalysis: Improvements for version 3 of the Twentieth Century Reanalysis system, Quarterly Journal of the Royal Meteorological Society, 145, 2876–2908, https://doi.org/10.1002/qj.3598, 2019.

Smith, M. W., Carrivick, J. L., and Quincey, D. J.: Structure from motion photogrammetry in physical geography, Progress in Physical Geography: Earth and Environment, 40, 247–275, https://doi.org/10.1177/0309133315615805, 2016.

Staindl, A.: Kurze Geologie von Südtirol, Weger, Brixen, 2000.

Stark, M., Rom, J., Haas, F., Piermattei, L., Fleischer, F., Altmann, M., and Becht, M.: Long-term assessment of terrain changes and calculation of erosion rates in an alpine catchment based on SfM-MVS processing of historical aerial images. How camera information and processing strategy affect quantitative analysis, jgeomorphology, https://doi.org/10.1127/jgeomorphology/2022/0755, 2022.

Tarolli, P.: High-resolution topography for understanding Earth surface processes: Opportunities and challenges, Geomorphology, 216, 295–312, https://doi.org/10.1016/j.geomorph.2014.03.008, 2014.

Tollmann, A.: Geologie von Österreich: Die Zentralalpen, Deuticke, Wien, 1977.

Vehling, L.: Gravitative Massenbewegungen an alpinen Felshängen: Quantitative Bedeutung in der Sedimentkaskade proglazialer Geosysteme (Kaunertal, Tirol), Doctoral thesis, Friedrich-Alexander-Universität Erlangen-Nürnberg, Erlangen, 2016.

Veit, H.: Die Alpen: Geoökologie und Landschaftsentwicklung, Ulmer, Stuttgart, 2002.

Wester, T., Wasklewicz, T., and Staley, D.: Functional and structural connectivity within a recently burned drainage basin, Geomorphology, 206, 362–373, https://doi.org/10.1016/j.geomorph.2013.10.011, available at: http://www.sciencedirect.com/science/article/pii/S0169555X13005242, 2014.

Zhong, Y., Liu, Q., Westoby, M., Nie, Y., Pellicciotti, F., Zhang, B., Cai, J., Liu, G., Liao, H., and Lu, X.: Intensified paraglacial slope failures due to accelerating downwasting of a temperate glacier in Mt. Gongga, southeastern Tibetan Plateau, Earth Surf. Dynam., 10, 23–42, https://doi.org/10.5194/esurf-10-23-2022, 2022.